

ANNEALING-DEPENDENT PHENOMENA IN $\text{Ga}_{1-x}\text{Mn}_x\text{As}$

A Dissertation Presented to
The Faculty of the Graduate School
University of Missouri - Columbia

In Partial Fulfillment
of the Requirements for the Degree
Doctor of Philosophy

by

BRIAN KIRBY

Dr. Jim Rhyne, Dissertation Supervisor

DECEMBER 2004

This work has been supported by NSF Grant No. DMR 013819.

The Undersigned, appointed by the Dean of the Graduate Faculty,
have examined a dissertation entitled

ANNEALING-DEPENDENT PHENOMENA IN $\text{Ga}_{1-x}\text{Mn}_x\text{As}$

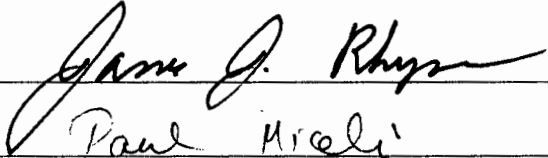
presented by

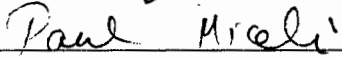
BRIAN KIRBY


a candidate for the degree

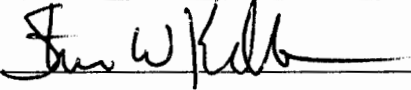
DOCTOR OF PHILOSOPHY

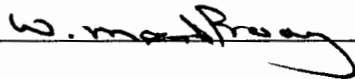
and hereby certify that in their opinion it is worthy of acceptance











October 15, 2004

For E

Acknowledgements

There are lots of people to thank. The first is Jim Rhyne, for taking me on as a student, and for treating me so exceptionally well. I've never met another grad student whose advisor provided the type of opportunities that mine has for me. I greatly appreciate Jim's technical training, but I also appreciate his efforts to help me make professional connections, and become integrated into the neutron scattering community. Among these connections has been Julie Borchers, who trained me in neutron reflectometry, and was truly integral to the experiments in this dissertation. Julie has vastly exceeded the requirements of her job in the way she has mentored me, and I am sincerely thankful for it. I've also greatly enjoyed getting to know Kevin O'Donovan and Suzanne te Velthuis, who have been valuable teachers and collaborators. I also thank Chuck Majkrzak, as the NG-1 Reflectometer is essentially his instrument, and these difficult experiments would not have been possible without the vast amounts of beamtime his support provided us. And of course, thanks go to Jacek Furdyna, and all of the Notre Dame guys, especially Tomek Wojtowicz and Xinyu Liu, who spent so much time and effort fabricating the world-class samples for this project.

From a personal standpoint, the first person to thank is my wife, Elizabeth. E is my perfect complement, and is the best friend I could ever hope for. I'd like to thank my parents Pat and Jim, who have given me nothing but support as I've pursued a career in science. I credit The Old Man for initiating my interest in physics (see Fig. 0.1). I also

thank my brothers, Kevin and Al, who I view as models for professional success.

Additionally, very special thanks go to D. DeBonis and T. Cougar, for their tireless efforts in service of the community. In closing, I thank my Creator.

BRIAN JAMES KIRBY

University of Missouri-Columbia

October, 2004

How to achieve Chain reaction

U-235 = 92 Protons - 143 Neutrons $\begin{array}{r} 92 \\ 143 \\ \hline 235 \end{array}$

U-238 = 92 Protons - 146 Neutrons $\begin{array}{r} 92 \\ 146 \\ \hline 238 \end{array}$

Less than one atom in 100 of U is 235
 U-238 can absorb neutrons without splitting
 (as a whole no chain reaction)
 For chain reaction enrich a pile of U by
 putting in more U-235

Another way of achieving chain reaction with
 natural U is by slowing down neutrons with
 substance called a moderator (water & carbon
 are good moderators)
 To make a chain reaction it is necessary to
 build a structure with pieces of U
 interlaced with pieces of moderators
 (Fission atoms easy to split)

Neutron one of the basic parts of all matter
 make up 99.9% of atom mass
 (discovered 1932)

Proton - a stable Pos charged sub
 atomic particle having a mass 1836
 times of electron

Jim Kirby 1987

Figure 0.1: Notes on nuclear fission made by Jim Kirby, C.F.I. My dad is a farmer, and while out on the tractor one day, it occurred to him that he had no idea how nuclear reactions worked. So, he read up on it. He enjoyed the subject tremendously – so much that Enrico Fermi became one of his personal heroes. I was nine years old at the time, and he let me help with his studies, sparking an interest in physics. Years later, I would find myself performing experiments at nuclear reactors like the ones we read about.

Contents

Acknowledgements	ii
List of Figures	vii
List of Tables	x
Abstract	xi

Chapter 1: Introduction to $\text{Ga}_{1-x}\text{Mn}_x\text{As}$

1.1 Introductory Remarks	1
1.2 Spintronics	1
1.3 Dilute Magnetic Semiconductors	4
1.4 The “Hole” Shooting Match	5
1.5 Post-Growth Annealing	6
1.6 Limits on Useful Mn Concentration	7
1.7 The Villain: Interstitial Mn	9
1.8 What Becomes of the Villain?	14
1.9 Brief Summary of What We Know	15
1.10 Goals of This Study	16
1.11 Polarized Neutron Reflectometry Measurements	17
1.12 Inelastic Neutron Scattering Measurements	19

Chapter 2: Polarized Neutron Reflectometry

2.1	Introduction	20
2.2	Reflection of Neutrons	21
2.3	Reflection of Polarized Neutrons	26
2.4	PNR Measurements	32
2.5	NG-1 Reflectometer	33
2.6	POSY-I Reflectometer	38
2.7	Data Corrections	39
2.8	Data Analysis	40

Chapter 3: Annealing Dependence of the $\text{Ga}_{1-x}\text{Mn}_x\text{As}$ Depth Profile

3.1	Introduction	47
3.2	Sample Preparation	48
3.3	Sample Weirdness	49
3.4	Measurement Difficulties	53
3.5	Set A: Annealing Dependence in a 50 nm Film	54
3.6	χ by Eye	65
3.7	Spin-Flip Data	69
3.8	Lower-Field Scans of Set A	72
3.9	Set B: Annealing Dependence in a 100 nm Film	77
3.10	Set C: Annealing Dependence, <i>Minimally</i> Changing Depth Profile	88
3.11	Early Work	99
3.12	Conclusions	100

Chapter 4: Effects of a Capping Layer on the $\text{Ga}_{1-x}\text{Mn}_x\text{As}$ Depth Profile

4.1 Introduction	101
4.2 Capping Recap	102
4.3 Sample Preparation and Net Characterization	103
4.4 PNR Measurements	104
4.5 Interpretation of PNR Data	112
4.6 Conclusion	117

Chapter 5: Search for Magnons in $\text{Ga}_{1-x}\text{Mn}_x\text{As}$

5.1 Introduction	118
5.2 Theoretical Magnon Dispersion	118
5.3 Inelastic Neutron Scattering	121
5.4 World Record Samples	122
5.5 SPINS Measurements	123

Appendix A: Reflpol Models	128
-----------------------------------	-----

Bibliography	138
---------------------	-----

Publications	144
---------------------	-----

Invited Talks	145
----------------------	-----

Contributed Conference Presentations	146
---	-----

Vita	147
-------------	-----

List of Figures

0.1	Notes on nuclear fission	iii
1.1	Cartoon of a spin FET	3
1.2	x -dependence of magnetization and magnetic moment in $\text{Ga}_{1-x}\text{Mn}_x\text{As}$	8
1.3	Crystal structure of $\text{Ga}_{1-x}\text{Mn}_x\text{As}$	10
2.1	Diagram illustrating specular reflection	24
2.2	Diagram of in-plane magnetization	29
2.3	Schematic of the NG-1 Reflectometer	34
2.4	Photograph of the upstream end of the NG-1 Reflectometer	36
2.5	Photograph of the sample housing on NG-1	37
2.6	Example data illustrating the effects of Q -dependent sample illumination	41
2.7	Explanation of features found in PNR data	43
3.1	Example θ rocking curve showing the “shoulders” common to our samples	50
3.2	Example data illustrating the anomalous background common to our samples	52
3.3	Reflectivities comparing the set A as-grown and annealed samples	56
3.4	Comparison of the reflectivities for the set A samples	58
3.5	Spin asymmetries for the set A samples	60
3.6	SLD models used to fit the set A samples	62
3.7	Comparison of models for the set A as-grown sample	67

3.8	Comparison of models for the set A annealed sample	68
3.9	Example data showing the spin-flip scattering common to our samples	70
3.10	SLD model used to fit the non spin-flip, and spin-flip data from Fig. 3.9	71
3.11	Reflectivities comparing the lower-field scans for set A	74
3.12	Spin asymmetry for the lower-field set A scans	75
3.13	SLD models used to fit the lower-field data for set A	76
3.14	SQUID magnetometry measurements of the set B samples	78
3.15	Reflectivities comparing the set B as-grown and annealed samples	80
3.16	Comparison of the reflectivities for the set B samples	81
3.17	Spin asymmetries for the set B samples	83
3.18	SLD models used to fit the set B data	84
3.19	Comparison of models for the set B as-grown data	85
3.20	Comparison of models for the set B annealed data	87
3.21	Reflectivities comparing the set C as-grown and annealed samples	92
3.22	Comparison of the reflectivities for the set C samples	93
3.23	Spin asymmetries for the set C samples	94
3.24	SLD models used to fit the Set C data	95
4.1	SQUID magnetometry measurements for the capped samples	105
4.2	18 K reflectivities comparing the capped as-grown and annealed samples	107
4.3	18 K comparison of the reflectivities for the capped samples	108
4.4	18 K spin asymmetries for the capped samples	110
4.5	SLD models used to fit the 18 K data for the capped samples	111
4.6	13 K comparison of the reflectivities for the capped samples	113

4.7	13 K spin asymmetries for the capped samples	114
4.8	SLD models used to fit the 13 K data for the capped samples	115
5.1	Inelastic neutron scattering scans of the thick samples	125
5.2	Measured and calculated magnon dispersion	127

List of Tables

3.1 Summary of bulk properties for the Chapter 3 samples	90
A.1 Reflpol parameters, sample A, as-grown, high-field scan	129
A.2 Reflpol parameters, sample A, annealed, high-field scan	129
A.3 Reflpol parameters, sample A, as-grown, high-field, alternate model	130
A.4 Reflpol parameters, sample A, annealed, high-field, alternate model	130
A.5 Reflpol parameters, sample A, annealed, high-field, spin-flip model	131
A.6 Reflpol parameters, sample A, as-grown, low-field scan	131
A.7 Reflpol parameters, sample A, annealed, low-field scan	132
A.8 Reflpol parameters, sample B, as-grown	132
A.9 Reflpol parameters, sample B, annealed	133
A.10 Reflepol parameters, sample B, as-grown, alternate model	133
A.11 Reflpol parameters, sample B, annealed, alternate model	134
A.12 Reflpol parameters, sample C, as-grown	134
A.13 Reflpol parameters, sample C, annealed	135
A.14 Reflpol parameters, capped, as-grown, 18 K	135
A.15 Reflpol parameters, capped, annealed, 18 K	136
A.16 Reflpol parameters, capped, as-grown, 13 K	136
A.17 Reflpol parameters, capped, annealed, 13 K	137

Abstract

There has been a great deal of recent research interest in the development of electronic-type devices that exploit not only an electron's charge, but also its spin. Such "spintronic" devices hold the promise of higher stability data storage, increased processing speed, and decreased power consumption as compared with conventional electronics. Many potential spintronic devices will require a "spin injector" capable of producing a current in which almost all the electrons have their spins aligned in the same direction. In particular, it would be valuable to develop a *ferromagnetic semiconductor* spin injector that could spin-polarize electrons with its magnetic field, and is compatible with semiconductor materials common to existing electronic devices. A promising candidate for such a spin-injector is $\text{Ga}_{1-x}\text{Mn}_x\text{As}$, due to its relatively high ferromagnetic transition temperature (T_C as high as 150 K), and its crystallographic compatibility with standard GaAs. However, in order to achieve maximum T_C , $\text{Ga}_{1-x}\text{Mn}_x\text{As}$ must be carefully annealed after growth. While it has been known since 2001 that annealing can increase T_C , it has not been understood until very recently exactly how annealing achieves this benefit.

With the aim of better understanding the mechanisms of this annealing process, this dissertation's primary focus is polarized neutron reflectometry (PNR) experiments that examine how annealing changes the depth-dependent magnetic and chemical properties of $\text{Ga}_{1-x}\text{Mn}_x\text{As}$ thin films. In several cases, these measurements show

annealing to increase the magnetization, make the depth dependence of the magnetization more uniform, and alter the chemical composition of the film's free surface. These results provide compelling evidence that annealing enhances $\text{Ga}_{1-x}\text{Mn}_x\text{As}$ by ripping ferromagnetically disruptive Mn impurities from the crystal lattice, freeing them to migrate to the surface of the film - corroborating other recent work.

A $\text{Ga}_{1-x}\text{Mn}_x\text{As}$ film capped with a layer of GaAs was also examined. We find that annealing of the capped film *does not* enhance the ferromagnetic properties, suggesting that the cap prevents interstitial Mn impurities from reaching the surface. Additionally, we find that the as-grown capped film features a significant magnetization gradient - a feature that remains the same after annealing. This suggests that the GaAs capping layer ruins the annealing process not simply by serving as a barrier to interstitial Mn impurities, but that it does so by changing the environment of the *entire* $\text{Ga}_{1-x}\text{Mn}_x\text{As}$ film.

Chapter 1

Introduction to $\text{Ga}_{1-x}\text{Mn}_x\text{As}$

1.1 Introductory Remarks

The principal topic of this dissertation is a study of the magnetic and chemical depth profiles of $\text{Ga}_{1-x}\text{Mn}_x\text{As}$. In addition, an attempt to establish the spin wave dispersion in $\text{Ga}_{1-x}\text{Mn}_x\text{As}$ will also be discussed. This initial chapter is devoted to introducing the scientific interest in this technologically important material, and to outlining some of the important issues concerning $\text{Ga}_{1-x}\text{Mn}_x\text{As}$ that the remainder of the paper addresses.

1.2 Spintronics

There is a great deal of current research interest in the development of “spintronics” technology. This term refers to electronic devices that exploit the spin degree of freedom of charged particles. Some possible benefits of spintronic devices could include data storage with reduced volatility, increased data processing speed, and

decreased electrical power consumption as compared with conventional semiconductor devices [1]. Ferromagnetic semiconductors could play an important role in the development of practical spintronic technology – particularly if such materials could be fabricated with high ferromagnetic transition temperatures (T_C).

As an example of the device utility of such a material, consider the example of the spin field-effect transistor (spin FET) [2]. A standard FET is a common electronic device that consists of a source and a drain, connected by a semiconducting channel. Charge carriers flowing from the source can be pushed out of the semiconducting channel with an applied electric field, allowing for control of the current flowing through the drain. A spin FET would have the same basic elements as a conventional FET, but it would be different in that the source and drain would be ferromagnetic. The ferromagnetic source would allow for polarized electrons (or holes) to be injected into the semiconducting channel. If the ferromagnetic drain were to have its magnetization polarized parallel to the carriers, the polarized current would flow freely. However, if carrier spins were rotated perpendicular to the drain via an applied voltage, the current would be impeded. In principle, this mechanism of rotating spins would require less energy, and could result in faster switching than in a conventional FET. Figure 1.1 [3] illustrates a spin FET.

A major challenge in developing a practical spin FET (or many other spintronic devices) involves finding suitable materials for spin injection (for instance, the source in a spin FET). One approach to this problem has been to use ferromagnetic metals to inject spin into semiconductors [4]. However, there are numerous troubles associated with spin injection across a metal-semiconductor interface, resulting in difficulties in achieving a useful degree of spin polarization. Alternatively, it has been demonstrated

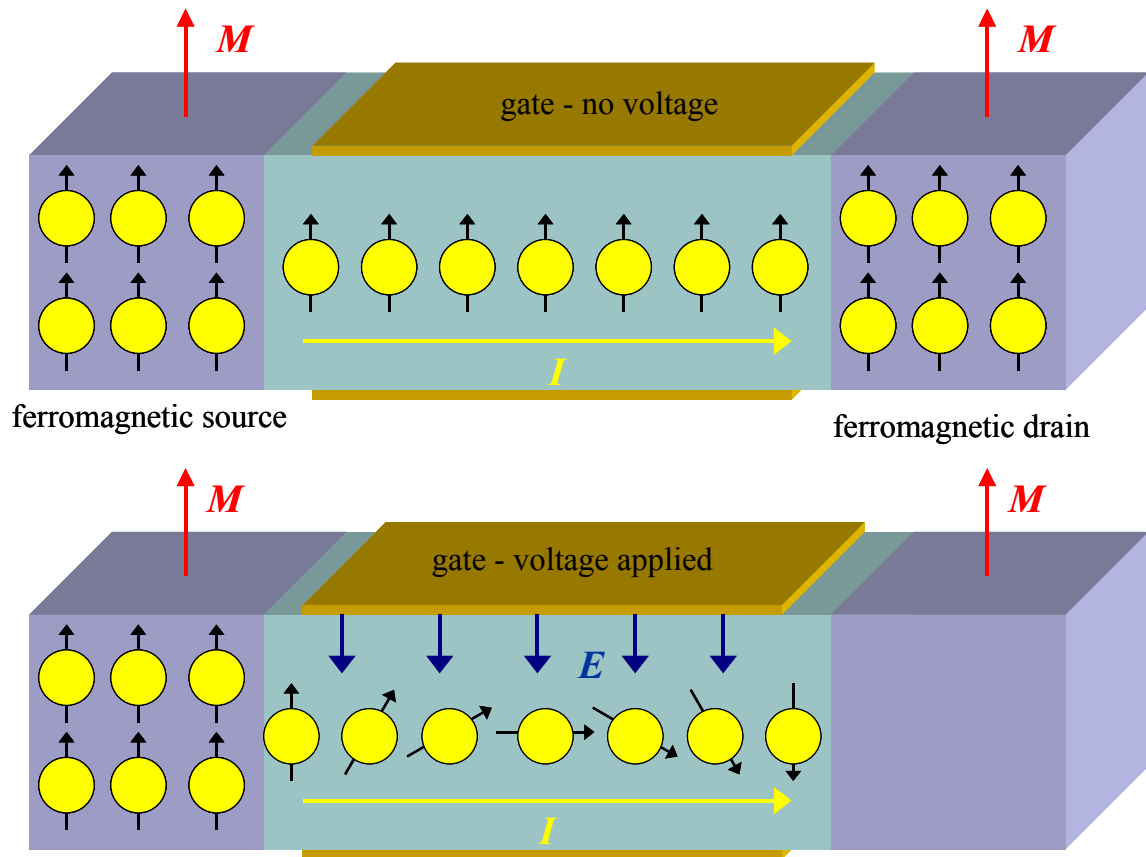


Figure 1.1: Cartoon of a spin FET. When no voltage is applied across the semiconducting channel (top), charge carriers spin polarized by the ferromagnetic source freely pass through the ferromagnetic drain. However, when a voltage is applied (bottom), the spin polarized carriers precess throughout the channel. This is done such that their spins are anti-parallel to the magnetization of the drain at the interface, inhibiting passage.

that ferromagnetic semiconductors can serve as effective spin injectors [5, 6]. This approach provides the advantage of spin injectors already compatible with semiconductor materials common in modern electronics, such as GaAs. This pursuit of all semiconductor spintronic devices provides technological motivation for study of the magnetic properties of ferromagnetic semiconductors.

1.3 Dilute Magnetic Semiconductors

Magnetic semiconductors have been studied since the 1960's, with early studies focusing on natural ferromagnetic semiconductors such as europium chalcogenides [7], and semiconducting spinels [8]. However, these materials are not particularly useful for spintronic applications because they generally exhibit a low T_C [1], and are crystallographically incompatible with standard semiconducting materials [9].

In addition, artificial magnetic semiconductors can be fabricated by randomly doping common semiconductors with magnetic impurities. This results in a class of materials known as *dilute magnetic semiconductors* (DMS). Initially, study of DMS focused on materials where the valency of the magnetic impurities corresponded with that of the semiconducting host, such as alloys of Mn with type II-VI semiconductors [10]. While this valency matching makes these II-VI DMS relatively easy to fabricate, the magnetic exchange in these materials is typically antiferromagnetic, often leading to spin-frustrated, spin-glass behavior [9] because of the tetrahedral site symmetry of the magnetic ion.

A major revolution in DMS research has occurred in the last fifteen years, as advancements in crystal growth have given researchers the opportunity to dope Mn into

other types of semiconductor materials where the exchange can be *ferromagnetic*. In particular, developments in non-equilibrium molecular-beam epitaxy (MBE) growth techniques have allowed crystal growers to “force” magnetic atoms into lattice sites of standard III-V semiconductors, while leaving the crystal structure largely intact. The first example of a III-V DMS came in 1989, when $\text{In}_{1-x}\text{Mn}_x\text{As}$ was developed [11], and was then later found to exhibit partial ferromagnetic order [12]. However, the III-V DMS that has received the most research attention is $\text{Ga}_{1-x}\text{Mn}_x\text{As}$. First fabricated in 1996, $\text{Ga}_{1-x}\text{Mn}_x\text{As}$ has been shown to display true long-range ferromagnetic order [13], and has been widely used as a “prototypical” material for study of III-V DMS.

1.4 The “Hole” Shooting Match

The primary reason that $\text{Ga}_{1-x}\text{Mn}_x\text{As}$ has received such wide attention is its relatively high T_C . Since the initial report of $T_C \approx 60$ K given in reference 13, the maximum reported value of T_C in $\text{Ga}_{1-x}\text{Mn}_x\text{As}$ has progressively increased in recent years, exceeding 150 K [14, 15]. While this value has generated a great deal of interest and optimism, it is still well below room temperature. The question that will determine the real technological usefulness of $\text{Ga}_{1-x}\text{Mn}_x\text{As}$ is whether or not T_C can continue to be pushed towards room temperature, or if there is a fundamental lower-temperature limit. In order to address this question, one must consider the charge doping of the system, as T_C for $\text{Ga}_{1-x}\text{Mn}_x\text{As}$ is strongly tied to carrier concentration.

The ferromagnetic behavior in $\text{Ga}_{1-x}\text{Mn}_x\text{As}$ originates from coupling between spin $5/2 \text{ Mn}^{2+}$ ions that occupy Ga sites in the lattice (Mn_{Ga}) [16]. The coupling is thought to be similar to the RKKY interaction in metals [17] where the ferromagnetic exchange is

mediated by charge carriers. For $\text{Ga}_{1-x}\text{Mn}_x\text{As}$ it is widely accepted that Mn_{Ga} are acceptors, and that they communicate their spin orientation among each other via self-generated holes [18]. So, the hole concentration is “the hole shooting match”, so to speak, when it comes to understanding the ordering temperature of $\text{Ga}_{1-x}\text{Mn}_x\text{As}$. Specifically, Dietl *et al* have proposed that T_C can be described by the Zener model of ferromagnetism [19, 20], which predicts that

$$T_C = C x p^{1/3} \quad (1)$$

where C is a constant, x is the concentration of Mn_{Ga} , and p is the hole concentration.

1.5 Post-Growth Annealing

An important discovery was made in 2000, when it was found (by accident, the story goes) that post-growth annealing of $\text{Ga}_{1-x}\text{Mn}_x\text{As}$ at temperatures near or below the growth temperature greatly enhances T_C [21]. It was later shown that annealing could also increase the saturation magnetization [22]. Further work revealed that the T_C enhancement effect is strongly dependent on the annealing temperature, and on the annealing time [22, 23]. Interestingly, it was found that the success of the annealing process is extremely sensitive to the annealing conditions. The predominant technique (described in Ref. 22) involves annealing at or slightly above the growth temperature ($\sim 250 - 280$ °C) for short periods of time ($\sim 1-2$ hours). Alternatively, it has been shown [23] that annealing at much lower temperatures ($\sim 175 - 200$ °C) for much longer periods of time (~ 100 hours), can produce a similar increase in T_C . If samples are “over-

annealed” (e.g. for too high a combination of temperature and time), annealing has a *detrimental* effect on the ferromagnetic properties of $\text{Ga}_{1-x}\text{Mn}_x\text{As}$.

1.6 Limits on Useful Mn Concentration

In 2002, Potashnik *et al.* conducted a detailed study of the effects of annealing on $\text{Ga}_{1-x}\text{Mn}_x\text{As}$ [24]. By using SQUID magnetometry and transport measurements to examine films of varying x , they showed that instead of continuously improving with increasing x , the ferromagnetic properties of $\text{Ga}_{1-x}\text{Mn}_x\text{As}$ are enhanced only up to a point. For optimally annealed samples, it was found that below $x \approx 0.05$, the conductivity (i.e. the hole concentration), T_C , and the zero temperature magnetization increased with increasing x . However, above $x \approx 0.05$, it was observed that all of these properties leveled off. Figure 1.2 shows the zero-temperature magnetization and the corresponding magnetic moment per Mn_{Ga} as a function of x (from Ref. 24), which is particularly telling. Divalent spin $5/2$ Mn (expected for Mn_{Ga}) should each contribute a magnetic moment of $4 - 5 \mu_B$. However, Figure 1.2 shows that only at $x \approx 0.01$ did the magnetic moment per Mn_{Ga} approach that expected value. As x increased above 1 %, the moment per Mn_{Ga} progressively decreased. This result implied that a progressively smaller fraction of the Mn_{Ga} were actually participating in the ferromagnetic exchange.

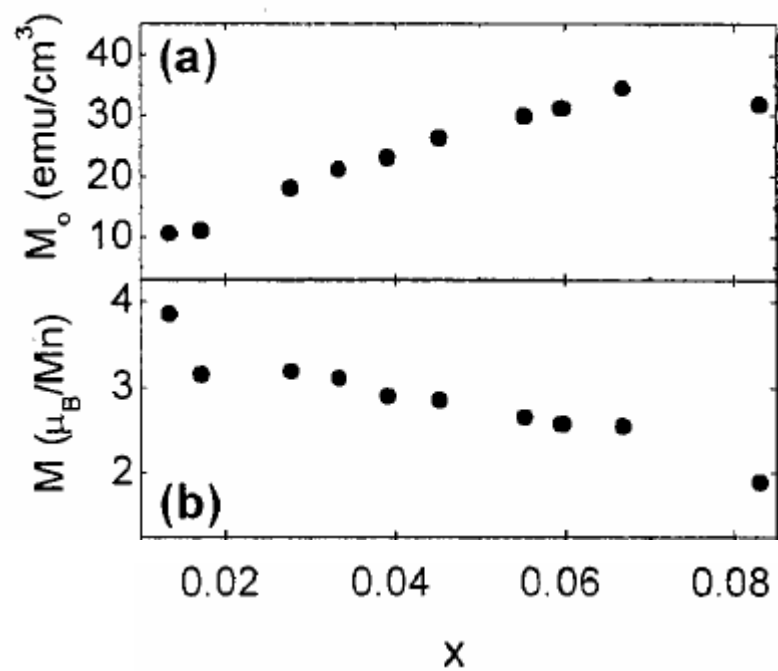


Figure 1.2: Optimally annealed $\text{Ga}_{1-x}\text{Mn}_x\text{As}$ zero-temperature magnetization (a) and magnetic moment per Mn_{Ga} ion (b) as a function of Mn_{Ga} concentration. Figure taken from Ref. 24.

The results described above begged some important questions:

- Why does annealing increase T_C and the magnetization?
- Why does annealing only work well for a very specific time and temperature?
- Why do T_C , the hole concentration, and the magnetization not progressively increase as more Mn is added to the system?
- Can T_C continue to increase, or is there a fundamental limit?

Some answers to these questions have started to come to light in the past two years. The current conventional wisdom is that the key to understanding these phenomena lies in understanding an *unwanted* Mn impurity.

1.7 The Villain: Interstitial Mn

The crystal lattice of GaAs has the zinc-blende structure, in which there are two interstitial sites with tetrahedral coordination. When Mn atoms occupy these interstitial sites, they act as double donors (all metal atom interstitials are donors). Therefore, in $\text{Ga}_{1-x}\text{Mn}_x\text{As}$, Mn interstitials (Mn_i) add electrons to the system which neutralize holes that are needed to mediate the ferromagnetic exchange. Figure 1.3 [25] shows the location of the different atoms in $\text{Ga}_{1-x}\text{Mn}_x\text{As}$.

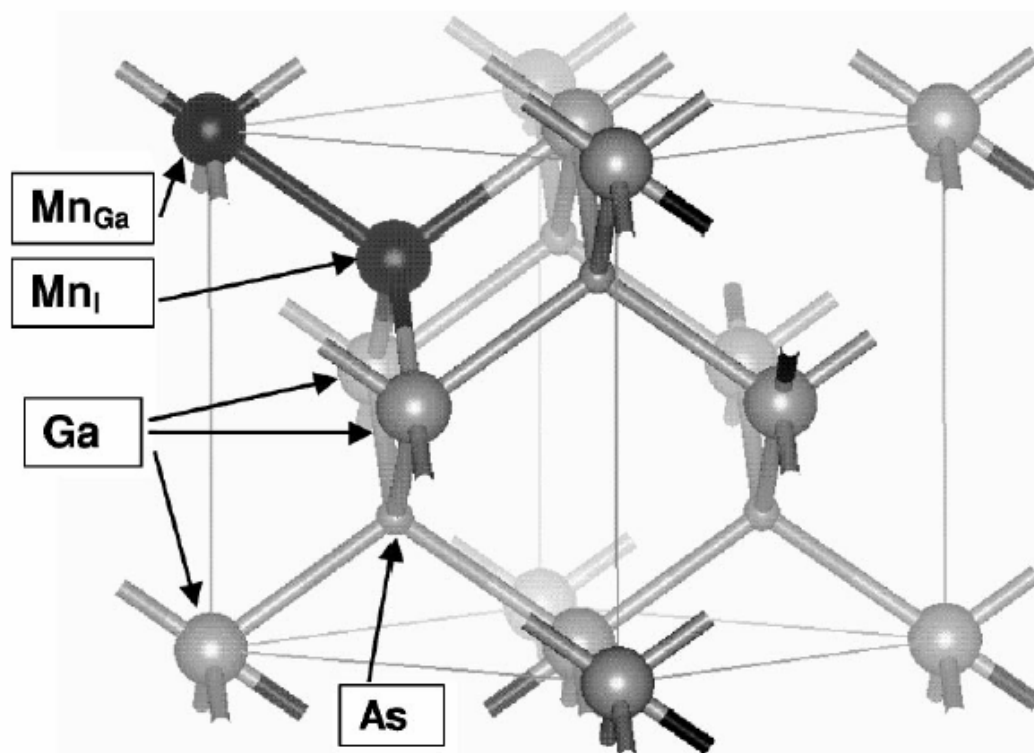


Figure 1.2: Crystal structure of Ga_{1-x}Mn_xAs. Figure taken from Ref. 25.

In addition to eliminating holes, it is likely that Mn_I hinders the ferromagnetic exchange in a second way. Calculations suggest that when in close proximity, Mn_I and Mn_{Ga} exhibit an *antiferromagnetic* exchange interaction [25]. Mn_I is known to be a highly mobile defect, and as a positively charged double donor it has an electrostatic attraction to the negatively charged acceptor Mn_{Ga} . For these reasons, it is reasonable to think that a significant number of Mn_I and Mn_{Ga} are in close proximity following growth of $Ga_{1-x}Mn_xAs$. So, it is likely that many Mn_I present in $Ga_{1-x}Mn_xAs$ are antiferromagnetically bonded with nearby Mn_{Ga} , canceling their moments, and *directly* reducing the overall magnetization.

The role of these interstitials was investigated by Yu *et al.* in 2002 using Rutherford backscattering and particle-induced x-ray emission [26]. For their experiments, three pieces of a 110 nm $Ga_{1-x}Mn_xAs$ film were cut from a single wafer. One piece was left as-grown, a second piece was optimally annealed (1 hour at 282 °C), and a third piece was “over-annealed” (1 hour at 350 °C). T_C for the as-grown film was 67 K. For the optimally annealed film T_C increased to 111 K, but for the over-annealed film T_C dropped to 49K. The channeling measurements showed that for the as-grown film, a significant amount of Mn occupied interstitial sites. When the optimally annealed film was examined, it was found to have a reduced concentration of Mn_I , and a higher concentration of Mn at random locations as compared to the as-grown film. Results for the over-annealed sample implied a very high concentration of Mn at random positions and a reduction in Mn at both interstitial and substitutional positions.

These results were very important, as they suggested that the annealing process enhanced the ferromagnetic properties of $\text{Ga}_{1-x}\text{Mn}_x\text{As}$ by liberating Mn_I and redistributing them to random sites, where the Mn would be electrically inactive, and unable to hinder the ferromagnetic exchange by either neutralizing holes or canceling Mn_{Ga} moments. Additionally, these results help explain the detrimental effects of over-annealing, by corroborating the idea that Mn_{Ga} are held more strongly to the lattice than are the very mobile Mn_I . Comparison of the three samples suggests that when $\text{Ga}_{1-x}\text{Mn}_x\text{As}$ is annealed at the optimal temperature, Mn_I are redistributed to random sites, allowing a previously suppressed population of Mn_{Ga} to participate in the ferromagnetic exchange. Alternatively, when the annealing temperature is raised, there is enough energy to liberate the more tightly bound Mn_{Ga} , reducing the number of Mn that participate in ferromagnetism. So, with this work, a plausible explanation of the annealing process was produced – optimal annealing puts Mn_I in places where it can't do any damage, without disturbing a significant amount of Mn_{Ga} .

The authors of Ref. 26 also proposed a solution to the mystery of why the ferromagnetic properties of $\text{Ga}_{1-x}\text{Mn}_x\text{As}$ do not continually improve with increasing x . Their argument revolves around the fact that the concentration of charged defects is largely determined by the Fermi energy [27]. In their picture, as Mn progressively enter Ga sites during the growth process, each new Mn_{Ga} adds to the concentration of electrically active acceptors, while at the same time adds to the number of uncompensated spins. That leads to an increasing downward shift of the Fermi energy, which progressively increases the formation energy for negatively charged defects such as Mn_{Ga} . As more and more Mn are added to the system, it becomes progressively more

difficult for a Mn atom to find its way to a Ga site. Therefore, a progressively larger fraction of Mn atoms end up in locations where they do not raise the hole concentration – such as interstitial sites. This reasoning suggests that as x increases to a value where T_C no longer increases, Mn are also entering interstitial sites in sufficient numbers as such to maintain a constant hole concentration.

Some credence to this idea was given by a study conducted by Lee *et al.* in 2003 [28]. In this work, a pair of $\text{Ga}_{1-x}\text{Mn}_x\text{As}$ films of differing x were doped with varying concentrations of Be (an acceptor), in an attempt increase the hole concentration (and thereby T_C). After examining the films using SQUID magnetometry and magnetotransport measurements, it was found that for $x = 0.03$, T_C did progressively increase with increasing Be concentration. This implies that for this value of x , Be doping was successfully increasing the hole concentration. However, when the Mn_{Ga} concentration was raised to $x = 0.05$, further increases in Be concentration systematically *decreased* T_C . This gives indirect evidence to suggest that above a maximum hole concentration, a progressively larger fraction of added Mn does go to interstitial sites. If this is the case, a fundamental limit on the hole concentration could be a roadblock to significant further increases in T_C .

Another impurity that is a source of trouble in $\text{Ga}_{1-x}\text{Mn}_x\text{As}$ is As antisites, that is, As that ends up at Ga sites (As_{Ga}) [29, 30]. Like Mn_{I} , As_{Ga} is a double donor, and is therefore detrimental to the ferromagnetic exchange. However, it is not likely that As_{Ga} are major players in annealing dependent phenomena. As_{Ga} has been shown to be a stable defect at temperatures up to 450 °C [31], while optimal annealing of $\text{Ga}_{1-x}\text{Mn}_x\text{As}$ takes place at temperatures below 300 °C.

1.8 What Becomes of The Villain?

If liberation of Mn_I is reason that annealing works, where does that liberated Mn end up? This question has been addressed in a number of recent studies that focus on surface and interface effects in $Ga_{1-x}Mn_xAs$ (including the research results of this dissertation). In 2003, Chiba *et al.* studied the effects of annealing $Ga_{1-x}Mn_xAs/GaAs/Ga_{1-x}Mn_xAs$ trilayer structures [32]. It was found that optimal annealing significantly improved T_C for the $Ga_{1-x}Mn_xAs$ layer with a free surface, whereas it had no apparent effect on the $Ga_{1-x}Mn_xAs$ layer that was covered with GaAs. This result implied that the presence of a free surface was critical to successful annealing of $Ga_{1-x}Mn_xAs$.

Experiments along a similar vein were undertaken by Stone *et al.* in 2003 [33]. This group examined the effects of annealing on a series of $Ga_{1-x}Mn_xAs$ films with varying thickness of GaAs capping layers. It was found that as little as ten monolayers of GaAs (~ 3 nm) were sufficient to completely suppress any positive effects of annealing. Additionally, electron micro-probe analysis (EMPA) measurements indicated a rise in Mn concentration for uncapped annealed films, as compared to capped annealed films. EMPA measurements are most sensitive to surface effects, due to the short penetration depth of the probing electrons. Therefore, these results suggested an increased Mn concentration at the surface of the film. In particular, this suggested that Mn_I were diffusing to the film surface during annealing.

Auger measurements published by Edmonds *et al.* in 2004 confirmed the presence of increased Mn at the surface of optimally annealed $Ga_{1-x}Mn_xAs$ films [15]. Also, this group performed time-dependent resistivity measurements on $Ga_{1-x}Mn_xAs$ films during

annealing. These measurements showed a systematic decrease of resistivity as a function of annealing time, implying a systematic increase in hole concentration. These annealing-dependent resistivity measurements determined a 0.7 ± 0.1 eV energy barrier for diffusion of Mn_I to the surface. This measured value compared favorably with *ab initio* calculations that considered the effect of $Mn_{Ga} - Mn_I$ complexes and electric fields produced by Mn_{Ga} .

Our polarized neutron reflectometry measurements published in 2004 [34] provided additional evidence for surface diffusion of Mn in $Ga_{1-x}Mn_xAs$ during annealing. This work will be described in great detail in later chapters.

1.9 Brief Summary of What We Know

To summarize, the following picture is now widely accepted for $Ga_{1-x}Mn_xAs$:

- Mn that exist at Ga sites (Mn_{Ga}) are the “good guys”. Mn_{Ga} participate in a ferromagnetic exchange mediated by holes they themselves create. Mn at interstitial sites (Mn_I) are the “villains”. Mn_I are double donors, and are thought to align antiferromagnetically with neighboring Mn_{Ga} .
- Optimal annealing increases T_C and the saturation magnetization in $Ga_{1-x}Mn_xAs$ by overcoming the binding energy of Mn_I , allowing it to diffuse to the surface to the sample.

- If a $\text{Ga}_{1-x}\text{Mn}_x\text{As}$ sample is over-annealed, enough energy is added to the system to release Mn_{Ga} from its spot in the lattice.
- There appears to be a maximum hole concentration at which $\text{Ga}_{1-x}\text{Mn}_x\text{As}$ can be grown. Above this hole concentration, further added Mn becomes progressively more likely to occupy interstitial sites.
- It is not yet known whether advances in sample growth or annealing techniques can overcome this apparent hole concentration limit, and further increase T_C by a significant amount

1.10 Goals of This Study

This dissertation work is a neutron scattering study of dilute $\text{Ga}_{1-x}\text{Mn}_x\text{As}$ thin films. At the time that this study was initiated (May, 2002), $\text{Ga}_{1-x}\text{Mn}_x\text{As}$ was already a hot research topic. However, at that time no neutron scattering studies of dilute $\text{Ga}_{1-x}\text{Mn}_x\text{As}$ films had been published (and our work was the first). In addition, the state of understanding concerning $\text{Ga}_{1-x}\text{Mn}_x\text{As}$ has evolved considerably since the start of this project. For instance, the ferromagnetically enhancing properties of annealing were already well established empirically. However, the surface was only beginning to be scratched with regard to the mechanisms with which annealing was achieving those benefits. Furthermore, questions surrounding the mysterious low magnetization per Mn atom were still at the forefront of discussion.

Given this situation, we hoped to gain insight into the ferromagnetic exchange and annealing-dependent properties of $\text{Ga}_{1-x}\text{Mn}_x\text{As}$ by using the unique microscopic probe provided by neutron scattering. The samples for this study have been fabricated by Prof. Jacek Furdyna's group at the University of Notre Dame. Tomek Wojtowicz and Xinyu Liu led the growth effort, and were assisted by Weng-Lee Lim, ShaoPing Shen, and Zhiguo Ze. Additionally, our Notre Dame collaborators have provided bulk characterization of their samples, using SQUID magnetometry, and magnetotransport measurements.

The majority of the neutron scattering measurements, which were initiated in May, 2002, were performed at the NIST Center for Neutron Research (NCNR) at the National Institute for Standards and Technology. These experiments were performed in collaboration with NCNR researchers Julie Borchers, Kevin O'Donovan, and Sungil Park. Additional measurements were taken at the Intense Pulsed Neutron Source (IPNS), and the Materials Science Division (MSD) at Argonne National Laboratory in collaboration with MSD researchers Suzanne te Velthuis and Axel Hoffman.

1.11 Polarized Neutron Reflectometry Measurements

From the beginning, the primary focus of this research effort was the use of polarized neutron reflectometry (PNR) to examine the ferromagnetic ground state of $\text{Ga}_{1-x}\text{Mn}_x\text{As}$. PNR is a powerful experimental technique that can provide information about the depth-dependent chemical profile and depth-dependent vector magnetization profile

in thin films. The details of PNR will be presented in Chapter 2. Some of the questions that we wished to answer with PNR measurements were the following:

- *Is there moment canting in $Ga_{1-x}Mn_xAs$?*

At the time this research effort was started, it was experimentally well established that not all the Mn atoms in $Ga_{1-x}Mn_xAs$ were participating in the ferromagnetic exchange. We were intrigued by the possibility that this could be due to some sort of moment canting, or frustration effects that resulted in non-collinear alignment of the Mn magnetic moments, even at low temperature and under an applied magnetic field. PNR was the perfect tool for investigating this possibility, as it has the ability to detect components of a film's magnetization perpendicular to its net magnetization direction. After examining many $Ga_{1-x}Mn_xAs$ films of varying thickness, x , and annealing conditions, no *conclusive* evidence for coherent moment canting could be found. However, the measurements reported in this dissertation certainly do not *exclude the possibility* of non-collinear moments in our $Ga_{1-x}Mn_xAs$ films.

- *Are interfacial features important for $Ga_{1-x}Mn_xAs$ films?*

PNR is particularly sensitive to chemical and magnetic changes at interfaces between layers. That sensitivity, coupled with the possibility of some sort of surface diffusion during annealing provided a second motivation for using PNR to examine $Ga_{1-x}Mn_xAs$ films. This turned out to be a particularly interesting aspect of this study, as important annealing-dependent chemical and magnetic differences were found between as-grown and optimally annealed $Ga_{1-x}Mn_xAs$ films.

- *Is there a uniform distribution of magnetic moment?*

PNR is useful as a depth-dependent vector magnetometer. So, although we could not definitively detect the presence of any magnetization perpendicular to the overall magnetization, we were able to successfully establish depth profiles of the magnetization component parallel to net magnetization for $\text{Ga}_{1-x}\text{Mn}_x\text{As}$ films of varying thickness, x , and annealing conditions. These profiles produced the unexpected result that the as-grown films commonly feature a distinct gradient in the magnetization (increasing towards the free surface), a feature that is far less pronounced after annealing.

1.12 Inelastic Neutron Scattering Measurements

- *Can we detect spin waves in $\text{Ga}_{1-x}\text{Mn}_x\text{As}$?*

In addition to the PNR measurements, another important aspect of this work was an attempt to measure the spin wave dispersion in $\text{Ga}_{1-x}\text{Mn}_x\text{As}$ using inelastic neutron scattering. For these measurements, Furdyna's group produced a series of $\text{Ga}_{1-x}\text{Mn}_x\text{As}$ films ranging from $\sim 6 - 9 \mu\text{m}$ thick. To our knowledge, these ultra-thick samples are the thickest $\text{Ga}_{1-x}\text{Mn}_x\text{As}$ samples ever fabricated. However, despite this tour de force of sample growth, the very dilute nature of the magnetic moments made inelastic measurements exceedingly difficult. While some evidence of spin waves was found, results were inconclusive and did not reproduce well.

Chapter 2

Polarized Neutron Reflectometry

2.1 Introduction

Polarized neutron reflectometry (PNR) is the experimental technique employed most extensively in this study. With that in mind, this chapter will give a detailed overview of this technique. This overview will focus on three areas: elements of the theory underlying reflection of polarized neutrons, the instruments used for these experiments, and the data analysis techniques employed to interpret the data. The following theoretical account closely follows portions of the much more detailed treatments given by Majkrzak, O'Donovan, and Berk [35], and by Fitzsimmons and Majkrzak.[36] Another valuable reference is Felcher's pioneering 1981 work [37].

2.2 Reflection of Neutrons

Neutron scattering relies upon the quantum mechanical phenomenon of wave-particle duality. Neutrons act as waves when they interact with a sample material, and in doing so, they encode information about the structure or dynamics of that sample. But following those interactions, we are conveniently able to treat the scattered neutrons as particles, counting them individually as we extract their encoded information. When focusing on the wavelike properties of the neutron as it interacts with a material, it is sufficient to represent it as a three-dimensional plane wave

$$\Psi(\mathbf{k}, \mathbf{r}) = e^{i\mathbf{k}\cdot\mathbf{r}}, \quad (2)$$

where \mathbf{k} is the neutron wavevector, and \mathbf{r} is its position. For simplicity's sake, we will *temporarily* ignore the spin of the neutron. For the case of neutron reflectometry, we are concerned only with elastic scattering, which allows for description of neutron interactions in terms of the time-independent Schrödinger equation

$$\left[(-\hbar^2/2m_n)\nabla^2 + V(\mathbf{r})\right] \Psi(\mathbf{k}, \mathbf{r}) = E \Psi(\mathbf{k}, \mathbf{r}), \quad (3)$$

where \hbar is Planck's constant, m_n is the neutron rest mass, $V(\mathbf{r})$ is the scattering potential, and E is the total neutron energy. Assuming neutrons incident from a vacuum, there is no potential outside the sample

$$V(\mathbf{r}) = 0 \Rightarrow E_0 = \text{KE} = \hbar^2 k^2 / 2m_n. \quad (4)$$

Inside the sample, we consider a continuum of scatterers of number density N , such that

$$V(\mathbf{r}) = (2\pi\hbar^2/m_n) \sum N_j b_j = (2\pi\hbar^2/m_n)\rho_{nuc}, \quad (5)$$

where j sums over all the different elements in the sample, b is each element's characteristic nuclear scattering length, and ρ_{nuc} is the nuclear (also called chemical [38]) scattering length density (SLD). Since we're only worried about elastic processes,

$$E_0 = E \Rightarrow [\nabla^2 + k_0^2 - 4\pi\rho_{nuc}] \Psi(\mathbf{k}, \mathbf{r}) = 0. \quad (6)$$

The neutron energy inside the medium is

$$E = (\hbar^2 k^2/2m_n) + (2\pi\hbar^2/m_n) \rho_{nuc}, \quad (7)$$

and since the energy must be conserved from outside to inside,

$$k^2 = k_0^2 - 4\pi\rho_{nuc}. \quad (8)$$

This can be used to define the refractive index

$$n = k/k_0 = [1 - (4\pi\rho_{nuc}/k_0^2)]^{1/2}. \quad (9)$$

Defining k via Eq. 9 allows the Schrödinger equation to be rewritten as

$$[\nabla^2 + k^2] \Psi(\mathbf{k}, \mathbf{r}) = 0. \quad (10)$$

In a region of space with uniform but nonzero ρ_{nuc} , the solution to Eq. 10 takes the plane wave form described in Eq. 2. Reinserting that plane wave solution into Eq. 10, and considering Eq. 8 yields the following valuable identity,

$$k_x^2 + k_y^2 + k_z^2 + 4\pi\rho_{nuc} = k_{0x}^2 + k_{0y}^2 + k_{0z}^2. \quad (11)$$

Now consider the case of reflection from an infinitely broad, perfectly flat slab that extends in the z (the surface normal) direction with thickness δ . The slab is bounded by an infinite vacuum on either side ($\rho = 0$), and the SLD within the slab has no lateral dependence ($\rho_{nuc} = \rho_{nuc}(z)$). Since $d\rho_{nuc}/dx = d\rho_{nuc}/dy = 0$, conservation of momentum dictates that

$$k_x = k_{0x}, k_y = k_{0y} \Rightarrow k_z^2 = k_{0z}^2 - 4\pi\rho_{nuc}. \quad (12)$$

Plugging those substitutions back into the Schrödinger equation shows that the wave equation reduces to one dimension

$$[(\partial^2/\partial z^2) + k_{0z}^2 + 4\pi\rho_{nuc}(z)]\psi(z) = 0. \quad (13)$$

This shows that if there are no in-plane variations in SLD, the *specular* reflectivity (angle of incidence = angle of reflection) is the *only* possibility for reflection. This means that the incoming and outgoing wavevectors satisfy

$$|\mathbf{k}_i| = |\mathbf{k}_f|. \quad (14)$$

Additionally, the wavevector transfer is defined as

$$\mathbf{Q} = \mathbf{k}_f - \mathbf{k}_i, |\mathbf{Q}| = Q = 2k_0 \sin\theta = 4\pi \sin\theta / \lambda_0, \quad (15)$$

where λ_0 is the incoming neutron wavelength, and θ is the angle between \mathbf{k}_i and the x -axis. A diagram of the specular condition is shown in Figure 2.1. In reality, a sample always contains some in-plane variations. Generally, the result is that the specular reflectivity provides the depth-dependence of the SLD while *integrating over* all in-plane

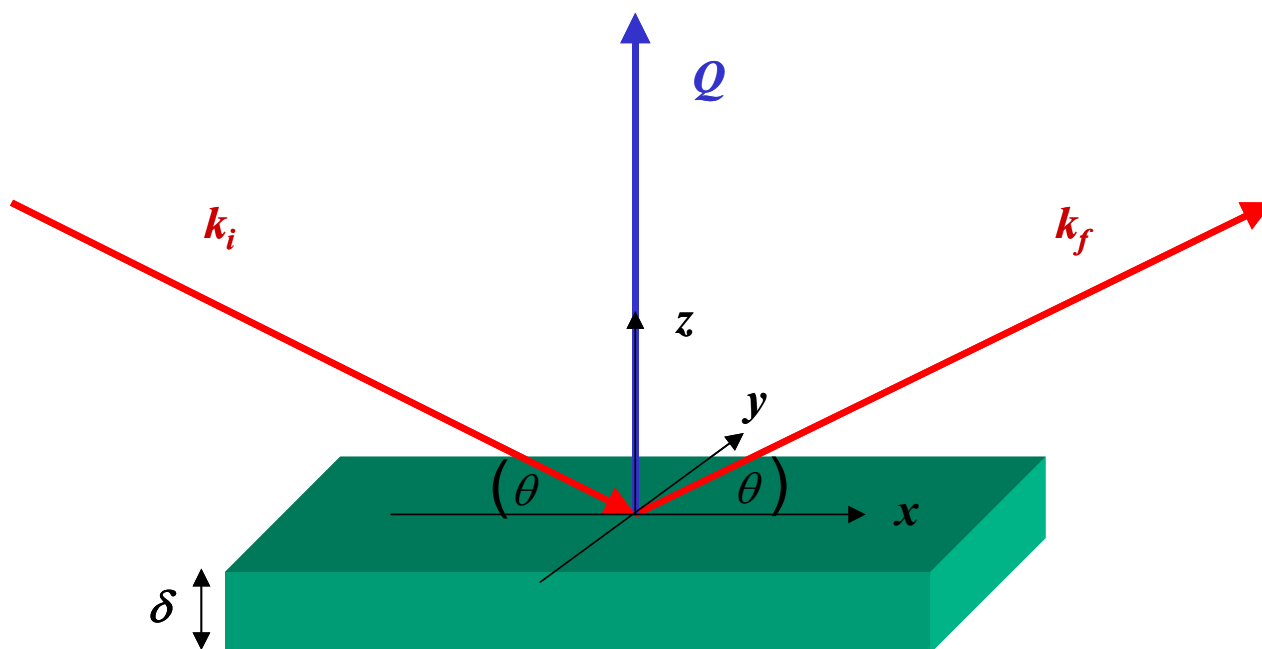


Figure 2.1: Diagram of the specular condition. Neutrons are reflected at the same angle at which they are incident, producing a Q -vector perpendicular to both in-plane coordinate directions. The specular reflectivity contains information about the *depth-dependence* of the sample's scattering length density. *In-plane* variations in scattering length density are integrated over.

inhomogeneities. Conversely, a great deal of in-plane information can be obtained by examining the off-specular reflectivity, but that is beyond the scope of this discussion.

For now, let us consider the case of a constant $\rho_{nuc}(z)$. Then, solving Eq. 13 for zero potential outside the slab (denoted region I and region III), and a constant potential inside the slab (denoted region II), this standard quantum mechanics transmission/reflection problem results in

$$\begin{pmatrix} t \\ ik_{III}t \end{pmatrix} e^{ik_{II}\delta} = \begin{pmatrix} \cos(k_{II}L) & \sin(k_{II}L)/k_{II} \\ -k_{II}\sin(k_{II}L) & \cos(k_{II}L) \end{pmatrix} \begin{pmatrix} 1+r \\ ik_I(1-r) \end{pmatrix}, \quad (16)$$

where the z subscripts have been dropped from the k 's, and those k 's are determined from Eq. 9. Additionally, t is the transmission amplitude, and r is the reflection amplitude.

For the case of a sample with a varying z -dependent potential, this formalism must be extended to incorporate multiple layers. This is done by dividing the slab into n number of bins j , each with a variable SLD. The resulting matrix equation can be expressed as

$$\prod_{j=n-1}^0 \mathbf{M}_j(\delta_j) \begin{pmatrix} 1+r \\ ik_0(1-r) \end{pmatrix} = \begin{pmatrix} t \\ ik_n t \end{pmatrix} \prod_{j=n-1}^0 e^{ik_n \delta_j} = \begin{pmatrix} t \\ ik_n t \end{pmatrix} e^{ik_n \Delta}, \quad (17)$$

where

$$\mathbf{M}_j(\delta_j) = \begin{pmatrix} \cos(k_j \delta_j) & \sin(k_j \delta_j)/k_j \\ -k_j \sin(k_j \delta_j) & \cos(k_j \delta_j) \end{pmatrix}, \quad (18)$$

and the total sample thickness is defined as the sum of the individual bin thicknesses

$$\Delta = \sum_{j=1}^{n-1} \delta_j . \quad (19)$$

Eq. 17 allows for calculation of a composite reflectivity amplitude r , which can be compared to the measured reflectivity, $R = |r|^2$. This formalism is obviously useful for discrete layers with sharply contrasting SLD, but with enough adequately small bins it can also approximate continuous changes in SLD. The bin size is a measure of the depth resolution of the SLD profile. The experimentally achievable depth resolution is largely determined by the maximum Q value of the data, so a good rule of thumb is that the bin size should not be too much smaller than π/Q_{max} . Eq. 18 is an *exact* calculation, and is referred to as “dynamical”, because it properly accounts for dynamical surface scattering of neutrons at very small angles (low- Q). A much simpler, alternative approach to calculating the reflectivity is to assume that the sample never significantly distorts the neutron wavefunction from its free-space form. This type of approximation is known as the Born approximation [39], and is considered “kinematic” instead of dynamic. While the Born approximation can be useful for qualitative analysis (as we will see later), or for describing features at high- Q , it fails catastrophically at low- Q .

2.3 Reflection of Polarized Neutrons

In the previous section, the magnetic moment of the neutron was ignored. However, the moment is of critical importance, as it allows neutron scattering to reveal magnetic properties of sample materials. By considering the magnetic interaction, we can move into the realm of *polarized neutron reflectometry* (PNR). In the presence of a magnetic field \mathbf{B} , the scattering potential from Eq. 5 is modified in the following way

$$V = V_{nuc} + V_{mag} = (2\pi\hbar^2/m_n) \rho_{nuc} \pm \boldsymbol{\mu} \cdot \mathbf{B} \quad (20)$$

where the magnetic moment vector is defined in terms of the neutron magnetic moment μ_n , the Pauli spin matrix $\boldsymbol{\sigma}$, and the nuclear magneton $\mu_N = 3.152 \times 10^{-8}$ eV/T,

$$\boldsymbol{\mu} = \mu_n \boldsymbol{\sigma} = -1.913 \mu_N \boldsymbol{\sigma}. \quad (21)$$

In matrix notation,

$$V(z) = \frac{2\pi\hbar^2}{m_n} \begin{pmatrix} \rho_{nuc} & 0 \\ 0 & \rho_{nuc} \end{pmatrix} \mp \mu_n \begin{pmatrix} B_z & B_x - iB_y \\ B_x + iB_y & -B_z \end{pmatrix}, \quad (22)$$

where “-” corresponds to when the neutron spin is parallel to \mathbf{H} , and “+” corresponds to when the neutron spin is antiparallel to \mathbf{H} . Maxwell’s equations dictate

$$\mathbf{B} = \mu_0 \mathbf{H} + \mathbf{m}, \quad (23)$$

where $\mu_0 = 4\pi \times 10^{-7}$ T·m·A⁻¹ is the permeability of free space, \mathbf{H} is the laboratory magnetic field of reference, and \mathbf{m} is the intensity of magnetization. PNR is sensitive to contrast in \mathbf{m} , so for fields applied in the y -direction (as in Fig. 2.1) we consider the potential difference across an interface

$$\delta V(z) = \frac{2\pi\hbar^2}{m_n} \begin{pmatrix} \rho_{nuc} & 0 \\ 0 & \rho_{nuc} \end{pmatrix} \mp \mu_n \begin{pmatrix} m_z & m_x - im_y \\ m_x + im_y & -m_z \end{pmatrix}, \quad (24)$$

where $\mathbf{m} = m_x \mathbf{x} + m_y \mathbf{y} + m_z \mathbf{z}$, is the sample magnetization.

From Eq. 20, the magnetic SLD can be defined in terms of a magnetic scattering length p ,

$$\rho_{mag} = \sum N_i p_i = C \sum N_i \boldsymbol{\mu}_i = C' \mathbf{M}, \quad (25)$$

where M is the sample magnetization, $C = 2.695 \times 10^{-5}$ Å· μ_B^{-1} and $C' = 2.9 \times 10^{-9}$ emu⁻¹·cm³·Å⁻². In terms of SLD, the potential difference becomes

$$\delta V(z) = \frac{2\pi\hbar^2}{m_n} \begin{pmatrix} \rho_{nuc} + \rho_{mag}^z & \rho_{mag}^x - i\rho_{mag}^y \\ \rho_{mag}^x + i\rho_{mag}^y & \rho_{nuc} - \rho_{mag}^z \end{pmatrix}. \quad (26)$$

The elements of the matrix in Eq. 26 can be recast in terms of spin-flip (incoming and scattered neutrons with opposite spin, designated ++ and --) and non spin-flip (incoming and scattered neutrons with the same spin, designated +- and -+) scattering events

$$\rho_{++} = \rho_{nuc} + \rho_{mag}^z, \rho_{--} = \rho_{nuc} - \rho_{mag}^z, \rho_{+-} = \rho_{mag}^x - i\rho_{mag}^y, \rho_{-+} = \rho_{mag}^x + i\rho_{mag}^y,$$

$$\Rightarrow \delta V(z) = \frac{2\pi\hbar^2}{m_n} \begin{pmatrix} \rho_{++} & \rho_{+-} \\ \rho_{-+} & \rho_{--} \end{pmatrix}. \quad (27)$$

Solving the Schrödinger equation for the above potential results in

$$\Psi(z) = U_+ \begin{pmatrix} 1 \\ 0 \end{pmatrix} \psi_+(z) + U_- \begin{pmatrix} 0 \\ 1 \end{pmatrix} \psi_-(z), \quad (28)$$

where

$$\psi_+(z) = \exp(ik_+z), \psi_-(z) = \exp(ik_-z), \quad (29)$$

and the refractive index is birefringent

$$n_{\pm} = \frac{k_{\pm}}{k_0} = \sqrt{1 - \frac{4\pi(\rho_{nuc} \pm \rho_{mag})}{k_0^2}}. \quad (30)$$

Consider the generalized case of sample spins with in-plane components of \mathbf{M} parallel and perpendicular to \mathbf{H} applied in-plane (see Fig. 2.2).

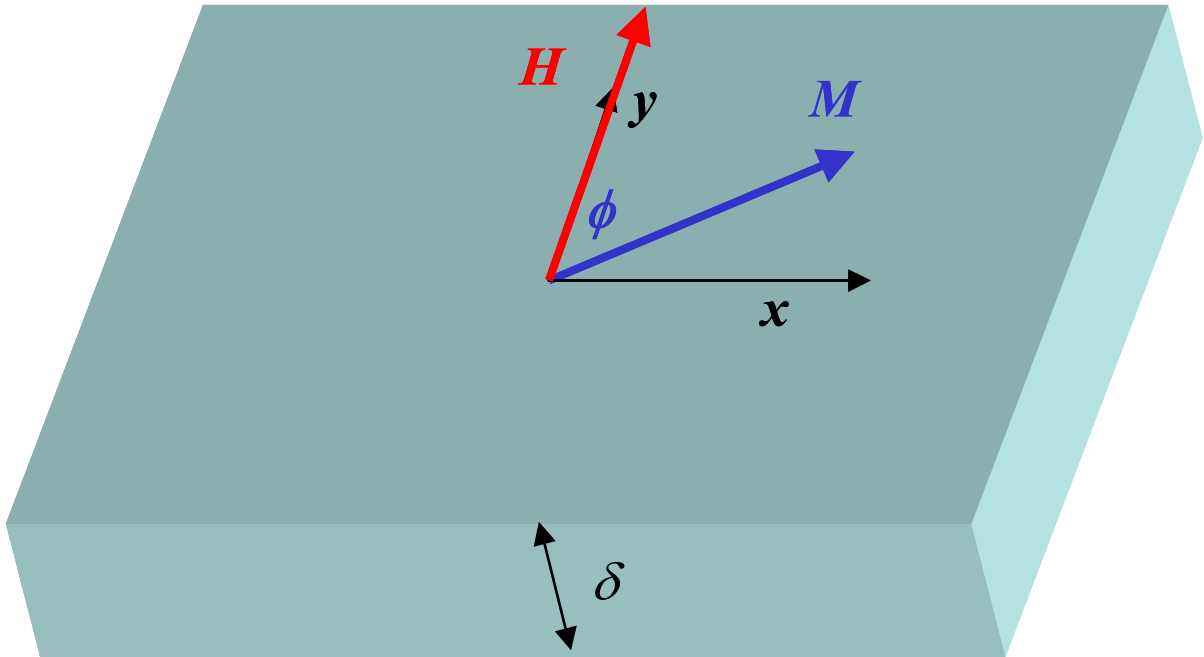


Figure 2.2: PNR is sensitive to components of the in-plane sample magnetization both parallel and perpendicular to the applied field. Since PNR is also sensitive to the depth-dependence of the magnetization, this technique provides a method of depth-dependent vector magnetometry.

With spin-dependence accounted for, the “polarized” analogue of Eq. 18 is

$$\prod_{j=n-1}^0 A_j \begin{pmatrix} I_+ + r_+ \\ I_- + r_- \\ i k_0 (I_+ - r_+) \\ i k_0 (I_- - r_-) \end{pmatrix} = \begin{pmatrix} t_+ \\ t_- \\ i k_n t_+ \\ i k_n t_- \end{pmatrix}, \quad (31)$$

where I_+ (I_-) is the incident fraction of neutrons parallel (antiparallel) to \mathbf{H} , and the elements A_{ij} are

$$A_{11} = 2\eta[\gamma_3 \cosh(S_+ \delta_j) - \gamma_1 \cosh(S_- \delta_j)] = A_{33}, \quad (32)$$

$$A_{21} = 2\eta[\gamma_1 \gamma_3 \cosh(S_+ \delta_j) - \gamma_1 \gamma_3 \cosh(S_- \delta_j)] = A_{43}$$

$$A_{31} = 2\eta[S_+ \gamma_3 \cosh(S_+ \delta_j) - S_- \gamma_1 \cosh(S_- \delta_j)],$$

$$A_{41} = 2\eta[S_+ \gamma_1 \gamma_3 \cosh(S_+ \delta_j) - S_- \gamma_1 \gamma_3 \cosh(S_- \delta_j)],$$

$$A_{12} = 2\eta[-\cosh(S_+ \delta_j) + \cosh(S_- \delta_j)] = A_{34}$$

$$A_{22} = 2\eta[-\gamma_1 \cosh(S_+ \delta_j) + \gamma_3 \cosh(S_- \delta_j)] = A_{44}$$

$$A_{32} = 2\eta[-S_+ \sinh(S_+ \delta_j) + S_- \sinh(S_- \delta_j)],$$

$$A_{42} = 2\eta[-S_+ \gamma_1 \sinh(S_+ \delta_j) + S_- \gamma_3 \sinh(S_- \delta_j)],$$

$$A_{13} = 2\eta[(\gamma_3 / S_+) \sinh(S_+ \delta_j) - (\gamma_1 / S_-) \sinh(S_- \delta_j)],$$

$$A_{23} = 2\eta[(\gamma_1 \gamma_3 / S_+) \sinh(S_+ \delta_j) - (\gamma_1 \gamma_3 / S_-) \sinh(S_- \delta_j)],$$

$$A_{14} = 2\eta[(-1 / S_+) \sinh(S_+ \delta_j) + (1 / S_-) \sinh(S_- \delta_j)],$$

$$A_{24} = 2\eta[(-\gamma_1 / S_+) \sinh(S_+ \delta_j) + (\gamma_3 / S_-) \sinh(S_- \delta_j)],$$

where,

$$S_{\pm} = i n_{\pm} k_0,$$

$$\gamma_1 = (2|\rho_{mag}| + \rho_{--} - \rho_{++} + 2\rho_{+-}) / (2|\rho_{mag}| - \rho_{--} + \rho_{++} + 2\rho_{+-}),$$

$$\gamma_3 = (2|\rho_{mag}| - \rho_{--} + \rho_{++} - 2\rho_{+-}) / (2|\rho_{mag}| + \rho_{--} - \rho_{++} - 2\rho_{+-}),$$

Eq. 31 allows for calculation of four neutron spin reflectivities, two non spin-flip (NSF), and two spin-flip (SF): R_{++} (NSF, neutron spin parallel to \mathbf{H}), R_{--} (NSF, neutron spin antiparallel to \mathbf{H}), R_{+-} (SF, incoming spin parallel to \mathbf{H} , scattered spin antiparallel), and R_{-+} (SF, incoming spin antiparallel to \mathbf{H} , scattered spin parallel).

A qualitative understanding of what information can be obtained from measuring these four reflectivities can be obtained by considering the Born approximation. This gives

$$\begin{aligned} \text{NSF: } R^{\pm\pm}(Q) &\propto \left[\int_0^4 [\rho_{nuc}(z) \pm \rho_{mag}(z) \cos \phi(z)] \exp(iQ_z z) dz \right]^2, \\ \text{SF: } R^{\pm\mp}(Q) &\propto \left[\int_0^4 [\rho_{mag}(z) \sin \phi(z)] \exp(iQ_z z) dz \right]^2, \end{aligned} \quad (33)$$

where ϕ is the angle between \mathbf{H} and \mathbf{M} . Eq. 33 provides the “take-home” messages:

A) The depth-dependent, in-plane sample magnetization parallel to \mathbf{H} , is given by the *difference* in the NSF reflectivities, spin up - spin down ($R_{++} - R_{--}$).

B) The depth-dependent, in-plane sample magnetization perpendicular to \mathbf{H} is given by either of the SF reflectivities (R_{+-} or R_{-+}).

So, it can be seen that measurement of all four neutron reflectivities makes PNR a tool for measuring *depth-dependent vector magnetization*.

2.4 PNR Measurements

While the reflection of polarized neutrons is certainly a quantum mechanical phenomenon, an actual PNR experiment can be understood fairly well in terms of a classical optical experiment (with the nontrivial exception of the magnetic polarization!). Neutrons of a particular “color” (wavelength) are magnetically polarized, and are specularly reflected from the sample as a function of scattering angle θ . After reflection, the spin polarization is analyzed by keeping only neutrons corresponding to one particular spin state, and throwing the rest away. The resulting neutron intensity is then measured with a detector. Since θ corresponds to Q (Eq. 15), measuring the reflected intensity as a function of increasing θ provides SLD information corresponding to progressively smaller length scales. Furthermore, by alternating the incoming and

analyzed neutron spin polarizations, we can specifically measure each of the SF and NSF reflectivities, which as discussed above, provide the depth-dependent vector magnetization.

2.5. NG-1 Reflectometer

The vast majority of the PNR measurements described in this dissertation were performed on the NG-1 Reflectometer at the NIST Center for Neutron Research (NCNR). A schematic of the NG-1 Reflectometer is shown in Fig. 2.3. Since the neutron source at the NCNR is a 20 MW reactor, a *continuous stream* of neutrons with a Maxwellian distribution of wavelengths is available to NCNR instruments. The NG-1 beamline is on a neutron guide that is illuminated by a liquid hydrogen cold source that shifts the peak energy of the Maxwellian distribution to longer wavelengths (lower energy). By utilizing longer wavelength neutrons, higher resolution in Q (wavevector transfer) is achievable. The cold neutrons in the guide intersect a vertically focusing pyrolytic graphite monochromator. The monochromator selects out only neutrons of a particular wavelength (for the NG-1 Reflectometer, 4.75 Å), and redirects them towards the reflectometer apparatus. The intensity of the monochromated beam is then recorded by a neutron monitor before passing through a pair of collimating slits. Next, spin polarization of the beam is achieved via a Fe/Si supermirror, which (with over 90% efficiency) scatters out of the transmitted beam all neutrons with spin states other than spin down (with respect to the plane of the mirror). Following the polarizing supermirror is a DC magnetic spin flipper, which (when activated) produces a magnetic field that

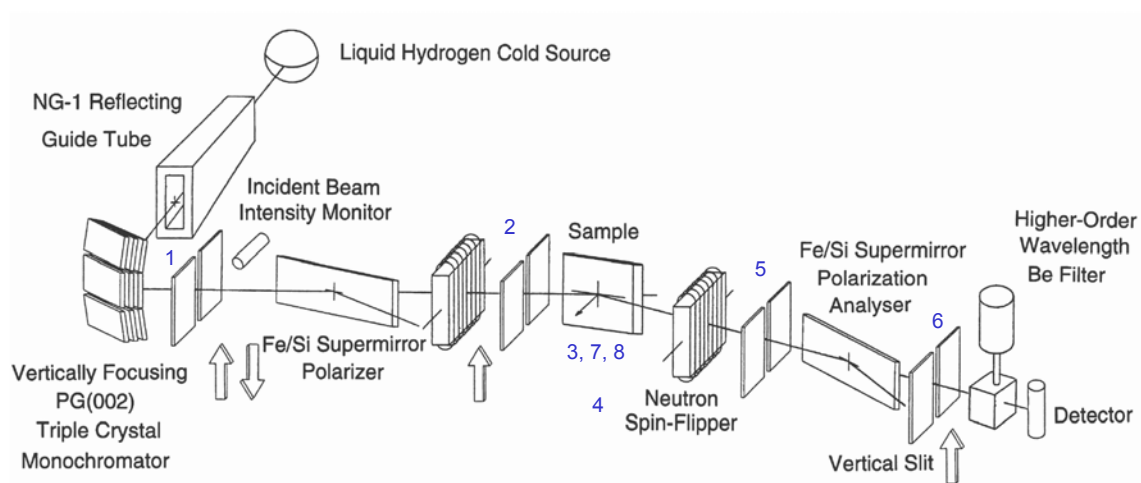


Figure 2.3: Schematic of the NG-1 Reflectometer. The numbers correspond to the control motors: 3 - scattering angle (θ), 4 - detector arm angle (2θ), 7 - sample translation, 8 - sample tilt angle, 1, 2, 5, 6 - slits. Figure taken from Ref. 35.

causes the neutron spin to precess 180° . Depending on whether it is on or off, the spin-flipper produces a beam of either spin-up or spin-down neutrons. Following another set of collimating slits, the neutron beam reflects from the sample (housed in an aluminum dispex sample can). Via the sample table, the sample can be rotated about θ , translated (approximately along the sample plane normal) and tilted about the sample's in-plane horizontal axis. The sample is surrounded by an electromagnet, which produces a vertical magnetic field H in the plane of the sample. On either side of the sample is room for addition of small bar magnets, which are used to provide guide fields to maintain polarization of the beam. The reflected beam from the sample is then passed through another spin-flipper/slits/polarizing mirror/slits assembly which allows for analysis of all four of the previously discussed spin-dependent reflectivities. The analyzed beam is transmitted through a Be filter (to remove λ/n higher order wavelengths that may have passed through the monochromator) before being incident on a horizontally narrow "pencil" detector, which measures the reflected intensity. A photograph of the upstream end of the reflectometer is shown in Fig. 2.4, and a close-up of the sample container and magnet housing is shown in Fig. 2.5.

Manipulation of the reflectometer slits, scattering angles, and sample translation is performed via eight motors (labeled on Fig. 2.3), which are computer controlled using Instrument Control Program (ICP) [40] software.

The NG-1 experiments we performed typically involved the following steps:

- 1) **Slitscan:** Collimating slits, H , and temperature were all set to the values to be used in the experiment, and an appropriate "slitscan" was taken. This involved rotating the



Figure 2.4: Photograph of the upstream end of the NG-1 Reflectometer. Some points of interest include: a) the front polarizing supermirror, b) the front DC spin flipper, c) the sample table (motors 3, 7, and 8), d) gear controlling the detector arm (motor 4), e) the electromagnet (sample can is visible in the hole). Picture courtesy J. S. Lee of the Korea Atomic Energy Research Institute.



Figure 2.5: Close-up photograph of the electromagnet sample housing. The cold finger containing the sample is shown between the two poles of the electromagnet. A stack of guide field magnets is visible in the foreground. Courtesy J. S. Lee of the Korea Atomic Energy Research Institute.

detector arm into the main beam, and translating the sample out of the beam, before measuring all four reflectivity cross sections. The slitscan was used to establish the difference in polarization efficiency upstream and downstream of the sample (i.e. the front and back flipping ratios).

2) **Alignment:** The detector arm was rotated into the main beam, and the high intensity position was found. This angle was set to be $2\theta = 0^\circ$, and defined the detector arm alignment. The sample was then translated into the main beam, and the sample angle was rotated until a maximum was found. This maximum crudely defined $\theta = 0$. For most materials, the critical θ (maximum angle of total external reflection) occurs near 0.25° . With this in mind, the detector arm was rotated to $2\theta = 0.5^\circ$, and the sample angle was rotated to $\theta = 0.25^\circ$, a position known as the “specular ridge”. While at the specular ridge, θ , the translation, and the tilt were all optimized. The maximum intensity position was then redefined to be $\theta = 0.25^\circ$.

3) **Specular Scans:** All four reflectivities were individually measured as a function of θ , while keeping the detector arm in a position equal to 2θ . Since the reflected intensity commonly falls off approximately as Q^4 , counting times were increased with increasing θ , in order to provide comparable statistics.

4) **Background Scans:** Background scattering was measured by repeating the specular scans (generally with reduced point density) but with θ offset by 0.3° .

2.6 POSY-I Reflectometer

In addition to the experiments on NG-1, a few measurements were conducted on the POSY-I polarized neutron reflectometer [41, 42] at Argonne National Laboratory’s

Intense Pulsed Neutron Source (IPNS). The primary difference between measurements at IPNS as compared to the NCNR is that IPNS is a *pulsed source*, which produces monochromatic bursts of neutrons instead of a steady stream. POSY-I exploits the pulse structure by fixing θ while simultaneously measuring a spectrum of wavelengths λ . By examining Eq. 15, one can see that varying λ with θ fixed serves to vary Q , just as varying θ with λ fixed varies Q in a continuous source experiment. While there are some differences at a pulsed source (different methods for spin-flipping, for example), pulsed PNR experiments are fairly similar to those at a continuous source. With that in mind, and since only a very few of the measurements in this dissertation were taken at IPNS, a more detailed description of POSY-I will not be outlined here. References 36, 41, and 42 are good resources for more details concerning PNR at pulsed sources.

2.7 Data Corrections

The first step in processing the data is to understand the statistical uncertainty.

The uncertainty associated with the reflectivity is

$$\Delta R = R^{1/2}. \quad (34)$$

Before it can be properly analyzed, the raw data must go through a series of refinements.

For the NG-1 measurements described in this dissertation, data refinement included the following steps (in which error propagation was accounted for):

1) Background Subtraction. The previously described background scans were subtracted from the specular scans. The background for most of our measurements appeared to be largely instrumental noise, but also likely included some off-specular

scattering resulting from in-plane sample inhomogeneities. The background we observed was generally not sample-dependent, as background scans taken with the same slit settings for different samples were commonly identical within statistics.

2) Polarization Corrections. In order to accurately gauge the intensities of the four spin-dependent reflectivities, the efficiencies of the polarizing supermirrors and spin flippers must be accounted for. This efficiency information is provided by the slitscan, and from the two SF reflectivities.

3) Footprint Correction. The illumination of the sample changes as it is rotated, and that must be accounted for. Since our measurements did not involve varying slits as a function of θ , and our samples were assumed to be fully engulfed in the beam for all θ , the footprint corrections were fairly straightforward. The positively sloping region near the critical edge of an NSF reflectivity curve (Fig. 2.6) would be flat, if not for the change in sample illumination. So, a line is fitted to this region, and is used to correct the data such that the formerly sloping region is flat. This correction is then applied to the other reflectivities.

The corrections to most of the PNR data in this dissertation were applied using the Reflred [43] software package.

2.8 Data Analysis

Once the data has been properly processed, some qualitative assessments of the corrected data can be made. For example, consider the corrected set of NSF R_{++} and $R_{..}$.

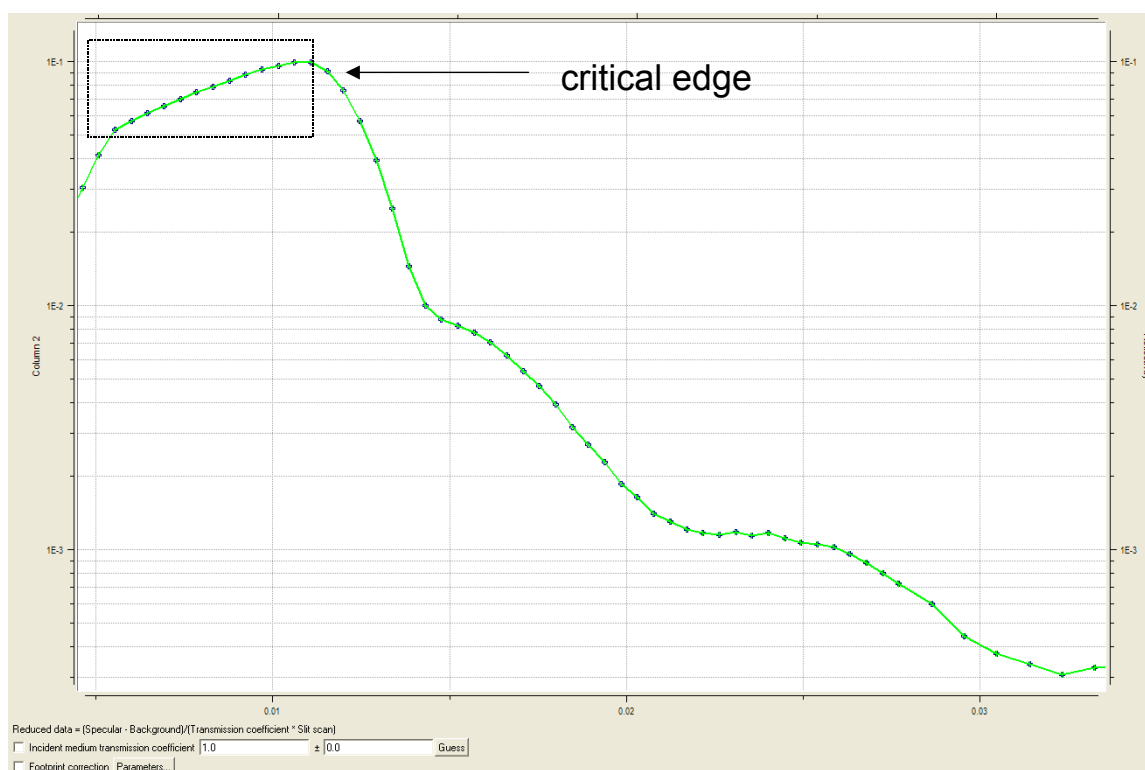


Figure 2.6: Log-scale plot of reflectivity as a function of Q (\AA^{-1}) illustrating the pre-footprint correction critical edge region. If not for Q -dependent sample illumination, the boxed region would be flat.

data (taken from a $\text{Ga}_{1-x}\text{Mn}_x\text{As}$ film) shown in Fig. 2.7. Some of the important features in this figure are:

- 1) **Critical Edge.** Position of this feature is determined by the summed SLD's of the layers. Typically, the critical edge is primarily determined by the SLD of the substrate, since it's usually the thickest layer by orders of magnitude.
- 2) **Periodicity of Fringes.** Dependent on the thickness of contrasting layers.
- 3) **Amplitude of Fringes.** Determined by SLD contrast between layers.
- 4) **Spin-Up & Spin-Down Splitting.** Results from sample magnetization. Magnitude of splitting as a function of Q is roughly related to the magnetization at different length scales.
- 5) **Fringe Attenuation.** Comes from roughness in SLD between contrasting layers. Sharply contrasting interfaces produce little attenuation, while "blurry" interfaces can greatly reduce the high Q intensity, and alter the fringe periodicity.

The spin-flip reflectivities are more difficult to understand in a qualitative, straightforward fashion. For the purposes of this dissertation, it is enough to say that detection of large SF intensity (at or near the NSF intensity near the NSF critical edge) that remains above background levels for a reasonable region of Q (multiple SF fringes) would suggest significant magnetic moment canting. As will be explained in the next chapter, we were unable to detect *definitive*, reproducible evidence of moment canting in any of our $\text{Ga}_{1-x}\text{Mn}_x\text{As}$ samples (which is not to say we can *rule out* moment canting!). For this reason, SF analysis is not given as thorough a treatment as NSF analysis.

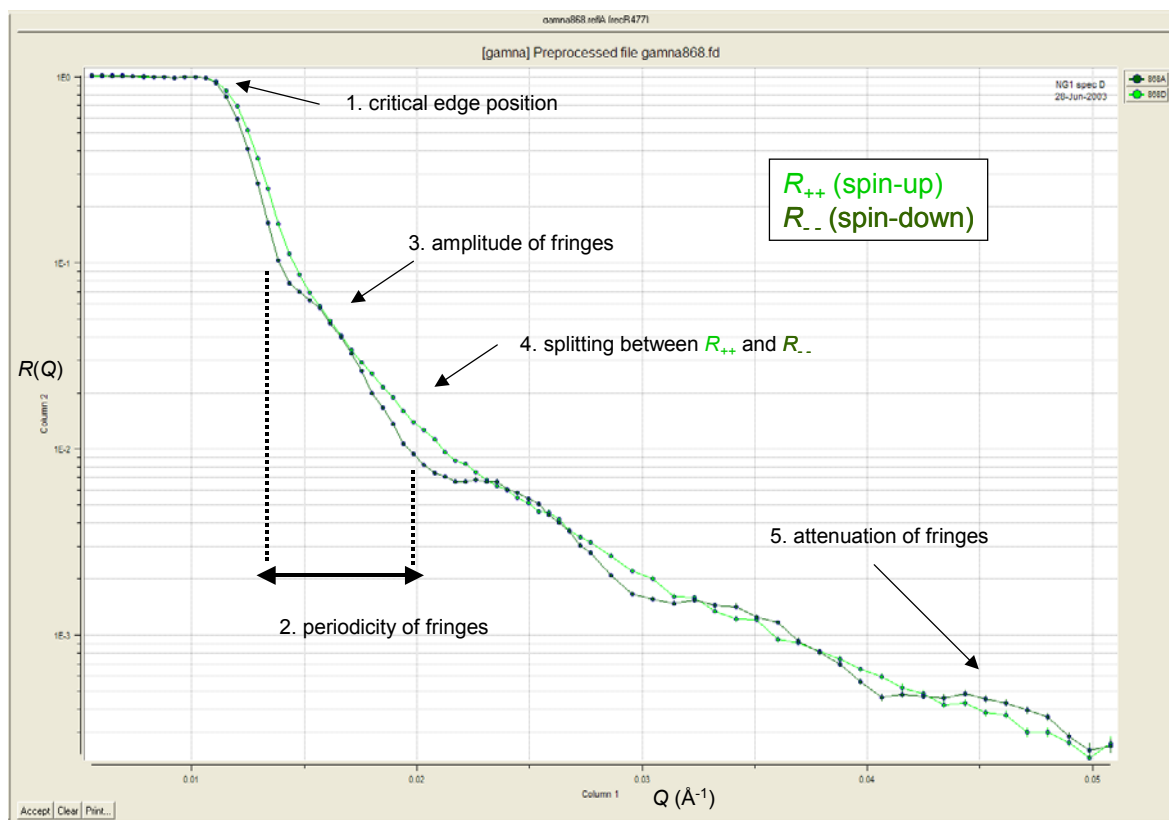


Figure 2.7: Example of corrected NSF PNR data. A great deal can be ascertained from qualitative assessment of features in the data.

Quantitative information is typically obtained by employing a nonlinear least-squares numerical analysis (corresponding to the theoretical formalism described above) to fit the PNR data. Most of the PNR data described in this dissertation was fit using the Reflpol software package, [43] which is based on algorithms developed by Ankner in the 1980's [44]. Reflpol fits the PNR data using the following parameters for each layer of a SLD model:

1) QC (\AA^2). The square of the critical edge position for the layer. Solving Eq. 9 for Q ($Q = 2k_0$) when $k_0 = 4\pi\rho_{nuc}$, defines the critical edge, and gives $Q^2_C = 16\pi\rho_{nuc}$. This means that varying this parameter is the same as varying the nuclear SLD.

2) D (\AA). Layer thickness corresponding to the nuclear SLD.

3) R0 (\AA). Roughness in QC (nuclear SLD) between the layer and the layer above it. This value should not exceed the thickness of the layer, or the layer above it.

4) MU (\AA^{-1}). Layer absorption. For the materials considered in this study, this was assumed to be a negligible variable, and was kept fixed.

5) QM (\AA^2). Square of the magnetic critical edge position for the layer. Since $Q^2_C = 16\pi\rho_{mag} = 16\pi C'M$ (by the same argument as for QC), varying this parameter is the same as varying the layer magnetization.

6) DM (\AA). Magnetic layer thickness. For our purposes, this was always fixed to be the same as the nuclear layer thickness.

7) RM (\AA). Roughness in QM (magnetization) between the layer and the layer above it. This value should not exceed the thickness of the layer, or the layer above it.

8) TH (deg). Moment canting angle. 270° is taken to be parallel to the applied field H . Fitting this parameter requires fitting SF data. Since the SF data is taken to be too small to accurately fit for the data in this study, TH is kept fixed at 270° .

Furthermore, Reflpol accounts for the following beam parameters that apply to all layers:

9) Intensity. Defines the normalization of the maximum beam intensity. Taken to be 1 for all the fits in this study.

10) Background. Adds a constant background to the data. Not used in this study (value set to $1e-10$), as the data are background subtracted.

11) Wavelength (Å). Wavelength of the incident beam. $\lambda = 4.75 \text{ \AA}$ for all data in this study.

12) Wavelength Divergence (Å). Accounts for any Q -independent uncertainty. We assume this to be fairly well defined, so this parameter was kept fixed at 0.021 for all data in this study.

13) Angular Divergence (rad). Accounts for any Q -dependent uncertainty. This not only includes the uncertainty in Q , but also “blurring” resulting from warping of the sample. This parameter was varied to correctly fit the “falloff” of the reflectivity immediately after the critical edge, and varied from 0.0005 to 0.0010 for the fits in this study.

The values of these parameters that fit the data define a SLD model representative of the sample. However, it should be made abundantly clear that finding a particular model to fit the data, *does not* imply that is the *only* model that will fit the data. In fact, uniqueness of a given solution is fundamentally hindered by the fact that reflectometry

measures *the square* of the reflected wavefunction, which means phase information is lost (there are schemes for getting around this in specific situations [45], but these methods are not applicable to our measurements). In practice, the best that can typically be done is to find the best fit possible using a SLD model that is *consistent* with the measured data, *and* is physically reasonable. When other physically reasonable models are found that fit the data equally or close to equally as well, it serves to establish uncertainty in the parameters that differ among the competing models.

Chapter 3

Annealing-Dependence of the $\text{Ga}_{1-x}\text{Mn}_x\text{As}$ Depth Profile

3.1 Introduction

This chapter will discuss polarized neutron reflectometry (PNR) measurements of $\text{Ga}_{1-x}\text{Mn}_x\text{As}$ films that show significant increases in Curie temperature and net magnetization after annealing. The aim of these experiments was to search for depth-dependent changes that occur during annealing, with the hope of better understanding the mechanisms that enhance the ferromagnetic exchange. The focus will be on three separate sets of samples that were all grown together at *nominally* the same growth temperature, and were annealed under similar conditions. Annealing was found to significantly alter the chemical and magnetic depth profiles of two of these sets, while it had little effect on the depth profiles of the other. The Reflpol [Section 2.7] parameters defining each of the models shown in this chapter are summarized in Appendix A.

3.2 Sample Preparation

The samples for this study were provided by Professor Jacek Furdyna's group at the University of Notre Dame. Using molecular-beam epitaxy, they fabricated $\text{Ga}_{1-x}\text{Mn}_x\text{As}$ films via the following steps:

- 1) 300 nm GaAs buffer layer was deposited on [001] GaAs substrate at ~ 580 °C.
- 2) The substrate was cooled to ~ 210 °C, and a 3 nm GaAs buffer layer was deposited.
- 3) While still at ~ 210 °C, a $\text{Ga}_{1-x}\text{Mn}_x\text{As}$ layer was grown.
- 4) Following growth, the resulting film was cleaved into pieces - one piece for annealing, and one piece to be left as-grown.
- 5) Annealing took place at ~ 270 °C, for about 1 hour, in a N_2 environment.
- 6) The films were further divided, providing specimens for characterization at Notre Dame, and pieces for PNR measurements.

The resulting samples were typically 2 cm x 2 cm in area. The Mn_{Ga} concentration x , in the $\text{Ga}_{1-x}\text{Mn}_x\text{As}$ films was established by using x-ray diffraction (XRD) to measure the change in lattice parameter a , from that of regular GaAs [46]. This method is not universally robust [47], as variations in growth parameters among different growers can change the relationship between a and x . However, if calibrated by another type of measurement (in our case particle induced x-ray emission), XRD can provide a reasonable relation between a and x . For our samples, we used the relation,

$$a(x) = (5.65469 + 0.24661x) \text{ \AA}. \quad (35)$$

This uncertainty associated with determination of x in this way is $\sim \pm 0.01$. The bulk magnetic properties of the samples were also characterized at Notre Dame, using magnetotransport measurements and/or SQUID magnetometry. Given extensive results

from other samples, the magnetic easy axis of these samples was assumed to lie along the [100] directions (any sample diagonal).

3.3 Sample Weirdness

The $\text{Ga}_{1-x}\text{Mn}_x\text{As}$ samples discussed in this dissertation displayed some strange features that should be noted. During alignment of the angle of reflection θ in a PNR experiment (see Section 2.4), it is expected to be able to optimize the instrument such that scanning θ (a “rocking curve”) results in a narrow Gaussian distribution of intensity peaked about the critical angle of reflection. However, we consistently observed significant “shoulders” in these peaks, even when the instrument alignment had been exhaustively optimized. Figure 3.1 shows an example rocking curve illustrating this point. The likely explanation for these shoulders is sample warping due to the way the sample was fastened. The bottom of the sample was covered by an aluminum pad (transparent to neutrons), and was attached to the sample holder using a screw. The broadness of the θ rocking curve tended to increase with increasing tightness of this screw, suggesting that the application of non-uniform pressure was bending the sample (GaAs is highly flexible). As the sample cooled, the screw became tighter, warping it further, and making the shoulder more prominent. So, the game was to attach the sample as loosely as possible, but to make sure that it was held tightly enough to prevent it from falling off! Typically, the broadness of the θ rocking curve also corresponded to the value of the angular resolution parameter needed to accurately fit the data (see Section 2.7).

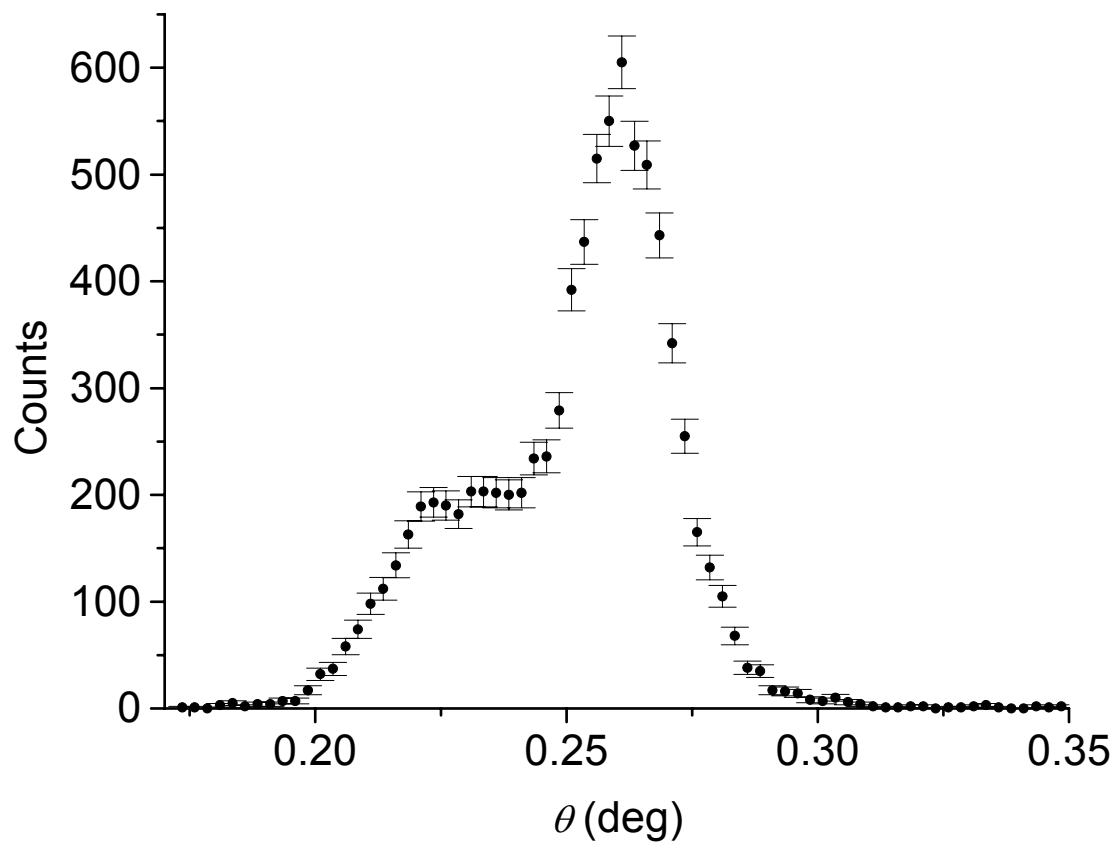


Figure 3.1: Example rocking curve illustrating the “shoulder” present in scans about the critical angle. Shoulders such as this are likely due to warping of the samples.

Translation alignment also proved tricky with these samples. We found that seemingly insignificant changes in translation could cause very noticeable changes in the θ position of the critical edge. Since the critical θ provides the value of the substrate SLD (see Section 2.7), our solution was to try and “tune” the translation such that the critical edge corresponded to the expected value for our GaAs substrates. This was mainly for arbitrary aesthetic purposes, as these errors did not significantly affect the points of interest, namely the chemical SLD [38] *difference* between the substrate and the rest of the film, and the magnetic SLD. However, there are small differences in the values of the substrate SLD in the models to be presented, which should be ignored. These differences are due to variations in tuning the critical θ , and not due to real differences in SLD

Additionally, PNR measurements consistently found a small region just below the critical edge where the background scattering was *larger* than the specular reflectivity. Figure 3.2 illustrates an example of this. This increased off-specular scattering could be related to the previously discussed sample warping, or could be indicative of some in-plane inhomogeneity of these samples. While this might be an interesting avenue to pursue elsewhere, it can be ignored for the purposes of discussing the specular reflectivity. This bizarre region occurs at Q -values below what is considered during fitting, and is removed before analysis.

Another point to consider when discussing in-plane inhomogeneity, is that the films may not be grown perfectly flat in the first place. Films grown by the Notre Dame group are known to have some unevenness in thickness from the center to the edges [48].

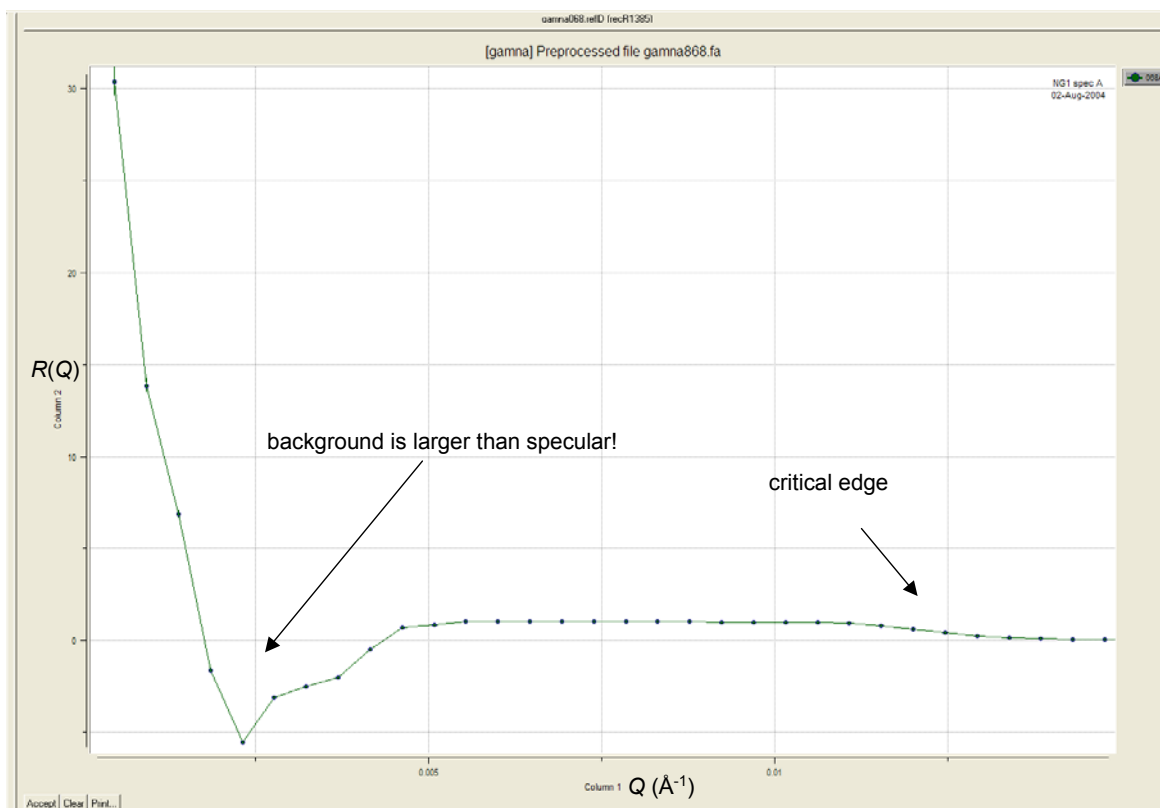


Figure 3.2: Example of corrected data with a region of unusually large background scattering.

However, they have found that their in-sample thickness difference is 5% or less, and is typically more like 1 %. So, in principle, this lack of flatness could account for a maximum of 5 nm of interfacial roughness in a 100 nm film, but it cannot explain differences observed between as-grown/annealed pairs. Furthermore, warping induced roughness could produce differences for an as-grown/annealed pair for one set of scans (from differences in screw tightness), but it is highly unlikely that it would do so in a *reproducible* fashion. In the following discussions, the presence of large magnetic gradients will be an important topic. We have discounted the idea that sample warping or uneven thickness could be significantly contributing to these magnetic gradients could be due solely to sample warping or uneven thickness because the data is *incompatible* with a comparable gradient in chemical composition.

3.4 Measurement Difficulties

This study was intrinsically challenging due to the very dilute concentration of Mn in these films. Because of this, the chemical (nuclear) SLD between $\text{Ga}_{1-x}\text{Mn}_x\text{As}$ and GaAs is not very different ($\sim 4\%$ different or less). This means that there was little chemical contrast between the film and the sample, damping the reflectivity oscillations. Fortunately, the magnetic nature of the films produced some additional contrast with the substrate, and introduced polarization-dependent differences in the reflectivity that provided additional information. Unfortunately, these films weren't *very* magnetic ($M \approx 20\text{-}50 \text{ emu}\cdot\text{cm}^{-3}$), making the polarization-dependent differences somewhat small.

Essentially, looking for depth-dependent changes in these films was like looking for a polar bear in a snowstorm (albeit a *magnetic* polar bear). Obtaining good data under

these circumstances required long counting times (sometimes up to a week for one sample under one set of conditions), and elimination of normally acceptable errors in instrument alignment. These measurements were not “business as usual” on NG-1 at the NCNR - we were pushing the limits of the technique. With each measurement, we became better at optimizing the experiments over the year and a half span of this project. However, the result is that not all of the data presented here is of equal quality. Where pertinent, these differences in quality will be pointed out.

3.5 Set A: Annealing Dependence in a 50 nm Film

The first as-grown/annealed $\text{Ga}_{1-x}\text{Mn}_x\text{As}$ pair we’ll consider provides the clearest evidence of an annealing-dependent depth profile, and will be denoted as “set A”. Set A has approximately 50 nm film thickness, and the Mn_{Ga} concentration was estimated to be $x \approx 0.092$. For the as-grown film, magnetotransport measurements revealed a maximum resistivity of $\rho_{max} \approx 0.035 \text{ } \Omega\cdot\text{cm}$, at $T_C \approx 55 \text{ K}$. For the annealed film, $\rho_{max} \approx 0.005 \text{ } \Omega\cdot\text{cm}$ at $T_C \approx 125 \text{ K}$. The increased T_C shows that annealing certainly improved the ferromagnetic exchange. Additionally, the drop in resistivity is consistent with an increased carrier concentration [49]. From Chapter 1, remember that experiments have suggested that annealing improves the ferromagnetic properties of $\text{Ga}_{1-x}\text{Mn}_x\text{As}$ by liberating interstitial Mn impurities (Mn_{I}). Since Mn_{I} is a donor, and the substitutional Mn (Mn_{Ga}) are acceptors that mediate the ferromagnetic exchange via holes, an increased carrier concentration coupled with an increased T_C is consistent with a reduction in Mn_{I} .

Using NG-1 at the NCNR, a set of PNR measurements was taken on each of the films after cooling them to low temperature ($T = 16 \text{ K}$ for the as-grown, $T = 18 \text{ K}$ for the

annealed) while in an in-plane field of $H = 6.6$ kOe. The films were oriented with a [100] axis oriented nominally parallel to the applied field. The background for these two samples matched each other within error, and also matched that taken for several other samples under similar conditions. This justified adding these matching background scans together, in order to improve the overall uncertainty of the data. Both non spin-flip (NSF) and spin-flip (SF) data were taken. However, the SF data was found to be minimal (more on this later), and were not measured with the same statistics as the NSF. While the SF data were used to make polarization corrections to the NSF data, the uncertainty added by “cheating” on the SF was extraordinarily small compared to the reduction in uncertainty produced by spending more time counting NSF data. These scans were taken late in the study (when our methods were most optimized), and produced very high quality data.

Figure 3.3 compares the individual non spin-flip (NSF) reflectivities and fits corresponding to the as-grown (blue) and annealed (red) films. The spin-down (R_{-}) reflectivities are shown at the top, and the spin-up (R_{+}) are shown at the bottom. The data and fits are multiplied by Q^4 , and are shown on a log scale (to better emphasize subtle features). The fits shown are very good. However, before considering the results from the fitting, it is valuable to make some *qualitative* assessments based on visual inspection of the data. For both the spin-up and spin-down reflectivities, it can be seen that the low- Q intensity roughly matches for the two films, but at higher- Q the annealed film has greater intensity. Since high- Q corresponds to small length scales, this difference suggests a spatially small region of differing SLD between the films. The spin-down oscillations are pronounced for both the as-grown and annealed films, but the

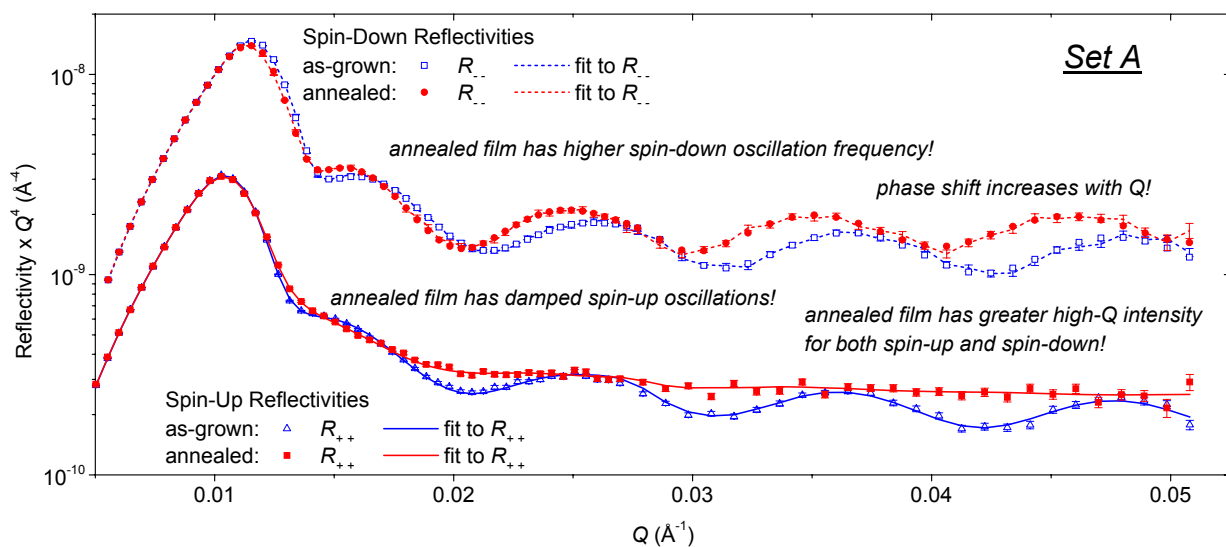


Figure 3.3: Comparison of the as-grown (blue) and annealed (red) set A 50 nm films for each of the NSF reflectivities and fits.

frequency of the oscillations is increased for the annealed film - implying that the measured thickness of the annealed film is slightly greater. Furthermore, the difference in frequency between the two films increases with increasing Q - implying a region of differing interfacial roughness between the two films. Examination of the spin-up reflectivities shows that the as-grown oscillations are far more pronounced than those of the annealed film. This suggests that for spin-up neutrons, the SLD of the $\text{Ga}_{1-x}\text{Mn}_x\text{As}$ region in the annealed film has barely any SLD contrast with its GaAs substrate, while there is significant contrast for the as-grown film. For spin-down neutrons, both films show pronounced oscillations (implying strong contrast). This spin-dependence in contrast immediately suggests *magnetic* differences between the two films.

More qualitative assessments can be made by plotting the as-grown and annealed NSF data separately, as shown in Figure 3.4. Comparing the spin-up and spin-down data in this way can provide insight into magnetic properties. While the data from the two films are similar, there are some important differences. While somewhat difficult to see while plotted this way, the “splitting” between spin-up and spin-down (R_{++} and R_{-}) is larger for the annealed film. Another difference in the spin-up/spin-down relationship is evident at low- Q . For the as-grown film, the spin-up and spin-down reflectivities form a “ribbon” between regions of maximum splitting. This feature is very different for the annealed film, for which the spin-up and spin-down reflectivities intersect between regions of maximum splitting. Additionally, at higher- Q the annealed film’s spin-up and spin-down reflectivities prominently cross back and forth. This differs from the as-grown film, for which the spin-up reflectivity is almost always greater than the spin-down.

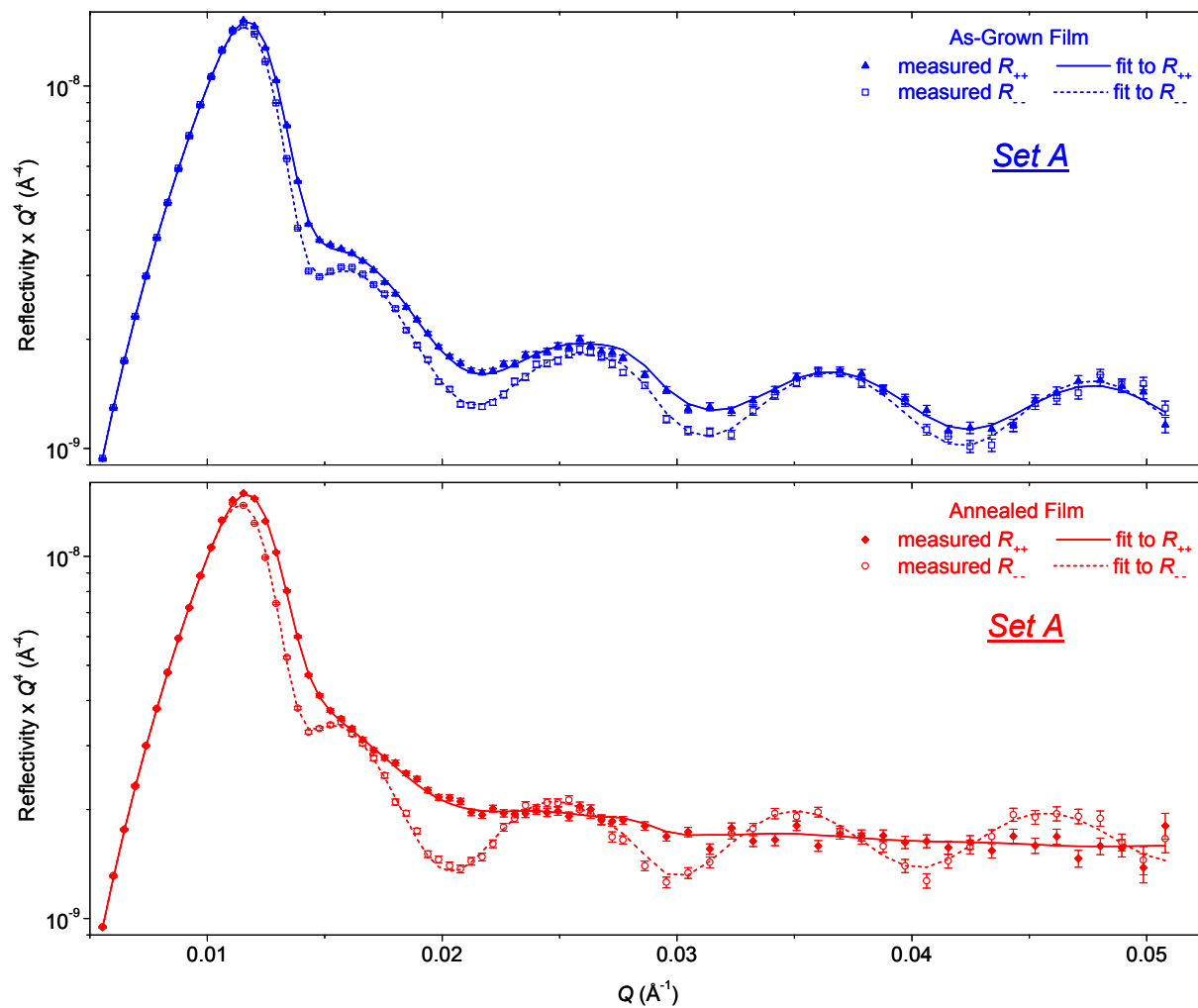


Figure 3.4: Comparison of the non spin-flip reflectivities and fits for the set A 50 nm samples. Note that for the as-grown film, the reflectivities form a “ribbon” at around 0.015 Å⁻¹, while no such feature is evident for the annealed film.

Since the splitting is small, the above listed magnetic features become more evident by recasting the NSF reflectivities and fits in terms of spin asymmetry (SA),

$$SA = (R_{++} - R_{--}) / (R_{++} + R_{--}). \quad (36)$$

Spin asymmetry [50] is a convenient quantity for gauging the film magnetization parallel to the applied field at different length scales. Focusing on the small magnetic features in this way is also helpful for ascertaining subtle differences in the quality of the fits.

Figure 3.5 shows the spin asymmetry and fits for both films.

The difference in spin-up and spin-down reflectivities manifests itself as the amplitude of the spin asymmetry. These amplitudes are clearly larger for the annealed film. Since the splitting of the spin-up and spin-down reflectivities is the result of film magnetization, the increased amplitude of the annealed film's spin asymmetry implies an increased net magnetization.

The presence (or lack thereof) of a “ribbon” formed by the spin-up and spin-down reflectivities manifests as the Q -definition of the spin asymmetry peaks. Especially at low- Q , it can be seen that the as-grown film's peaks are “smeared” together, while the annealed film's peaks are much sharper. Smearing of this sort can be a sign of magnetic roughness. A “hand waving” explanation of why this is so can be arrived at by considering the inverse relationship between reciprocal space and real space. The spin asymmetry can be thought of as the magnetic signal in reciprocal space. A sharply oscillating magnetic signal in reciprocal space implies a *continuous* distribution of

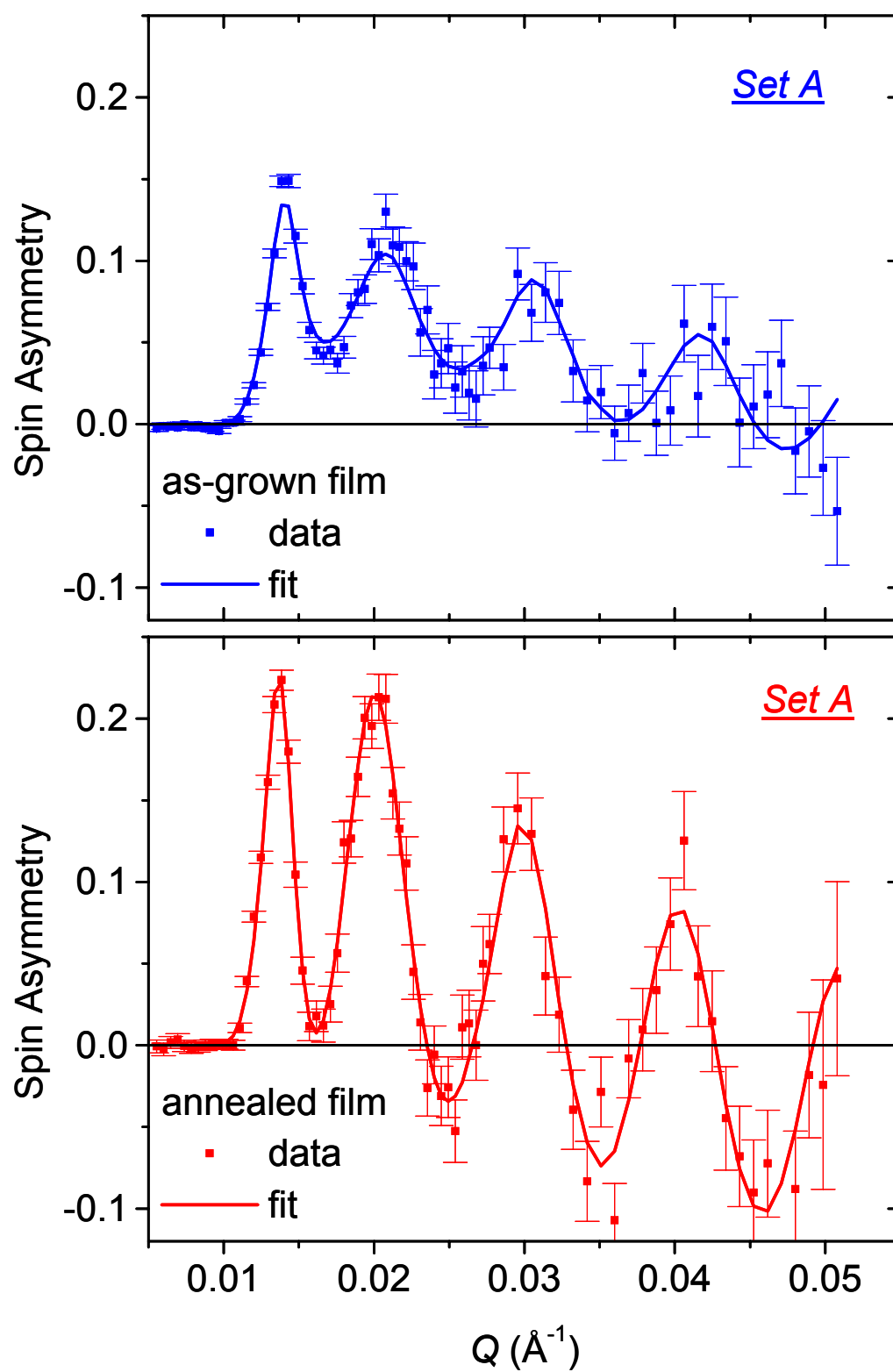


Figure 3.5: Fitted spin asymmetry for the set A as-grown and annealed 50 nm films. Annealing results in larger amplitude, less “smearing”, and more negativity at high- Q .

magnetization in real space. Conversely, smeared oscillations of the magnetic signal in reciprocal space imply a *varying* distribution of magnetization in real space.

The alternating action of the spin-up and spin-down reflectivities at high- Q in the annealed film is manifested as a spin asymmetry that crosses zero. While the spin asymmetry for the annealed film crosses zero early and often, that of the as-grown film only shows minimal signs of doing so at the highest Q . This zero crossing is a very striking feature, as it shows that at higher- Q values, neutrons polarized *antiparallel* to the film magnetization are sometimes reflected with greater intensity than their spin-parallel counterparts! This implies a length scale in the film at which there is a drastic change in the film magnetization. It can also be seen for both films that the spin asymmetry amplitude decreases at high- Q . This suggests that a small region of each film has a reduced magnetization.

To gain a more precise understanding of the differences in the films, we must consider the SLD models that produced the fits to the data, which are shown in Figure 3.6. The chemical SLD is shown as a dashed line at the top of each panel, while the magnetic SLD is the solid line at the bottom of each panel. The film magnetization is directly proportional to the magnetic SLD, and is shown on a separate scale on the right. Note the breaks in the scales, and that the magnetic SLD's correspond to different scales for the two films. Since Mn is the only atom in this system with a negative nuclear scattering length, and is the only atom contributing a *significant* magnetic moment, the $\text{Ga}_{1-x}\text{Mn}_x\text{As}$ film is clearly delineated from the GaAs substrate in each model, and corresponds to a region of decreased chemical SLD, and non-zero magnetic SLD. “Significant” is used in the preceding sentence because x-ray circular dichroism has

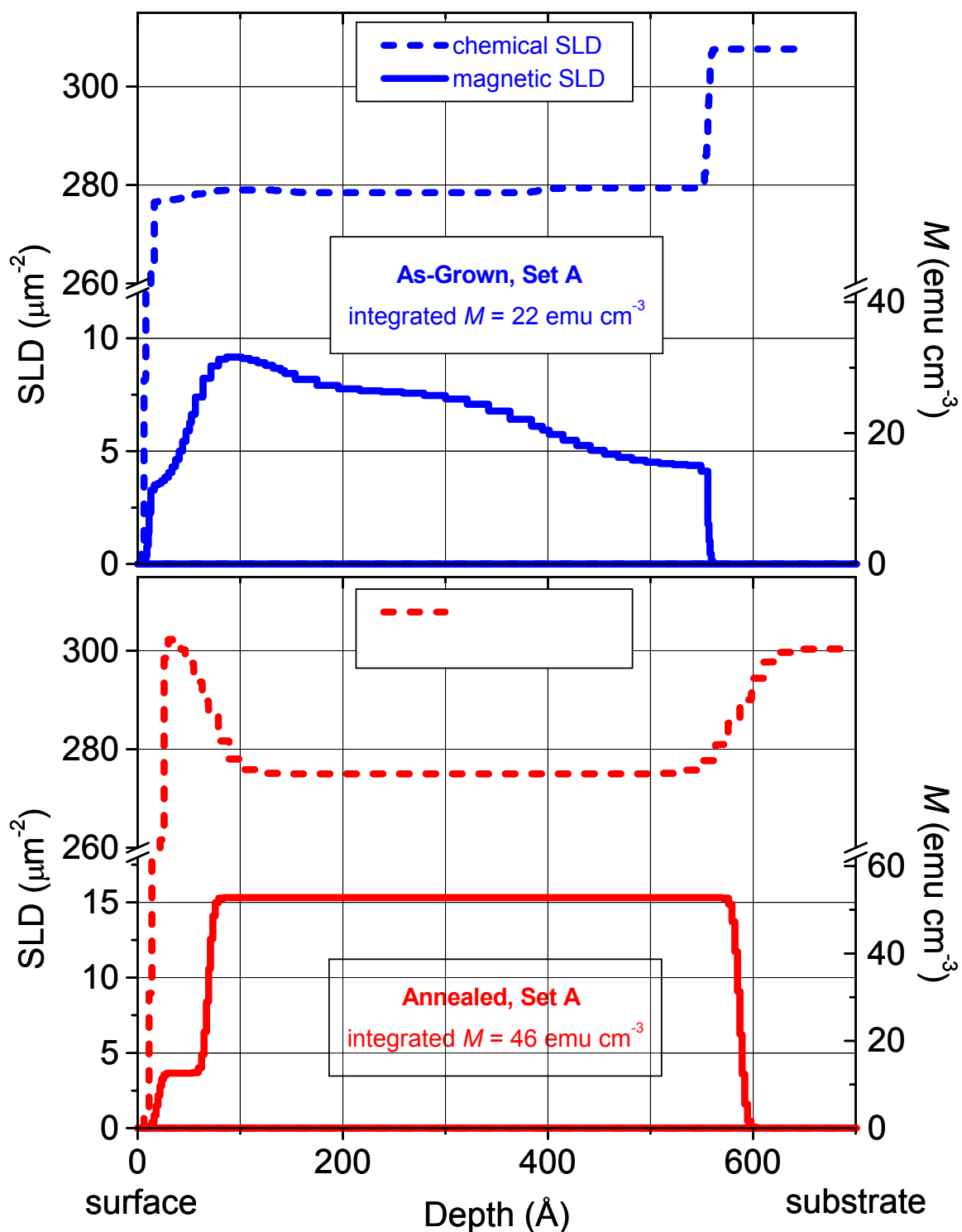


Figure 3.6: Scattering length density models used to fit the PNR data in Figs. 3.3 - 3.6. The annealed film has a larger integrated M , a more homogeneous M profile, and features a chemically altered surface layer.

revealed the presence of induced magnetic moments on Ga and As atoms in $\text{Ga}_{1-x}\text{Mn}_x\text{As}$ [51]. However, these induced moments are thought to be very small compared to the Mn moment [52, 53] and are unlikely to be responsible for the type of effects we describe here.

The model for the as-grown sample shows a substrate interface with very discrete transitions in chemical SLD and magnetization. Throughout the bulk of the film, there is little change in the chemical SLD, while the magnetization features a pronounced spatial gradient in the magnetization. Since the magnetization doubles from one side to the other while the chemical SLD does not show a comparable change, it implies that the magnetization gradient is not due to changes in total Mn concentration. Instead, a more likely explanation is that it is the *ratio* of Mn_{Ga} to Mn_{I} that is changing from substrate to surface, while the *overall* Mn concentration remains relatively constant. After the magnetization peaks near the film surface, the model shows a reduction in magnetization but no significant change in the chemical SLD at the film surface. Measurements of the net magnetization (as taken using SQUID magnetometry) can be compared to a SLD model by considering the model's *integrated* magnetization. This quantity is obtained by integrating over the magnetization of the entire film, and dividing by the film thickness. For the samples in this chapter, the *entire* film thickness (i.e. anything that's not substrate) is used in the division. The integrated magnetization for the model of the as-grown sample in Fig. 3.6 is $22 \text{ emu}\cdot\text{cm}^{-3}$.

The model for the annealed film features some drastic differences. First, it is evident that annealing produced a large increase in the magnetization, as the model's integrated magnetization is $48 \text{ emu}\cdot\text{cm}^{-3}$. At the substrate interface, we see that the

chemical roughness is significantly larger for the annealed film. This suggests some “shuffling” of Mn atoms at this interface during the annealing process. Then for the majority of the film, not only is the chemical SLD constant, but so is the magnetization. This suggests that for the annealed film, the overall Mn concentration is again constant, but that the ratio of Mn_{Ga} to Mn_I is much more uniform than it is for the as-grown. These annealing-dependent changes are highly consistent with the displacement of Mn_I . However, if this is the case, one might expect to observe a small increase in the chemical SLD of the annealed film near the substrate, corresponding to the fact that more Mn_I would have evacuated the region of depleted magnetization than any other. The absence of this increase in chemical SLD can be explained, as Mn_I are thought to be only a small fraction of the total Mn [26]. Therefore, the resulting inhomogeneity in chemical SLD is probably be too small to be detected with PNR.

More evidence for redistribution of Mn_I during annealing can be found by considering the surface of the annealed film. Here, the model shows a sharp increase in the chemical SLD, while the magnetization drastically drops to practically zero. The result is that the surface layer looks very similar to the substrate. So, the conclusion one might come to is that there is no Mn present at the surface - that it is simply GaAs. However, other experimental work has indicated that annealing enhances the ferromagnetic properties of $Ga_{1-x}Mn_xAs$ by sending Mn_I to the surface [15, 33], which would be in complete opposition to a *depletion* of Mn! This requires consideration of a different interpretation. Instead of GaAs, the surface layer could be some other compound that *looks like* GaAs. As it turns out, θ - phase MnN could fit the bill [54], as it is antiferromagnetic, and (depending on the relative ratio of Mn to N) is likely to have a

chemical SLD very similar to that of GaAs. During annealing in N_2 , it is conceivable that N oxidized Mn_I that was diffusing to the surface, forming a MnN surface layer.

However, it would be somewhat surprising that the very strong N_2 bond would be broken at our low annealing temperatures (although it might happen due to some sort of surface effect). Oxygen would be a more plausible oxidizing agent for the Mn_I , but the measured chemical SLD is much higher than that expected for common Mn & O compounds. This leaves MnN formation as the most likely explanation for the surface layer we observe, although this cannot be proven with PNR alone. Additionally, the model shows that the surface layer is approximately 5 nm thick, which is approximately equal to the observed difference in overall film thickness between the as-grown and annealed models. This further supports the idea of annealing producing a new surface layer [55].

3.6 χ by Eye

The models for the as-grown and annealed films in Fig. 3.6 each use a different number of layers. The as-grown film required five layers for a best fit (substrate and four $Ga_{1-x}Mn_xAs$ layers of changing magnetization), while the annealed required only 3 layers (substrate, $Ga_{1-x}Mn_xAs$, and MnN). The justification for incorporating additional layers in the model for the as-grown film is that the least-squares fit to the PNR data improves significantly when the parameters in the additional layers are allowed to vary. Additional layers do not substantially improve the fit for the annealed film.

While the change in χ^2 (the measure of fit accuracy in a least-squares fit) is solid justification for adding layers to allow for a graded magnetization in the as-grown film, it is good practice to also use “ χ by eye” - that is, visually inspect the quality of the fits [56]. Figure 3.7 compares a flat magnetization 3-layer model and corresponding fit (shown in light blue) to the graded magnetization 5-layer model and fit from Figure 3.5 and Figure 3.6 (shown in dark blue). The “flat” model (which does allow for reduced magnetization near the surface) fails miserably in describing the low- Q spin asymmetry. The flat model neither accounts for the broadness of the peaks, nor comes close to reproducing the smearing of the peaks.

The situation is very different for the annealed film. Consider Figure 3.8, where the 3-layer model from Figure 3.6 and corresponding fit from Figure 3.5 (shown in red), is compared to a 5-layer model and its corresponding fit (shown in pink). While a very small decrease in χ^2 is obtained by allowing the additional layers parameters to vary, the fits produced from the two models is essentially the same! Even though the extra layers are not otherwise useful, they do establish some uncertainty for the fit to the annealed film. Small changes in the magnetization are not required to fit the data for the annealed film, but they cannot be ruled out, either! However, these small changes are certainly not comparable to the large ones featured in the model for the as-grown film, in which the magnetization approximately doubles from one side to the other.

Uncertainty in the model for the as-grown film is a little tougher to establish. While the difference in fitting quality from the two models shown in Figure 3.7 is striking, the difference in fitting quality between competing models that both feature a

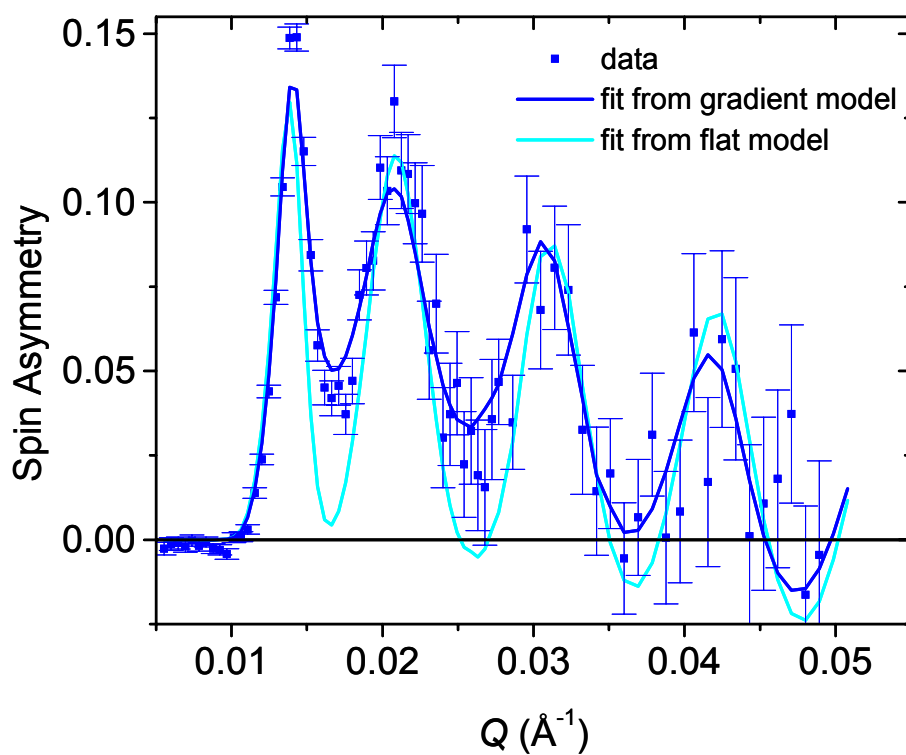
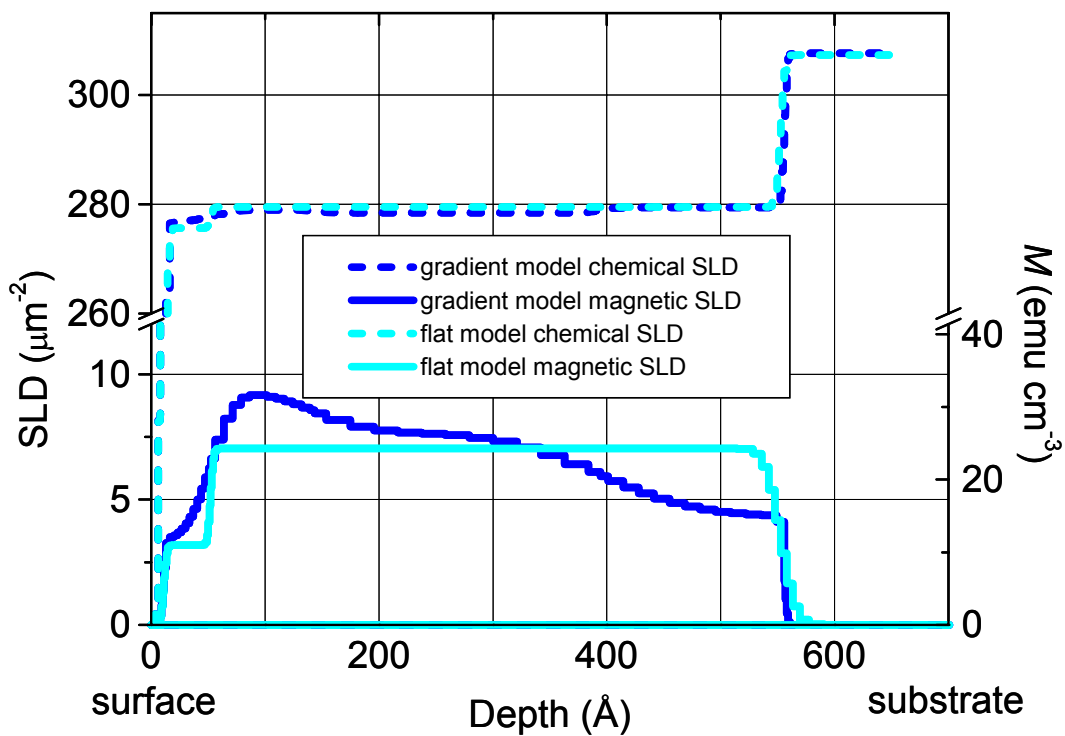


Figure 3.7: Comparison of the 5-layer “gradient” model and fit for the as-grown film (from Fig. 3.5 and Fig. 3.6) to an alternate 3-layer “flat” model and fit. The flat model is not adequate to describe the data.

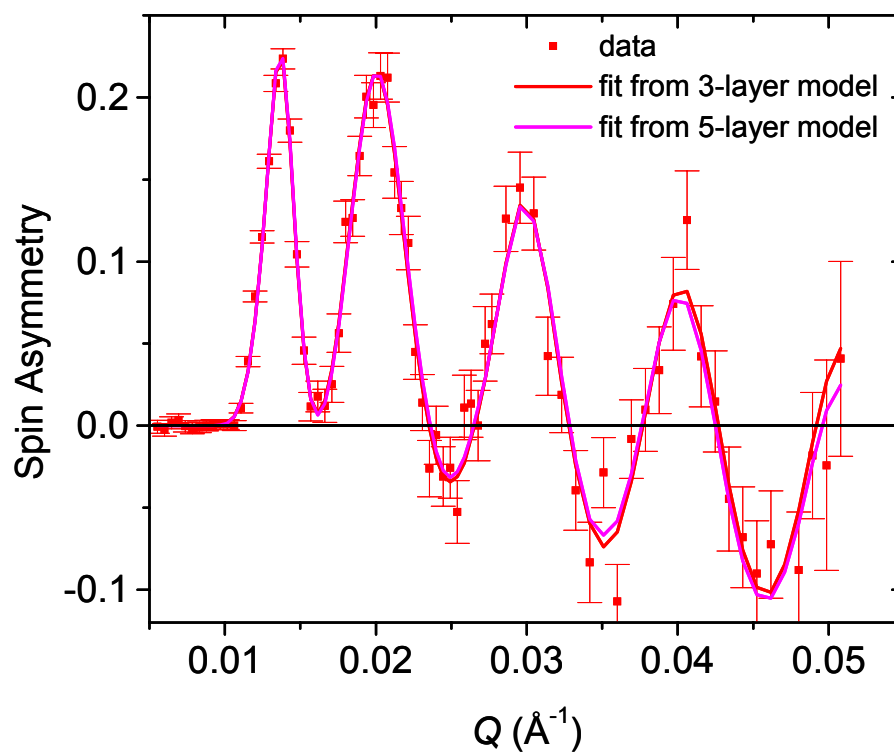
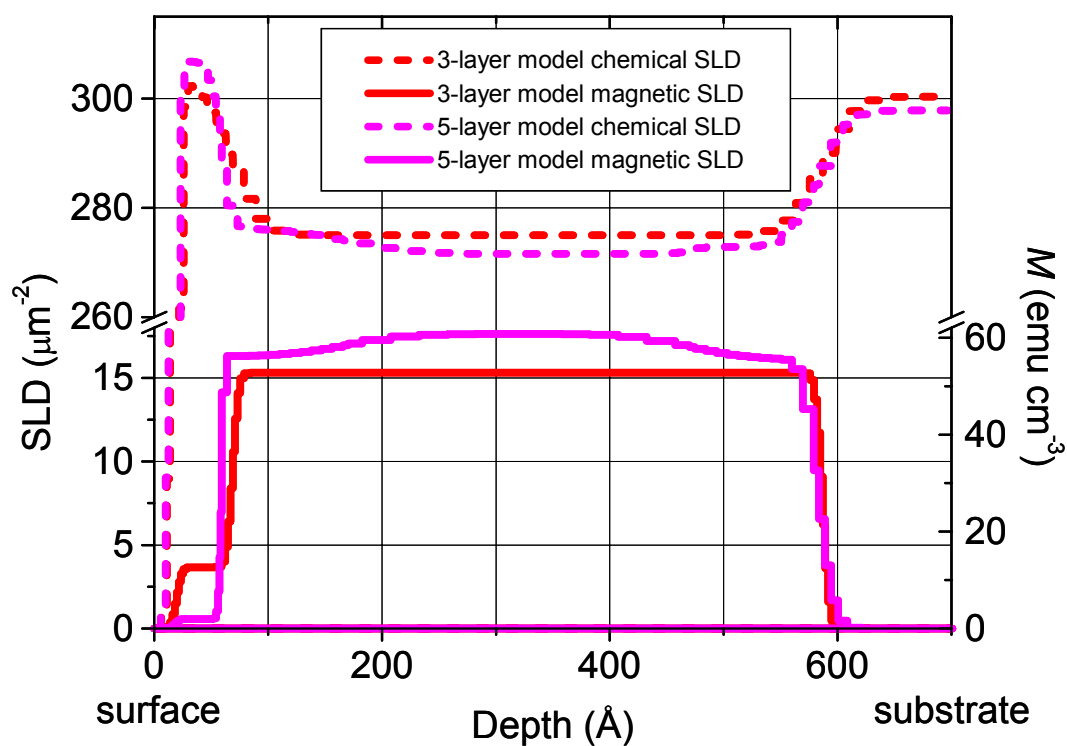


Figure 3.8: Comparison of the 3-layer model and fit for the annealed film (from Fig. 3.5 and Fig. 3.6) to an alternate 5-layer model and fit. The models produce essentially the same fit to the data

magnetization gradient is more subtle. However, the model for the as-grown film in Figure 3.6 provides the best fit of any tried so far [57], and each of the main features in its magnetization profile (low magnetization at the substrate, gradient with an approximate factor of two increase, peak just below the surface, reduced magnetization at the surface) appear to be necessary to arrive at this best fit.

3.7 Spin-Flip Data

As previously alluded to, the spin-flip (SF) scattering measured for all the samples in this study was too small to realistically fit. However, some SF scattering was usually detected, which could indicate that there was some in-plane moment canting present in these films. In order to give some idea of what cannot be ruled out from our measurements, we will consider the SF scattering from the above discussed scan of the set A annealed sample, which is typical of most of the samples. Figure 3.9 shows the PNR data and fits for all four reflectivities. SF data that was below background, or essentially indistinguishable from background has been removed. Figure 3.9 shows just how weak the SF scattering is, as at best it is two orders of magnitude less than the NSF scattering, and extends only over a very limited region of Q . However, this small scattering can be fit in a manner consistent with the NSF data, using the model shown in Figure 3.10. This model is very similar to the one shown in Figure 3.6, except that the magnetic moments are canted away from the applied field by an average of 19° throughout the $\text{Ga}_{1-x}\text{Mn}_x\text{As}$ film.

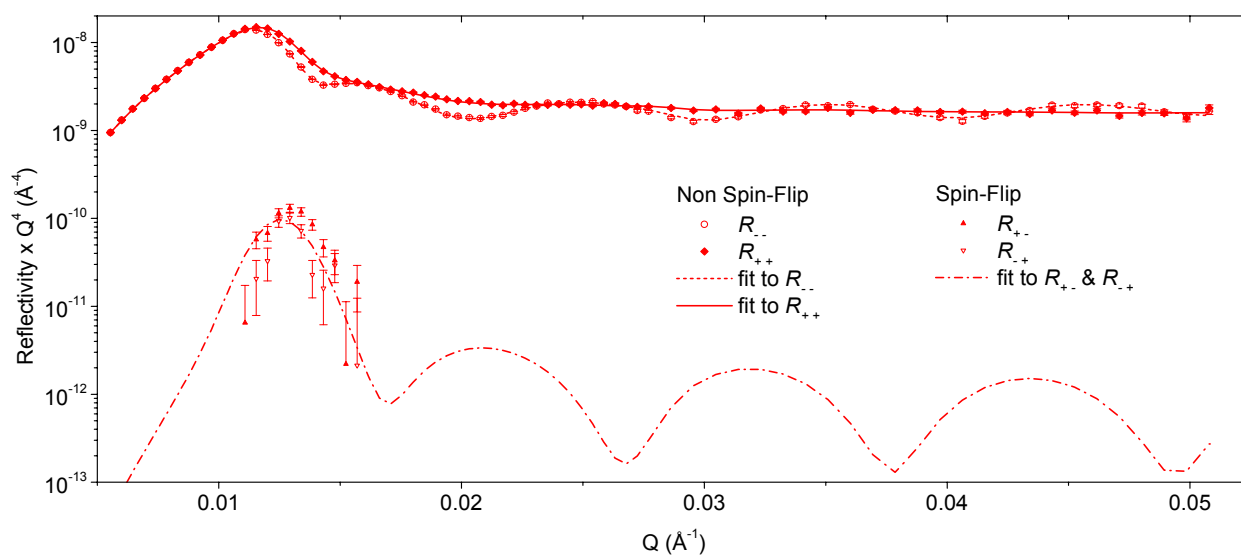


Figure 3.9: Non spin-flip (NSF) and spin-flip (SF) reflectivities and fits. The SF data is two orders of magnitude lower than the NSF data, and is appreciably different from background for only a very limited range of Q .

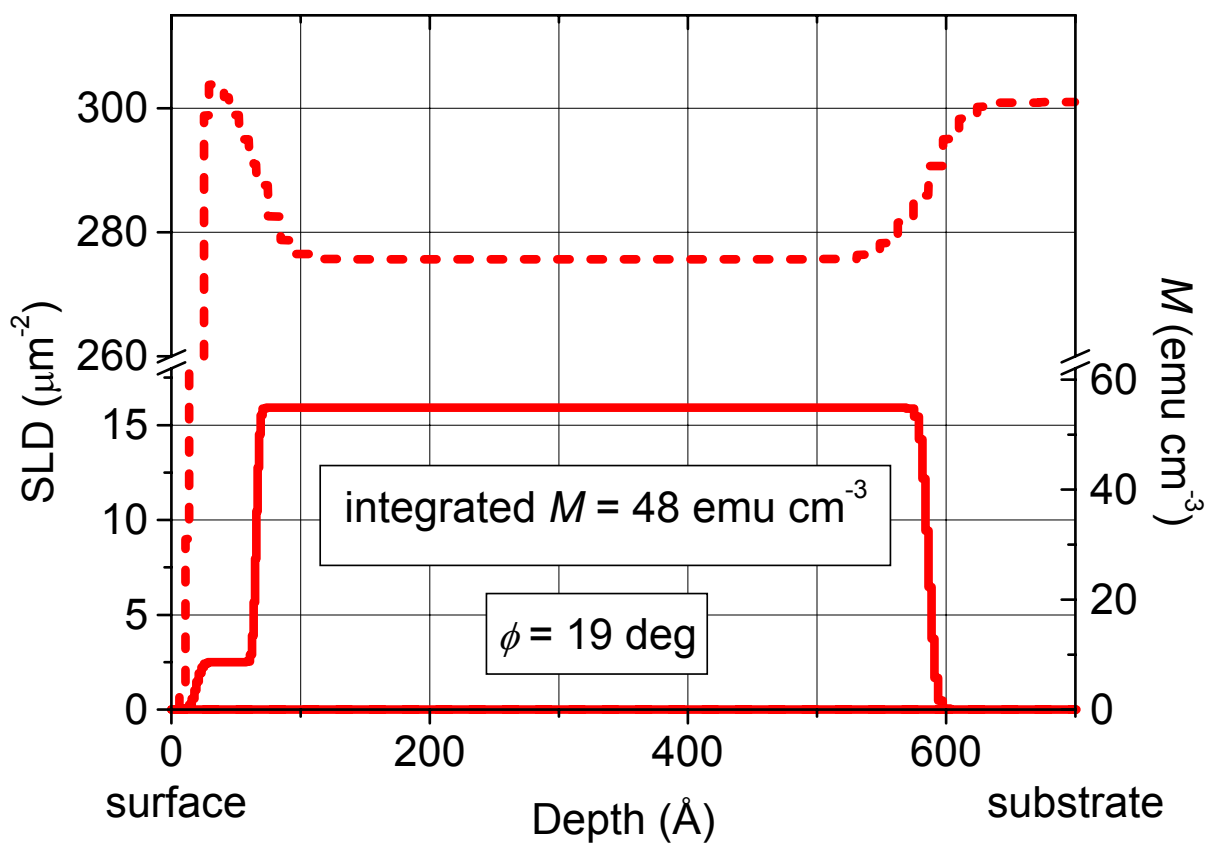


Figure 3.10: Alternate scattering length density model that accounts for non spin-flip and spin-flip data from the annealed film. For this case, “magnetization” refers to the total magnetization, not just the component parallel to the applied field.

While this model is discussed for the sake of completeness, moment canting of this magnitude seems *highly* unlikely in an applied field of 6.6 kOe. Furthermore, the SF scattering is small enough to be near the uncertainty of our ability to do polarization corrections to the data. So, while we can't rule out some moment canting, we certainly can't verify it. At any rate, we see no consistent difference in SF scattering between as-grown/annealed pairs, suggesting that moment canting is not a factor in annealing-dependent differences.

3.8 Lower-Field Scans of Set A

Besides the scans discussed above, there were an additional set of PNR scans taken on set A. These scans were taken under different conditions, as the samples were examined with a [110] direction aligned nominally parallel to an applied field of 1 kOe, after being zero field cooled to $T = 13$ K. These data were taken earlier in the study than the above described high-field data, and are of significantly lower quality. The low-field scans were taken for lower counting times, and at lower point density, which creates additional ambiguity about smearing of the data (the key to detecting magnetization gradients). The point density below the critical edge is particularly low, which causes added uncertainty in the footprint correction (see Section 2.6), and thereby added uncertainty in the high- Q intensity. It is also possible that the samples were held looser than in the high-field scans, allowing for slight in-scan sample movement that could have led to irregular chemical SLD profiles.

Figure 3.11 shows the individual low-field NSF reflectivities and fits plotted together for both as-grown and annealed films. The annealed film's reflectivities are more intense than the as-grown at high- Q , and the annealed film's spin-up reflectivity shows little contrast, agreeing well with the high-field scans. Those data and fits are recast as spin asymmetry in Figure 3.12. The spin asymmetry for the as-grown film is qualitatively similar to its high-field counterpart. However, there is a subtle difference between high and low-field for the annealed film, as the low-field spin asymmetry shows slightly more smearing at low- Q .

The SLD models used to fit the low-field data are shown in Figure 3.13. Both models show reduced homogeneity of the chemical SLD. Given the high-field results, these variations in chemical SLD likely result from the inferior quality of the data, and should not be considered as realistic. The model for the as-grown film again features no major change in surface chemical SLD, and has a pronounced magnetization gradient. But, in this case, the best fit requires a more pronounced peak in magnetization near the film surface. The model for the annealed film is again thicker and rougher at the substrate than the as-grown film, and features a sharp peak in chemical SLD corresponding with a drop in magnetization at the surface - reaffirming the presence of a chemically altered surface layer. The annealed film's magnetization is more uniform than the as-grown, but does show a region of reduced magnetization near the substrate - a feature corresponding to the increased smearing of the spin asymmetry.

It is conceivable that these differences from high to low field for both films could be real. But, it seems somewhat unlikely that particular regions of the films are magnetically turning "on and off" by the change in field conditions. It seems more likely

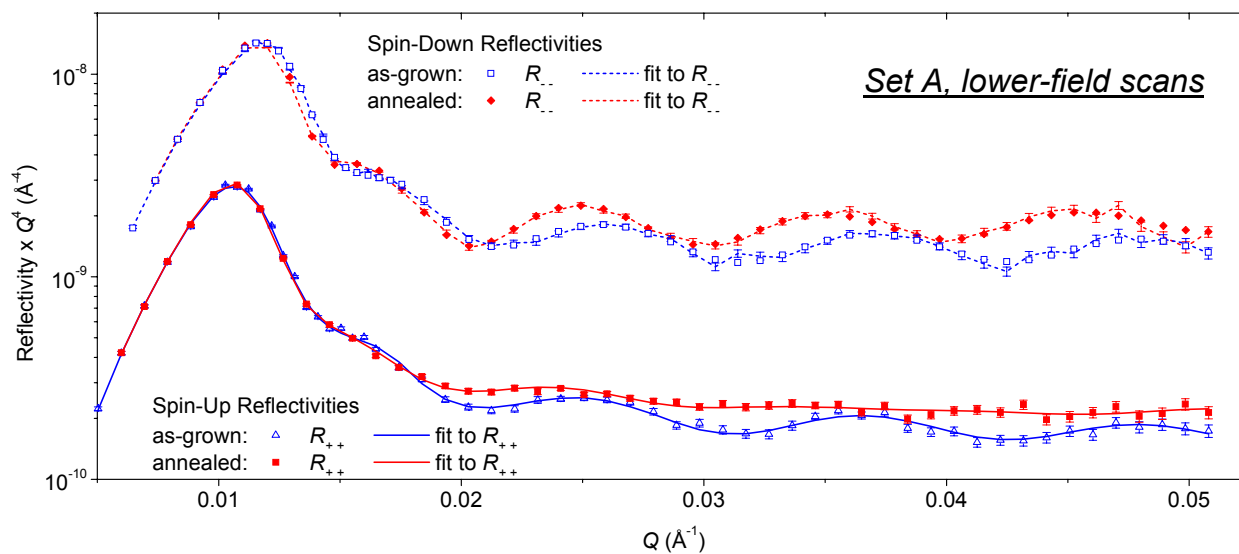


Figure 3.11: Lower-field PNR data and fits for the 50 nm films. The increased intensity for the annealed film at high- Q agrees well with the higher-field data.

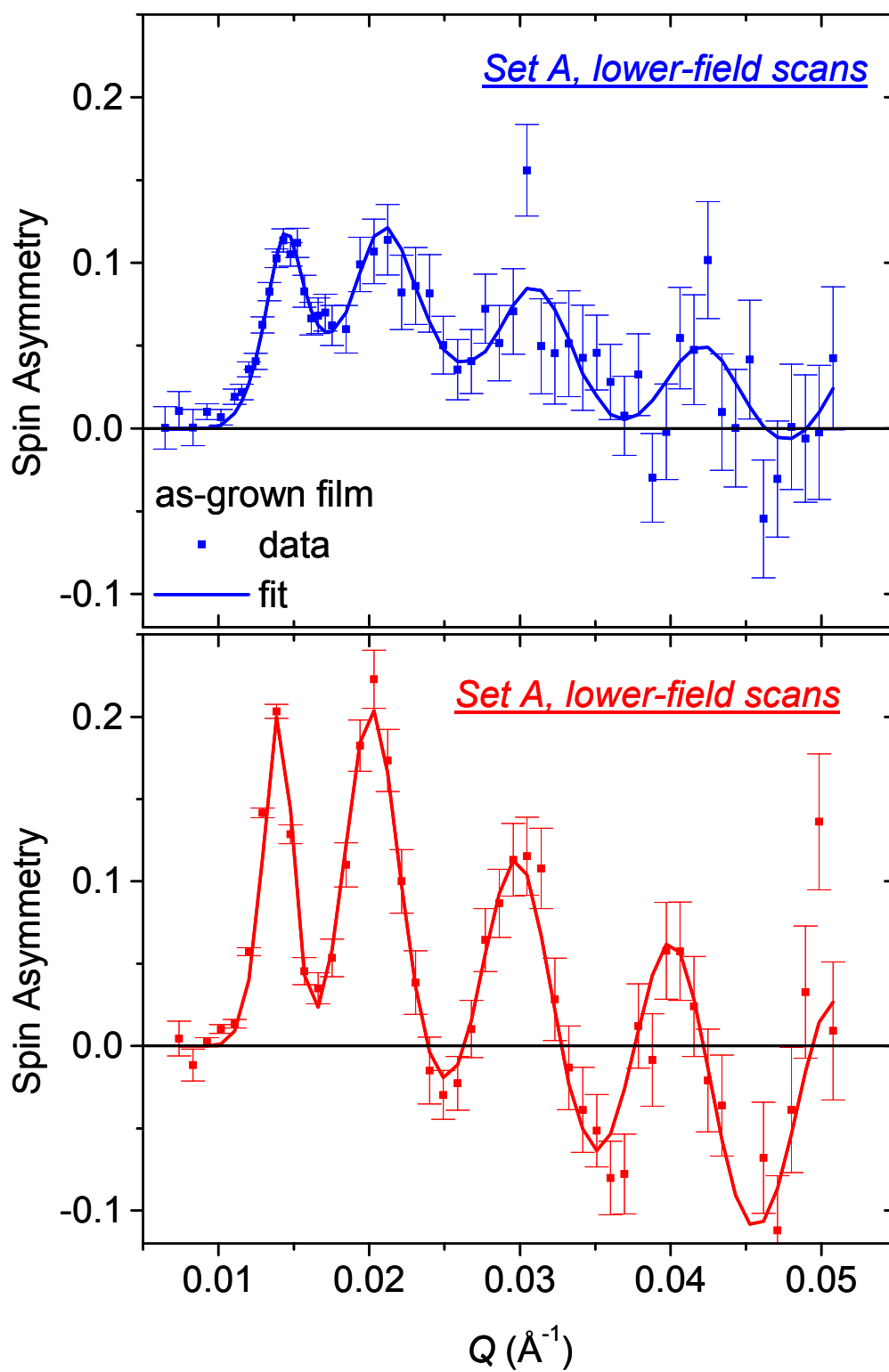


Figure 3.12: Lower-field spin asymmetries and fits for the as-grown and annealed set A 50 nm films. The features are similar to those at higher-field.

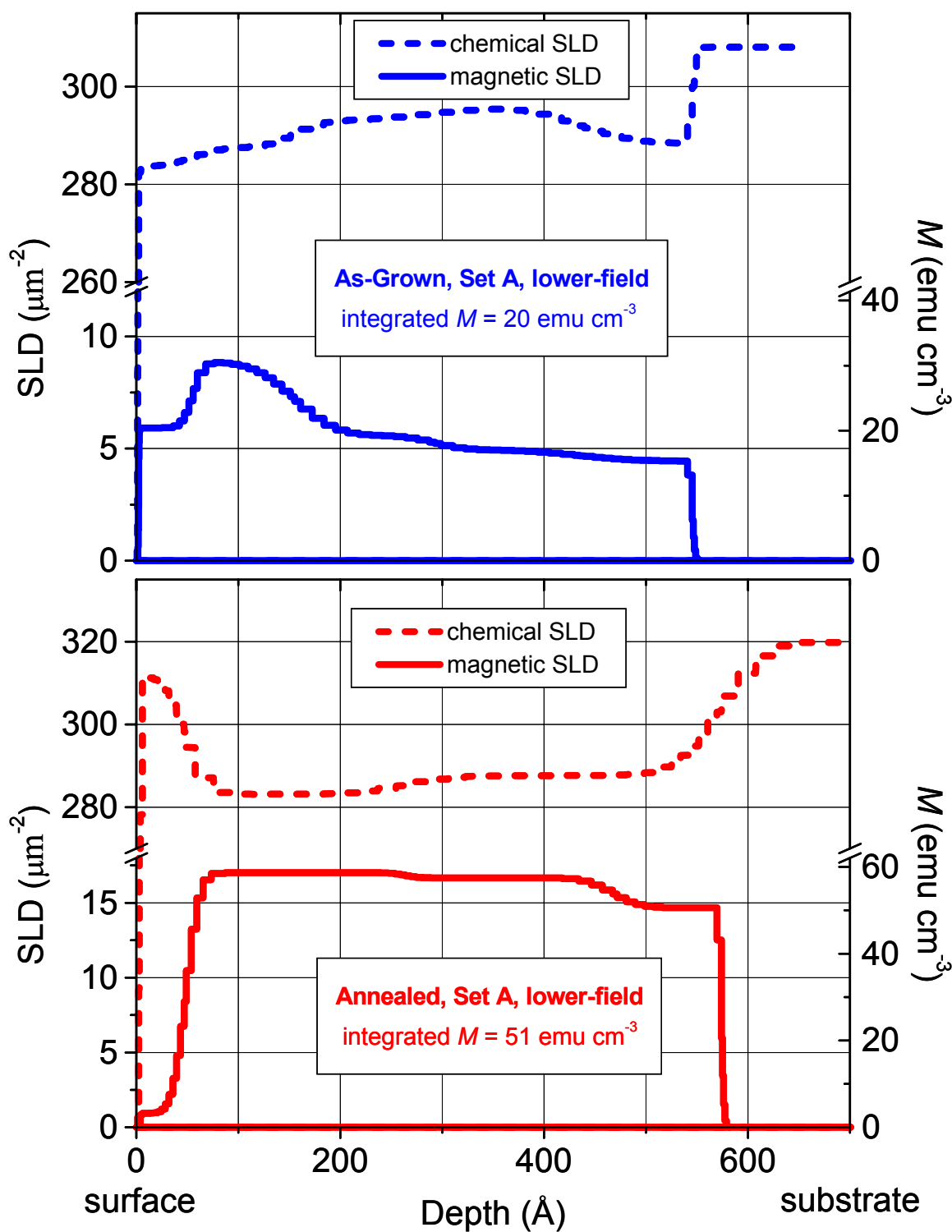


Figure 3.13: Scattering length density models used to fit the lower-field PNR data. These models agree well with the important features of the models for the higher-field data

that these differences result from the inferior quality of the data. What is important is that these data do corroborate the most important features of the high-field models: magnetization gradient in the as-grown film, increased and more homogeneous magnetization for the annealed film, and evidence for a MnN layer at the surface of the annealed film.

3.9 Set B: Annealing Dependence in a 100 nm Film

The second set of samples we'll consider is an as-grown/annealed pair of approximately 100 nm film thickness, denoted as "set B". The Mn_{Ga} concentration was $x \approx 0.076$. For the as-grown film, magnetotransport measurements revealed a maximum resistivity of $\rho_{max} \approx 0.036 \text{ } \Omega \cdot \text{cm}$ at $T_C \approx 60 \text{ K}$. For the annealed film, $\rho_{max} \approx 0.006 \text{ } \Omega \cdot \text{cm}$ at $T_C \approx 125 \text{ K}$. These resistivities and T_C 's are similar to those of the previously discussed 50 nm samples, and again suggest a decrease in Mn_{I} concentration with annealing. The field and temperature dependent net magnetizations for these films were measured using SQUID magnetometry, and are shown in Figure 3.14. Comparison of the as-grown and annealed field-dependent magnetizations at $T = 13 \text{ K}$ shows that annealing increased the high-field magnetization from $20 \text{ emu} \cdot \text{cm}^{-3}$ to $40 \text{ emu} \cdot \text{cm}^{-3}$, and decreased the coercive field. The temperature-dependent magnetizations confirm that annealing increased T_C and additionally show that annealing made the temperature distribution more "mean-field like".

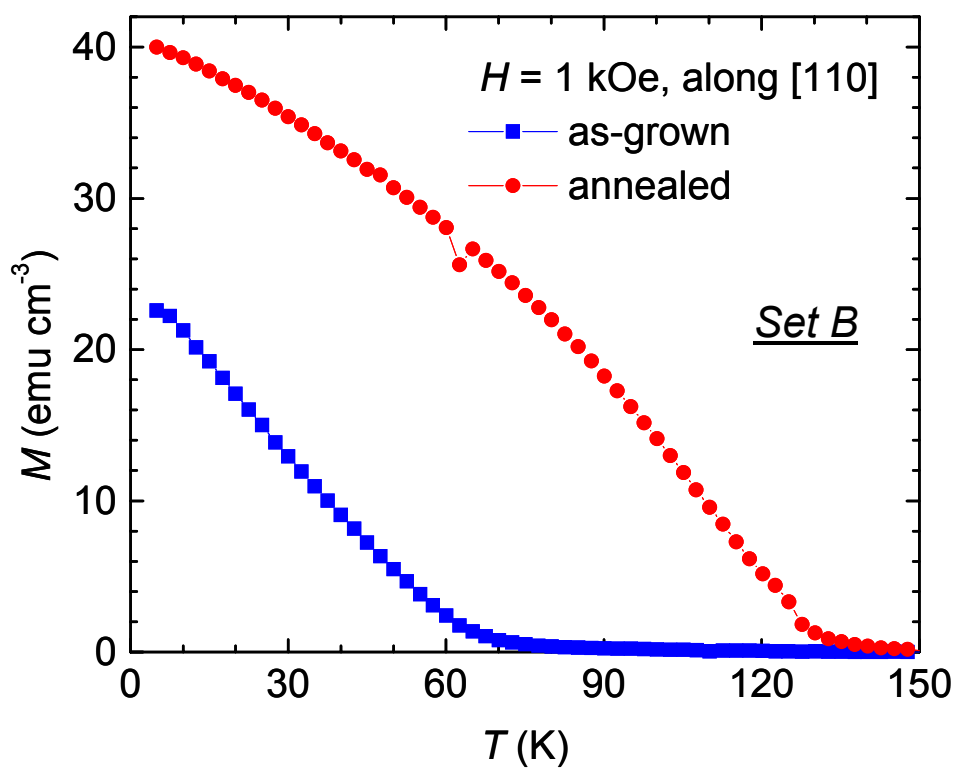
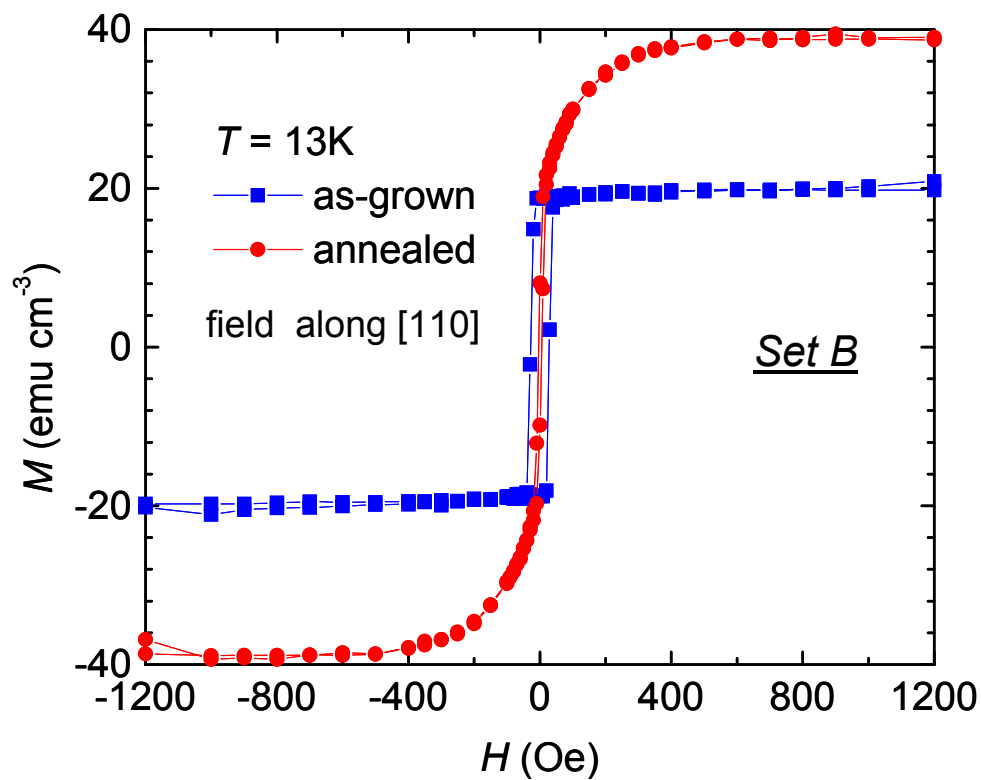


Figure 3.14: Field-dependent and temperature-dependent net magnetization dependencies for set B's as-grown and annealed samples.

PNR measurements were taken on NG-1 after zero-field cooling the samples to $T = 13$ K, and applying $H = 1$ kOe in-plane. The samples were oriented with a [110] direction nominally parallel to H . Extensive background scans were taken for each film, negating the need for addition of background from other scans. SF data was taken with equal statistics to the NSF data, and was found to be minimal. While these measurements were a “breakthrough” in terms of detecting small differences in these very dilute magnetic materials [34], they were taken relatively early in the study, and the resulting data quality (and corresponding uncertainty) pales in comparison to that of set A.

Figure 3.15 compares the individual NSF reflectivities for the as-grown and annealed films. As was the case for set A, Figure 3.15 shows increased high- Q intensity for the annealed film - suggesting a differing surface layer. Differences in oscillation frequency are more subtle than for set A, making differences in film thickness more ambiguous. However, the spin-down oscillations for the annealed film do appear to undergo a greater change in frequency than do their as-grown counterparts - implying increased substrate roughness for the annealed film. Figure 3.16 shows each film’s NSF reflectivities and fits plotted together. Since the films are 100 nm instead of 50 nm, the oscillations are more tightly spaced than for set A, making subtle features more difficult to distinguish. This difficulty is compounded for the annealed film, as the data was taken with lower point density. Despite these difficulties, it can be seen that for these thicker samples, the as-grown film again has more of a “ribbon” quality to the low- Q data, and that again the spin-up and spin-down reflectivities cross more prominently for the annealed film.

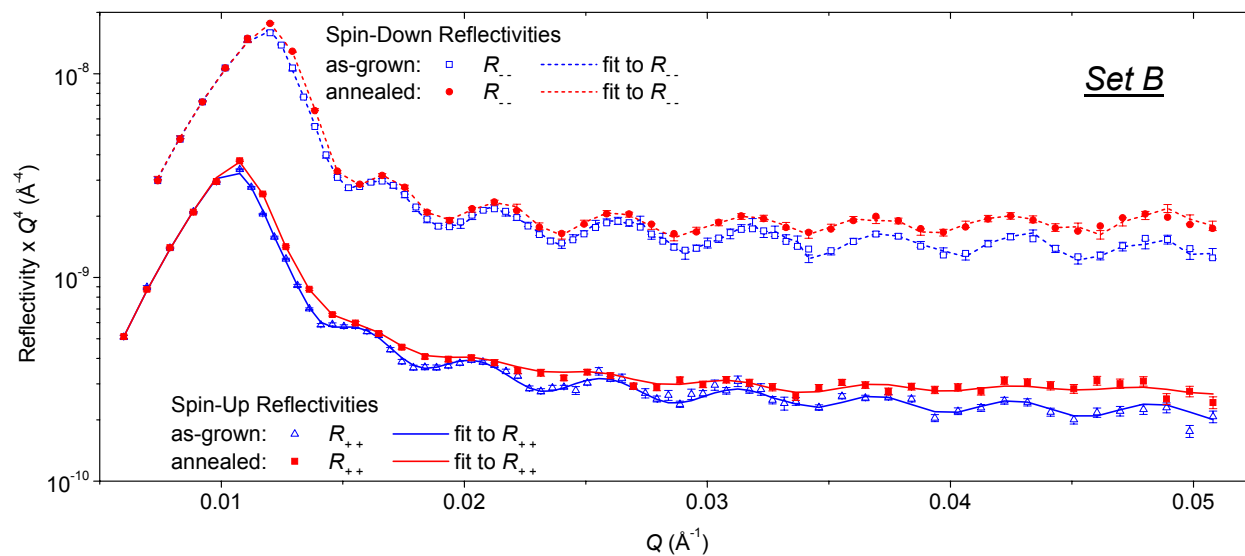


Figure 3.15: Comparison of the as-grown and annealed set B 100 nm films for each of the fitted NSF reflectivities. The annealed film is more intense than the as-grown at high- Q .

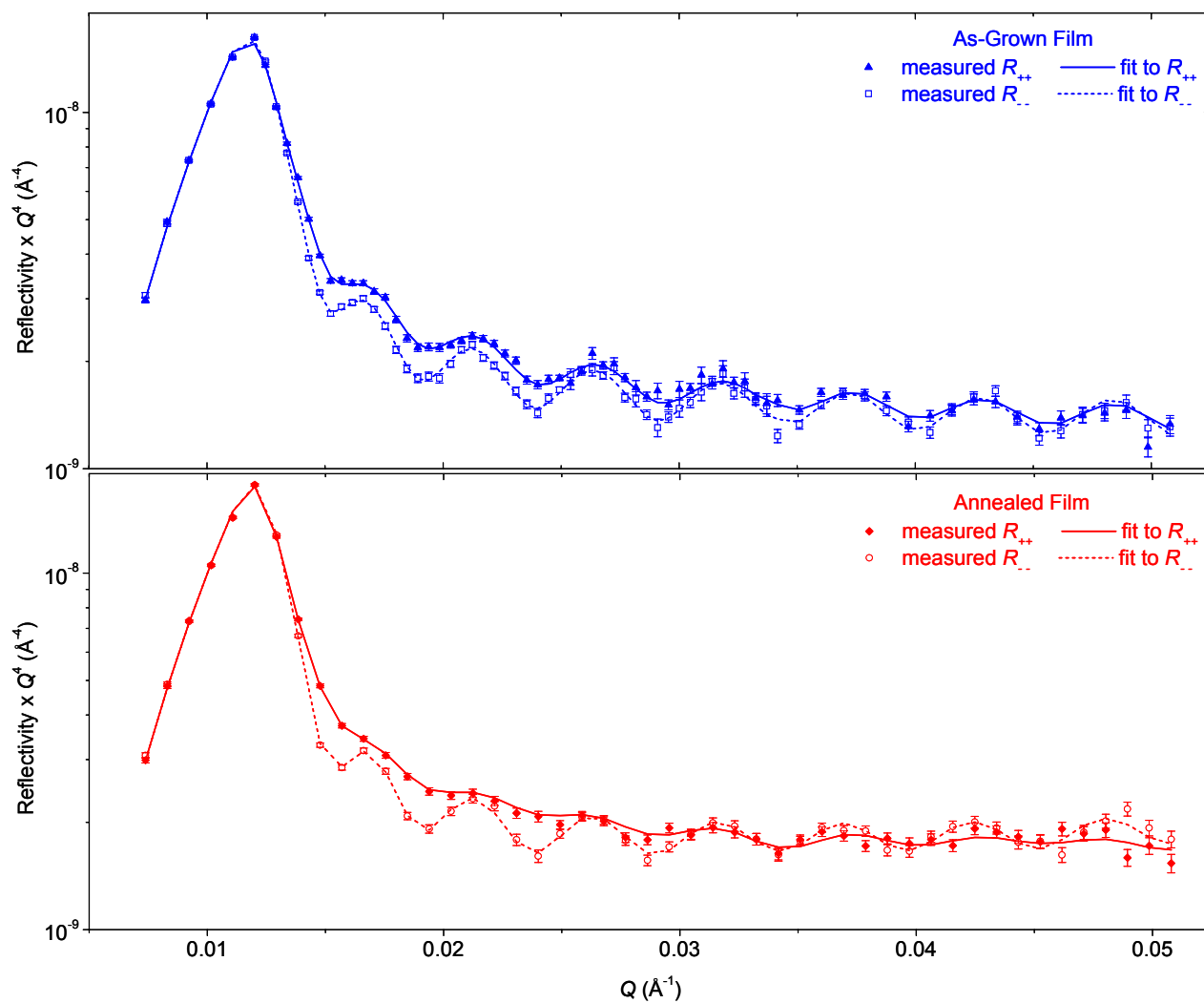


Figure 3.16: Comparison of the NSF reflectivities and fits for the as-grown and annealed set B 100 nm films.

These features are accentuated in the fitted spin asymmetries for the two films, which are shown in Figure 3.17. It can be seen that annealing increases the peak amplitude, and decreases the smearing of the peaks somewhat (especially in proportion to the *amplitude* of the peaks) - suggesting an increased and more homogeneous magnetization upon annealing. Both films show a decrease in peak amplitude at high- Q (suggesting reduced magnetization at the surface), but the annealed film spin-asymmetry prominently crosses zero (suggesting a more drastic drop in magnetization).

The best fits for this data were generated with the SLD models shown in Figure 3.18. These 6-layer models corroborate the SQUID measurements fairly well, as they show that annealing increases the integrated magnetization from $17 \text{ emu}\cdot\text{cm}^{-3}$ to $48 \text{ emu}\cdot\text{cm}^{-3}$. The models are qualitatively very similar to those for set A. Again we see a pronounced magnetization gradient for the as-grown film, and very little change in the chemical SLD at the surface. For the annealed film, the chemical roughness is increased, and the magnetization gradient is less extensive. Additionally, the top 50 \AA of the annealed film features a sharp increase in chemical SLD, and a sharp decrease in magnetization, likely corresponding to a MnN layer. These models again are consistent with an increase in film thickness upon annealing.

However, there is more uncertainty in the models of set B as compared to those of set A, due to increased thickness and reduced data quality. This uncertainty is especially prevalent for the as-grown film. While the fitting is very sensitive to the presence of a magnetization gradient, it is not very sensitive to the *spatial extent* of the gradient. To illustrate the approximate range of possible spatial extents, consider Figure 3.19, which

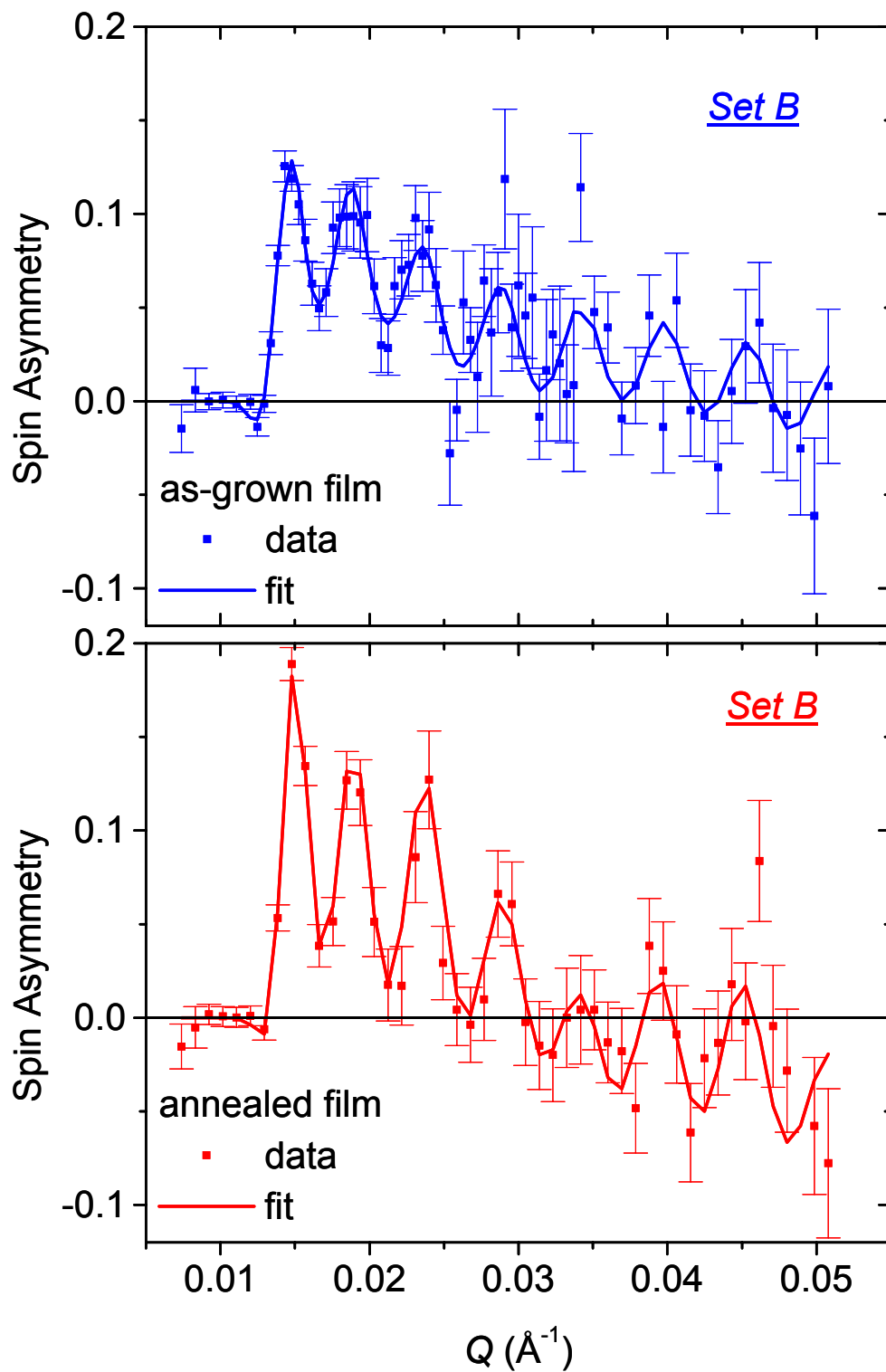


Figure 3.17: Fitted spin asymmetries for the set B 100 nm films. The annealed film features less low- Q smearing, and more high- Q negativity.

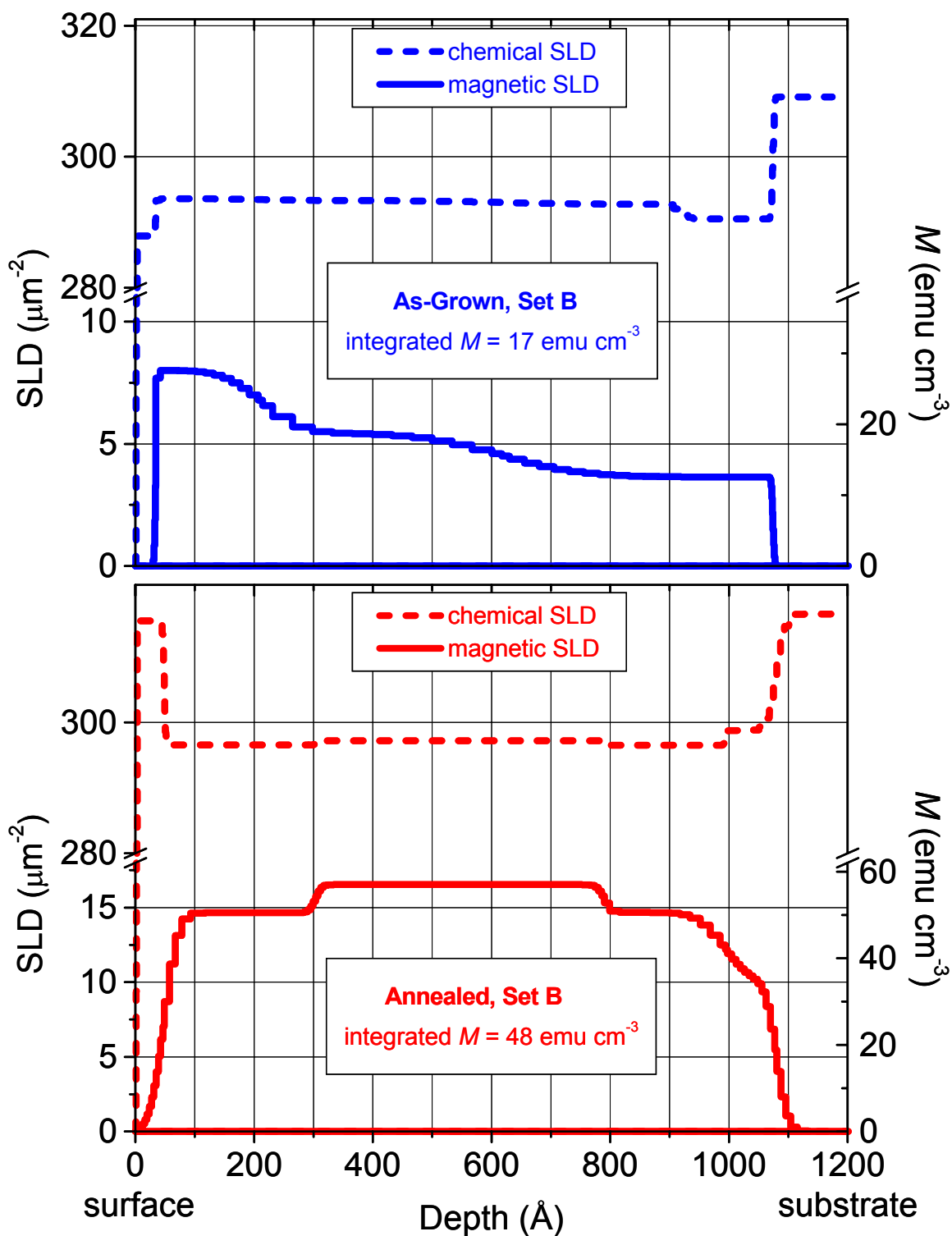


Figure 3.18: Scattering length density models used to fit the set B PNR data. The annealed film shows an increased M , a more homogeneous M , and a chemically altered surface layer.

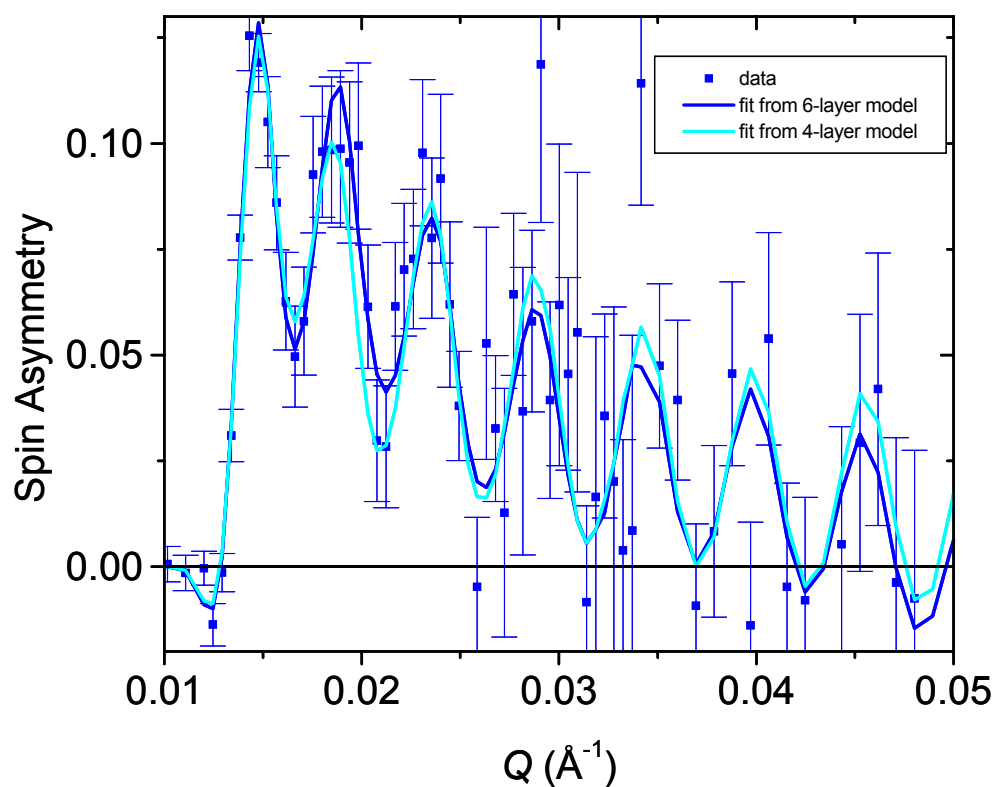
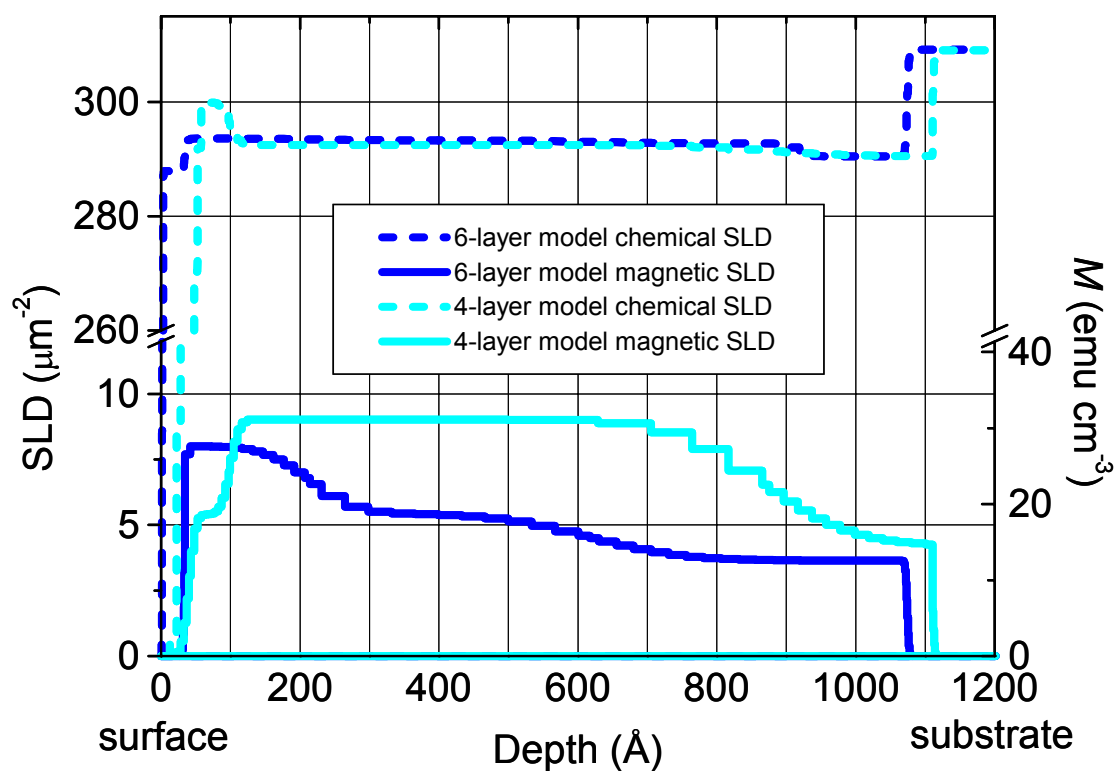


Figure 3.19: Comparison of the 6-layer model and fit for the as-grown film (from Fig. 3.17 and Fig. 3.18) to an alternate 4-layer model and fit. The 4-layer model is only slightly worse at fitting the data - suggesting it is also a reasonable model.

shows a χ -by-eye comparison of the “best-fit” 6-layer model from Figure 3.18 and a simpler “close to best-fit” 4-layer model. The two models have significant differences, as the 4-layer model has a larger integrated magnetization ($25 \text{ emu}\cdot\text{cm}^{-3}$), and a less extensive magnetization gradient. The 4-layer model also expresses the uncertainty in the composition of the surface layer, as the high- Q data is not really sufficient to tell whether the surface is smooth, and has no change in chemical SLD, or if the surface is exceptionally rough and has an extremely small spike in the chemical SLD (essentially the same thing, from our point of view). The spin asymmetry fits in Figure 3.19 show the small deficiencies of the 4-layer model, as it is slightly worse at reproducing the second peak of the spin-asymmetry. However, this difference in the fits is very subtle, so the 4-layer fit cannot be realistically ruled out. Further reducing the spatial extent of the magnetization gradient progressively worsens the quality of the fit.

A comparison of the 6-layer model for the annealed film, and a simpler 4-layer model is shown in Figure 3.20. The only noticeable difference in the two models is that the 4-layer model is “flatter”, as it does not feature the magnetization “shelf” that is present at the center of the 6-layer model (at $46 \text{ emu}\cdot\text{cm}^{-3}$, the integrated magnetization for the 4-layer model is only slightly smaller than that of the 6-layer model). The resulting difference in the fits largely amounts to the 4-layer model not accounting for the amplitude of the third spin asymmetry peak. Since this difference essentially concerns one data point, the existence of the magnetization shelf does not stand on particularly solid ground.

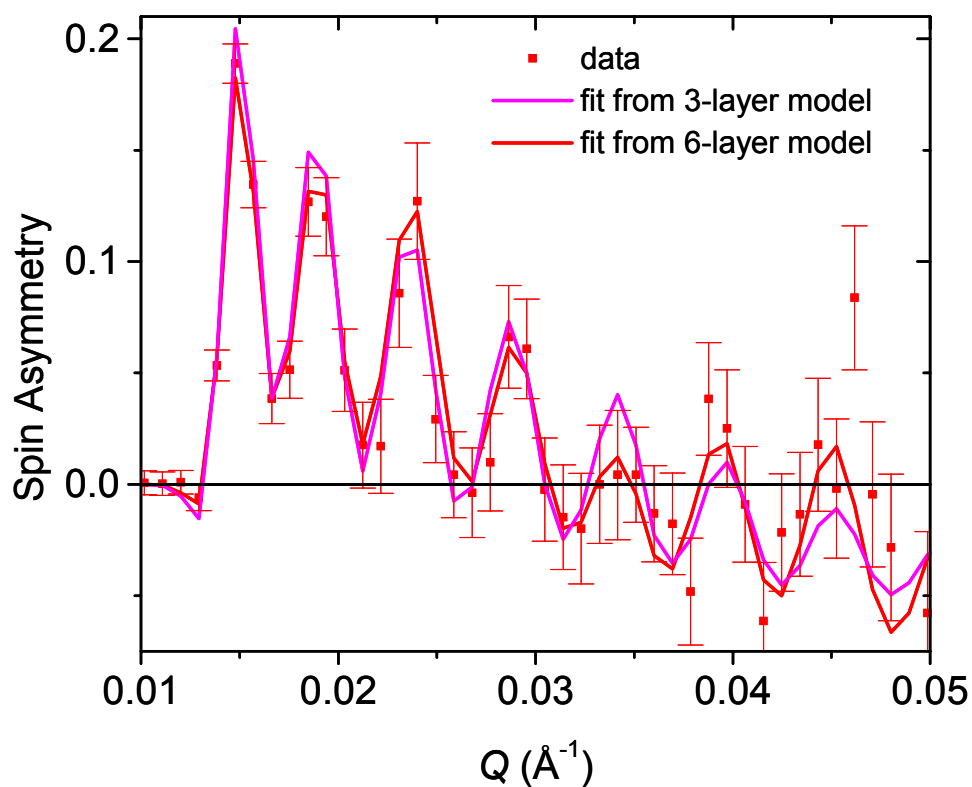
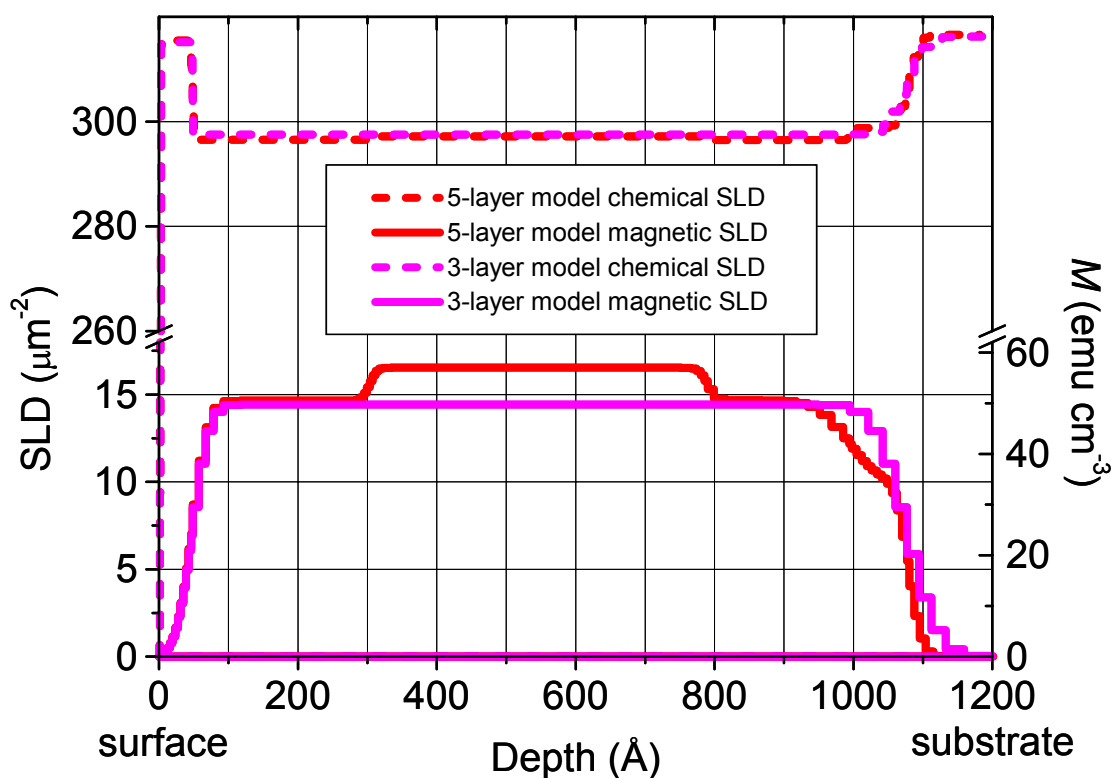


Figure 3.20: Comparison of the 6-layer model and fit for the annealed film (from Fig. 3.17 and Fig. 3.18) to an alternate 3-layer model and fit. The 3-layer model is only slightly worse at fitting the data - suggesting it is also a reasonable model.

Due to the low point density, we have found that the data for the annealed sample are somewhat ambiguous, and can support alternate models in which there are more variations in the magnetization. Although these alternate models can suitably fit the data, they do not *improve* the fit, and can generally be discounted as unphysical, for reasons such as integrated magnetizations that do not agree well with SQUID measurements, and/or large scale inhomogeneity in the chemical SLD. While these alternate models cannot be *completely* ruled out, at the very least it can be said that the data for the as-grown sample appear to *require* a significant magnetization gradient, while the data for the annealed sample certainly do not.

So, even though differences in the magnetization depth profile for set B are not quite as “concrete” as they are for set A, the best fits to the data (using 4 or 6 layer fits) certainly suggest that annealing affected the depth profile in qualitatively the same way as it did for set A. The magnetization gradient is again more pronounced for the as-grown film, and again we see very strong evidence that annealing changed the chemical makeup of the surface of the film, consistent with Mn_I diffusion.

3.10 Set C: Annealing Dependence, Minimally Changing Depth Profile

The third set of samples we’ll consider is another as-grown/annealed pair of approximately 50 nm film thickness, denoted as set “C”. The Mn_{Ga} concentration was $x \approx 0.081$. Even though this sample was grown and annealed under nominally the same conditions as the previously discussed samples, magnetotransport measurements revealed

some surprising differences. The as-grown sample showed a maximum resistivity of $\rho_{max} \approx 0.009 \Omega \cdot \text{cm}$ at $T_C \approx 70 \text{ K}$. This is a substantial increase in as-grown T_C as compared to the other two as-grown samples discussed, suggesting an increase in hole concentration and a reduced Mn_I concentration. The as-grown ρ_{max} is noticeably lower for set C, as compared to the other two, also consistent with increased hole concentration [49]. For the annealed sample, $\rho_{max} \approx 0.003 \Omega \cdot \text{cm}$ at $T_C \approx 140 \text{ K}$. This T_C is higher and ρ_{max} is lower than the other two annealed samples, again consistent with an increased hole concentration. These results are consistent with room-temperature Hall effect measurements, which show the set C samples to have larger carrier concentrations, p than the other two sets. Values of p , ρ_{max} , and T_C for all three sets of samples are summarized in Table 3.1. What all of this suggests is that the as-grown sample of set C was somehow grown with a lower Mn_I concentration than those of sets A and B, despite all of them being grown together at the same time!

PNR measurements were taken on NG-1 after applying $H = 6.6 \text{ kOe}$ in-plane, and cooling the samples to low temperature ($T = 20$ for the as-grown, $T = 16 \text{ K}$ for the annealed). The samples were oriented with a $[100]$ direction nominally parallel to H . The as-grown film was broken during instrument alignment, resulting in use of a 1.0 cm by 1.5 cm piece (instead of the typical 2 cm by 2 cm), which significantly reduced the available intensity. In addition, the small sample size made instrumental alignment more difficult, causing the apparent critical θ to vary more than usual from that expected for GaAs (see section 3.3). Another problem with the scan of the as-grown sample, was a problem with control of one of the reflectometer slits, resulting in exceptionally high

Set	As-Grown p (290 K) (10^{19}cm^{-3})	Annealed p (290 K) (10^{19}cm^{-3})	Δp (290 K) (10^{19}cm^{-3})	As-Grown ρ_{max} ($\Omega\cdot\text{cm}$)	Annealed ρ_{max} ($\Omega\cdot\text{cm}$)	As-Grown T_C (K)	Annealed T_C (K)
A	5.97	12.1	6.13	0.035	0.005	60	125
B	5.08	11.1	11.1	0.036	0.006	60	125
C	9.78	21.2	11.4	0.009	0.003	70	140

Table 3.1: Summary of the hole concentrations, resistivities and Curie temperatures of the three as-grown/annealed pairs discussed in this chapter. Note that set C is significantly different from the other two sets.

background for a “mid- Q ” region of the scan. While we obtained good statistics at low- Q , the above discussed problems resulted in lower quality data for the as-grown sample at high- Q . The scan of the annealed sample was of very high quality. Several background scans were added and used to correct the annealed sample’s data. For both samples, SF data was taken with lower statistics than the NSF data, but was found to be minimal.

Figure 3.21 shows a comparison of the as-grown and annealed films for each of the fitted NSF reflectivities. The aforementioned difficulties in alignment of the as-grown sample cause a shift in Q that makes qualitative differences between the two films more difficult to see. However, for the spin-down reflectivities, the high- Q intensity is fairly similar for the two films (although the peaks are Q -shifted). For the spin-up reflectivities, the annealed film has higher intensity than the as-grown, but that is somewhat misleading, as alignment differences cause the annealed film’s intensity to be significantly higher at all Q - therefore there is no high- Q increase *relative* to low- Q . So, we observe no strong qualitative evidence for an altered surface layer on the annealed film. Differences in oscillation frequency between the two films are subtle, making qualitative assessment of film thickness difficult. However the phase shift between the as-grown and annealed spin-down reflectivities increases noticeably with Q , suggesting a difference in interfacial roughness between the films. Additionally, we observe damped oscillations for the annealed film’s spin-up reflectivity, implying differences in magnetization.

Figure 3.22 compares the fitted NSF reflectivities for the as-grown and annealed films. While the as-grown sample’s data is of lower quality, close inspection of Figure

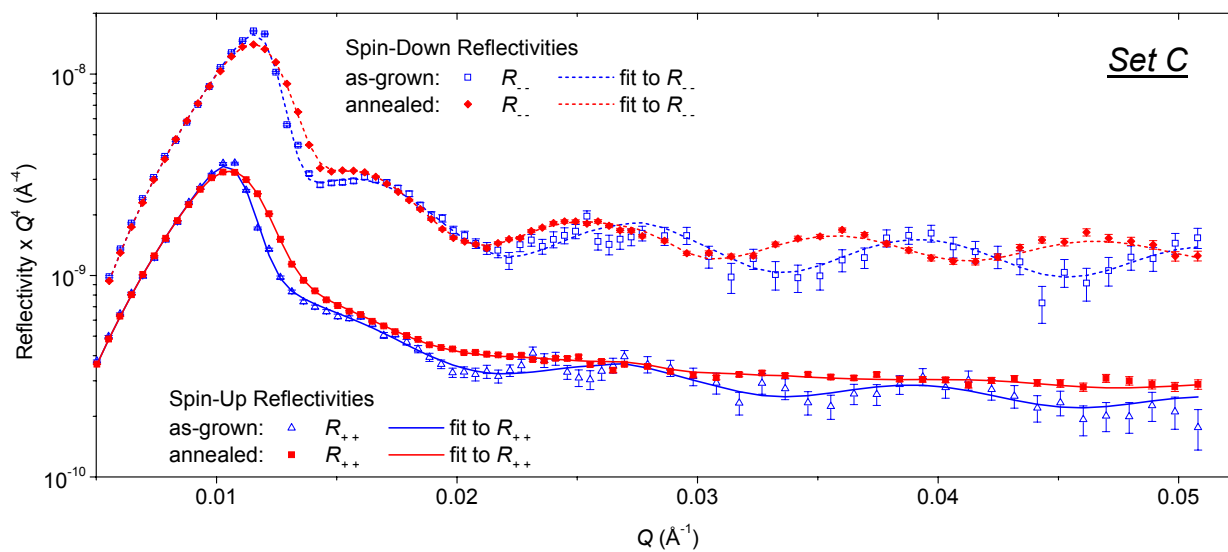


Figure 3.21: Comparison of the as-grown and annealed set C 50 nm films for each of the fitted NSF reflectivities. The high- Q intensities are fairly similar for both films.

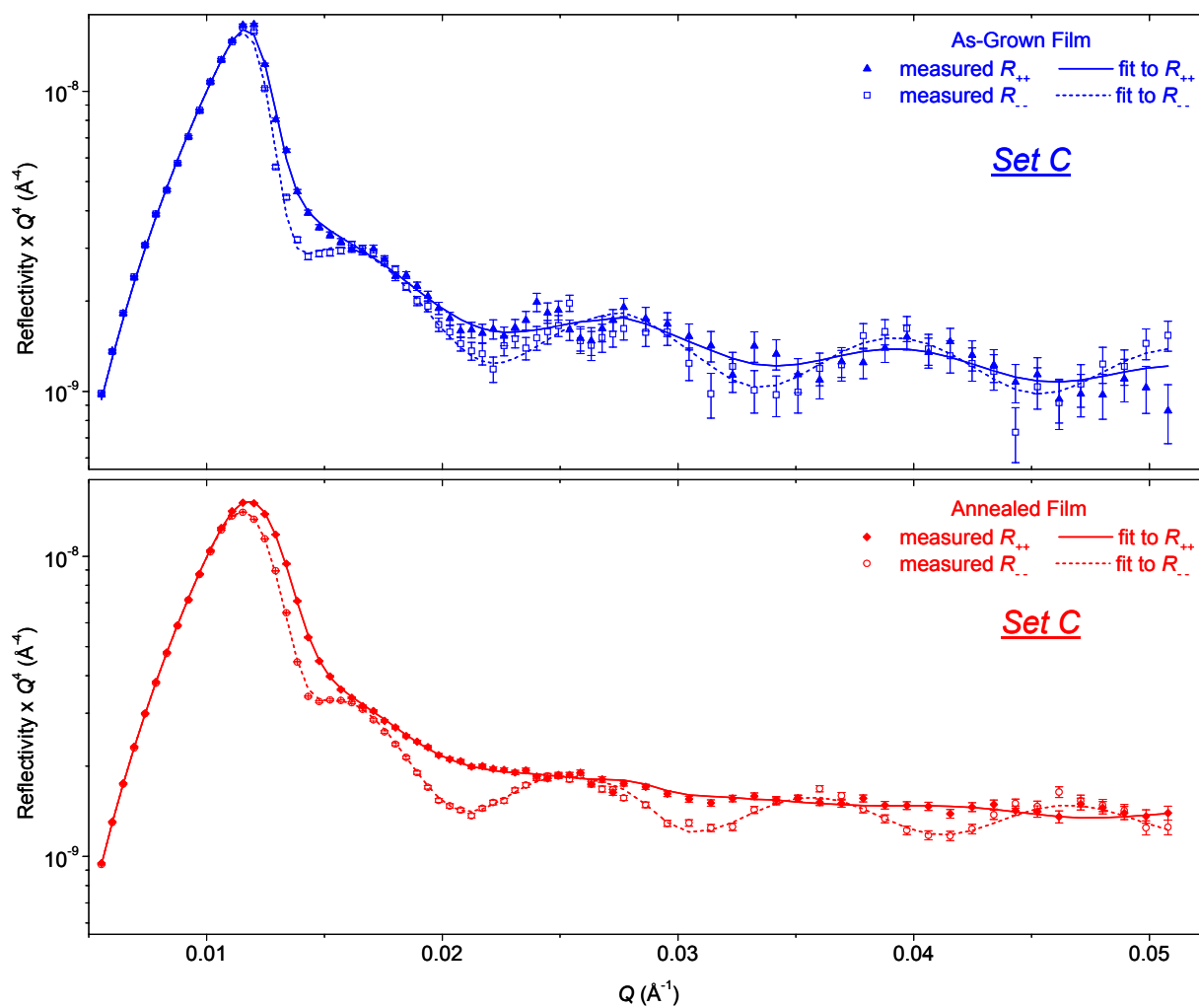


Figure 3.22: Comparison of the NSF reflectivities and fits for the as-grown and annealed set C 50 nm films. There is no sign of ribbon formation for either film.

3.22 reveals that the as-grown and annealed reflectivities are very similar. In particular, we see no evidence of a ribbon for either film. The fitted spin asymmetries for the as-grown and annealed films are shown in Figure 3.23. This figure reiterates the similarities in the films, especially at very low- Q . The amplitudes of the first peaks are very similar for both films, suggesting that the difference in magnetization upon annealing is not as large as for the other sets. More importantly, there is no discernable difference in *peak smearing* between the films. This suggests that *neither* film has a magnetization gradient. While the error bars for the as-grown film increase significantly after the first peak, it appears that the peak amplitude does become noticeable larger for the annealed film after that point, suggesting some increase in net magnetization. Both films' spin asymmetries cross zero in similar ways, suggesting similar dropoffs in magnetization at the surface.

The as-grown and annealed SLD models used to fit the PNR data are shown in Figure 3.24. The reduced data quality for the as-grown film requires that we interpret the model very carefully. The model consists of four layers, and shows a chemically and magnetically discrete substrate interface, followed by relatively constant chemical and magnetic SLD's. Notice the absence of a magnetization gradient. There is great certainty in this feature of the model, as it results from the lack of smearing between the first two spin asymmetry peaks - something that occurs at Q -values where the statistics are still very good. There is a small "hitch" in the chemical SLD near the substrate, but it is likely that feature is not "real", and is instead due to the reduced quality of the data at high- Q . At the surface of the as-grown film we see a drop in the magnetization, accompanied by a small drop in the chemical SLD. The surface drop in magnetization is fairly reliable, as it originates from the spin-asymmetry crossing zero at high- Q - a very

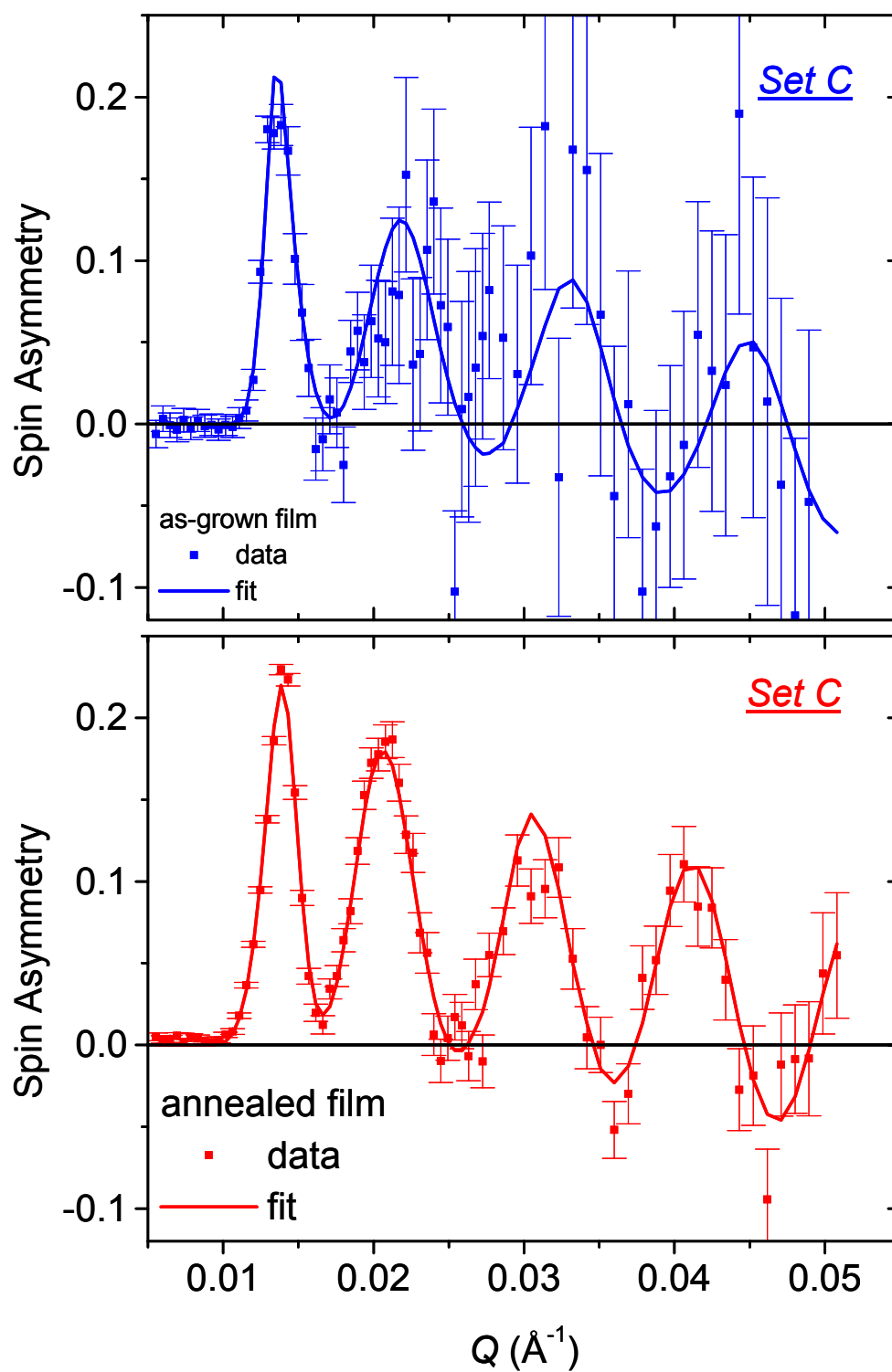


Figure 3.23: Fitted spin asymmetries for the set C 50 nm films. Aside from peak amplitude, the two films are very similar.

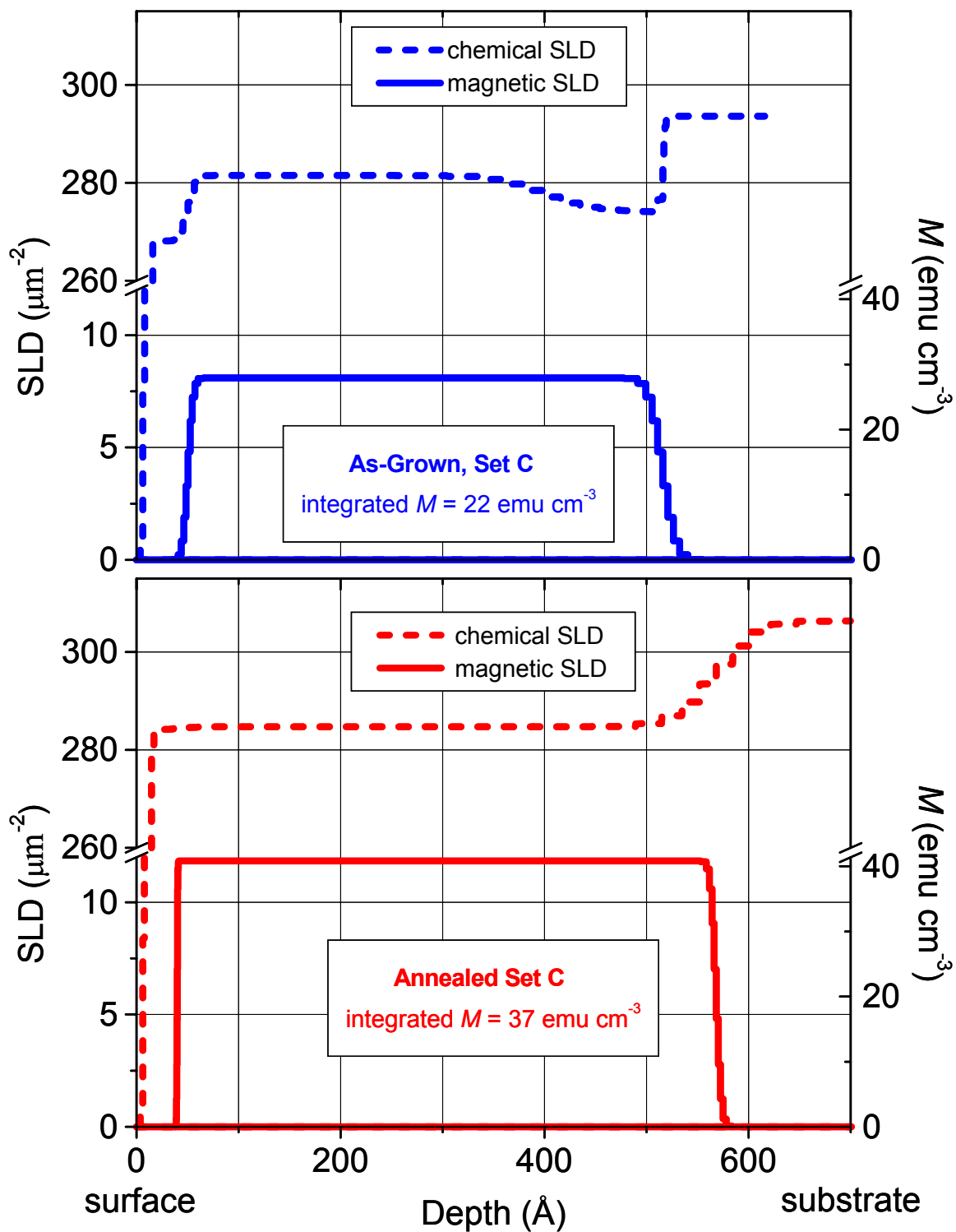


Figure 3.24: Scattering length density models used to fit the set C PNR data. Aside from an increase in integrated M , the two models are quite similar.

prominent feature of the data. However, the surface drop in chemical SLD is far less reliable, as this feature could be the result of uncertainty in the footprint correction (see section 2.7) due to the reduced size of the broken sample. The integrated magnetization for the model is $23 \text{ emu}\cdot\text{cm}^{-3}$.

The model for the annealed film consists of 3 layers. Again we see an increase in the net magnetization (integrated magnetization is $37 \text{ emu}\cdot\text{cm}^{-3}$), although this increase is not as great as for the other sets. Additionally, the annealed film again has a much chemically rougher substrate interface. The magnetically active region of the annealed film *appears* to be thicker, but the thickness shown in the as-grown film model may not be reliable - again due to the reduced data quality at high- Q . Other than these features, the model for the annealed film is very similar to that of the as-grown. There is a region of decreased magnetization near the surface, but there is no spike in the chemical SLD, meaning there is no direct evidence for a MnN surface layer. However, the increased T_C and magnetization upon annealing strongly imply that some Mn_I must have diffused to the surface of the annealed film. This can be explained, as the slightly increased film thickness of the annealed model is consistent with a thin Mn or MnN surface layer that is either too thin or too dilute to establish contrast with the Ga_{1-x}Mn_xAs film.

The results for set C are most interesting, as we observe that a sample that appears to have an increased as-grown carrier concentration shows neither a magnetization gradient before annealing, nor large-scale changes in surface chemical composition after annealing. Since Mn_I are donors that reduce the hole (carrier) concentration, this gives further evidence that magnetization gradients are due to an increased Mn_I/Mn_{Ga} ratio over

a region near the substrate. Additionally, reduced Mn_I concentration could explain why we observe less evidence of a chemically altered film surface after annealing. If there are fewer impurities to begin with, there are fewer to send to the surface! However, if indeed that is the case, there remains an unresolved problem. If fewer Mn_I are being diffused to the surface of sample C during annealing, it is unclear why it would show increases in T_C and hole concentration that are similar to those of the other two samples! With enough imagination, there are several ways in which this apparent paradox could *conceivably* be resolved (Mn_I moving to Ga sites during annealing, other mechanisms for improving T_C during annealing, ...etc.) , but at this point, such explanations are mere speculation. Despite this lingering puzzle, what is important and interesting is that we observe a distinct correlation among as-grown T_C , magnetization gradient, and annealed surface properties.

A remaining question is why set C apparently has a lower as-grown Mn_I concentration than the other two sets, when all three were grown together under the same growth conditions! The likely answer is that the growth conditions weren't *really* identical. During growth in the MBE chamber, each of the sample substrates was held in place with a Mo block. While the region below the block was held at a constant growth temperature, each of the individual blocks probably has a slightly different heat conductivity. So, it is possible that for some of the samples, the temperature was changing slightly during the growth. Since the location of Mn in the lattice (substitutional or interstitial) is dependent upon the thermodynamics of the system (see section 1.7), this slightly changing temperature could produce variations in the Mn_I/Mn_{Ga} ratio - resulting in lower overall carrier concentration, and a magnetization gradient! If

this is the case, these results show just how extremely sensitive $\text{Ga}_{1-x}\text{Mn}_x\text{As}$ growth is to the smallest changes in growth conditions.

3.11 Early Work

The earliest PNR studies we performed were conducted on an as-grown, and annealed $\text{Ga}_{1-x}\text{Mn}_x\text{As}$ samples each of approximately 100 nm film thickness, and Mn_{Ga} concentration of $x \approx 0.07$. However, this was not an as-grown/annealed pair, as they were separately grown samples. The data were of very low quality as compared to the later data, due to inexperience in measuring such dilute magnetic systems. However, some of the measurements of the annealed film were of extreme importance, as experiments carried out in collaboration with Suzanne te Velthuis on POSY I at Argonne National Laboratory gave us our first PNR evidence of an altered surface layer in a successfully annealed $\text{Ga}_{1-x}\text{Mn}_x\text{As}$ film. Work on the as-grown sample using NG-1 was less successful, as PNR measurements were not completely reproducible. However, these measurements did produce evidence that this as-grown sample is different than the others we have studied, as it appears to have a chemically altered surface layer similar to what we have commonly observed for annealed films. Additionally, these measurements were unclear as to the presence of a magnetization gradient. While re-examining this as-grown sample using our improved techniques might be an interesting and valuable endeavor, it is one that we have not yet pursued, and remains an avenue for future study.

3.12 Conclusions

The results described in this chapter have verified several conclusions drawn from other workers' experiments, and have produced new ones. To summarize:

- Optimal annealing of $\text{Ga}_{1-x}\text{Mn}_x\text{As}$ can drastically change the chemical composition of the film surface - strongly suggesting that Mn_I impurities diffuse to the surface during annealing.
- Optimal annealing can greatly increase the net magnetization of $\text{Ga}_{1-x}\text{Mn}_x\text{As}$ films - implying that Mn_I reduce the magnetization as well as T_C .
- We observe magnetization gradients in some as-grown $\text{Ga}_{1-x}\text{Mn}_x\text{As}$ films, and find that annealing "smooths out" these gradients, without producing drastic changes to the chemical composition in that same region.
- For our "best" $\text{Ga}_{1-x}\text{Mn}_x\text{As}$ film (highest carrier concentration and T_C), we observe no as-grown magnetization gradient or chemically altered surface layer upon annealing - suggesting that each of those features are indicative of regions with increased Mn_I concentration.
- We commonly observe an increase in chemical roughness at the film/substrate interface with annealing.
- We have shown that PNR, typically applied to the characterization of concentrated magnetic systems, can also provide detailed information about the spatial distribution of magnetic ions in very dilute ferromagnetics.

Chapter 4

Effects of a Capping Layer on the $\text{Ga}_{1-x}\text{Mn}_x\text{As}$ Depth Profile

4.1 Introduction

In Chapter 3, evidence was presented to show that annealing produces its beneficial effects in $\text{Ga}_{1-x}\text{Mn}_x\text{As}$ by shaking Mn_I from the lattice, allowing it to diffuse to the film surface. We further explored Mn_I diffusion in this material by considering the effects that annealing has on a $\text{Ga}_{1-x}\text{Mn}_x\text{As}$ film *without* a free surface. This chapter describes polarized neutron reflectometry (PNR) experiments that examine $\text{Ga}_{1-x}\text{Mn}_x\text{As}$ films capped with GaAs. While we find that annealing of a capped sample has a small *negative* effect on its *net* magnetic properties, we observe no evidence that annealing produces large changes in the *depth-dependencies* of the sample's magnetization or chemical composition. This result suggests that the GaAs capping layer inhibits Mn_I diffusion not simply by providing a physical barrier that blocks the path of freed Mn_I , but

that it does so by somehow changing the environment of the entire film. Re \uparrow lpol parameters for each of the models shown in this chapter are summarized in Appendix A.

4.2 Capping Recap

In Chapter 1, it was pointed out that Mn at interstitial sites (Mn_I) in $Ga_{1-x}Mn_xAs$ fight ferromagnetism by aligning antiferromagnetically with Mn at Ga sites (Mn_{Ga}), and by annihilating valuable holes needed to mediate the ferromagnetic exchange among the Mn_{Ga} . Also in Chapter 1, experiments performed by Stone *et al.* were discussed, that showed that capping $Ga_{1-x}Mn_xAs$ films with as little as 10 monolayers of GaAs totally suppressed any increase of Curie temperature (T_C) or net magnetization (M) associated with annealing [33]. Furthermore, they observed small decreases in T_C and magnetization upon annealing when the GaAs cap exceeded 4 nm in thickness. These results, combined with those from surface studies [15], measurements of $Ga_{1-x}Mn_xAs/GaAs/Ga_{1-x}Mn_xAs$ trilayer structures [32], and our own PNR measurements [34, Chapter 3] provided strong evidence that annealing enhances the ferromagnetic properties of $Ga_{1-x}Mn_xAs$ by ripping Mn from interstitial sites, allowing it to diffuse to the surface, thereby freeing additional Mn_{Ga} to participate in the ferromagnetic exchange.

But, through what mechanism does a GaAs cap prevent this Mn_I diffusion? Both Edmonds [15], and Stone [33] have speculated that this phenomenon is electrostatic in nature. These authors propose that when positively charged Mn_I donor ions begin to diffuse into a GaAs layer, they cause the layer to become electron-doped. Since the acceptor Mn_{Ga} ions cause the $Ga_{1-x}Mn_xAs$ layer to be hole-doped, any small Mn_I

diffusion into the GaAs results in formation of a p-n junction at the $\text{Ga}_{1-x}\text{Mn}_x\text{As}/\text{GaAs}$ interface - severely limiting Mn_I diffusion. Under this scenario, if there is instead a free surface, Mn_I can travel there and be electrically pacified through oxidation (or *nitridation* -see Section 3.5), allowing for a large Mn_I buildup, and a corresponding enhancement of ferromagnetism in the $\text{Ga}_{1-x}\text{Mn}_x\text{As}$ layer. Evidence for the necessity of surface oxidation has been found by our collaborators at Notre Dame, as they have observed that annealing $\text{Ga}_{1-x}\text{Mn}_x\text{As}$ in vacuum instead of N_2 results in diminished enhancement of T_C [58].

The depth-sensitivity of PNR made it a natural choice to further explore the role played by a GaAs cap during annealing. By looking for evidence of annealing-dependent changes in chemical composition and/or magnetization of a capped film, the validity of Edmonds' and Stone's argument could be examined.

4.3 Sample Preparation and Net Characterization

The sample for this experiment was fabricated using molecular-beam epitaxy at Notre Dame. A $\text{Ga}_{1-x}\text{Mn}_x\text{As}$ film was prepared by first depositing a 160 nm GaAs buffer layer on a [001] GaAs substrate at a temperature of 580 °C, then cooling the substrate to 230 °C and adding another 2.7 nm GaAs buffer layer, before depositing approximately 100 nm of $\text{Ga}_{1-x}\text{Mn}_x\text{As}$, and then a 9 nm GaAs cap. Using x-ray diffraction, the Mn_{Ga} concentration of the film was established to be $x \approx 0.076$ (see section 3.2). This film was cleaved, and one piece was annealed in N_2 for 1 hour at 270 °C (nominally the same conditions as the uncapped samples described in Chapter 3), while another piece was left

as-grown. These pieces were further cleaved, providing separate specimens for PNR and SQUID magnetometry.

The net magnetizations of the as-grown and annealed films, obtained using the SQUID, are shown in Figure 4.1. Fields were applied to the samples along a [110] direction. These measurements show that, in sharp contrast with uncapped films, annealing does not improve the ferromagnetic properties of the film. In fact, we observe that annealing is detrimental to the film's ferromagnetic properties (in agreement with Ref. 33), as the low-field T_C is reduced from 53 K to 40 K, and the high-field magnetization at $T = 13$ K drops from $23 \text{ emu}\cdot\text{cm}^{-3}$ to $17 \text{ emu}\cdot\text{cm}^{-3}$. Hall effect measurements showed that the $T = 290$ K carrier concentration also dropped with annealing, from $p = 3.27 \times 10^{19} \text{ cm}^{-3}$ to $p = 2.14 \times 10^{19} \text{ cm}^{-3}$. Magnetotransport measurements revealed that annealing of a similar uncapped $\text{Ga}_{1-x}\text{Mn}_x\text{As}$ film in the same oven at the same time as the capped film resulted in a significant increase in T_C (from 40 K to 90 K) - providing further evidence that the GaAs cap is indeed responsible for ruining the beneficial effects of annealing.

4.4 PNR Measurements

PNR measurements were conducted at the NIST Center for Neutron Research (NCNR) using the NG-1 Reflectometer. A magnetic field of $H \approx 6.6 \text{ kOe}$ was applied in the plane of the film along a [100] direction before cooling the sample to low temperature. This procedure was performed for measurements at two different

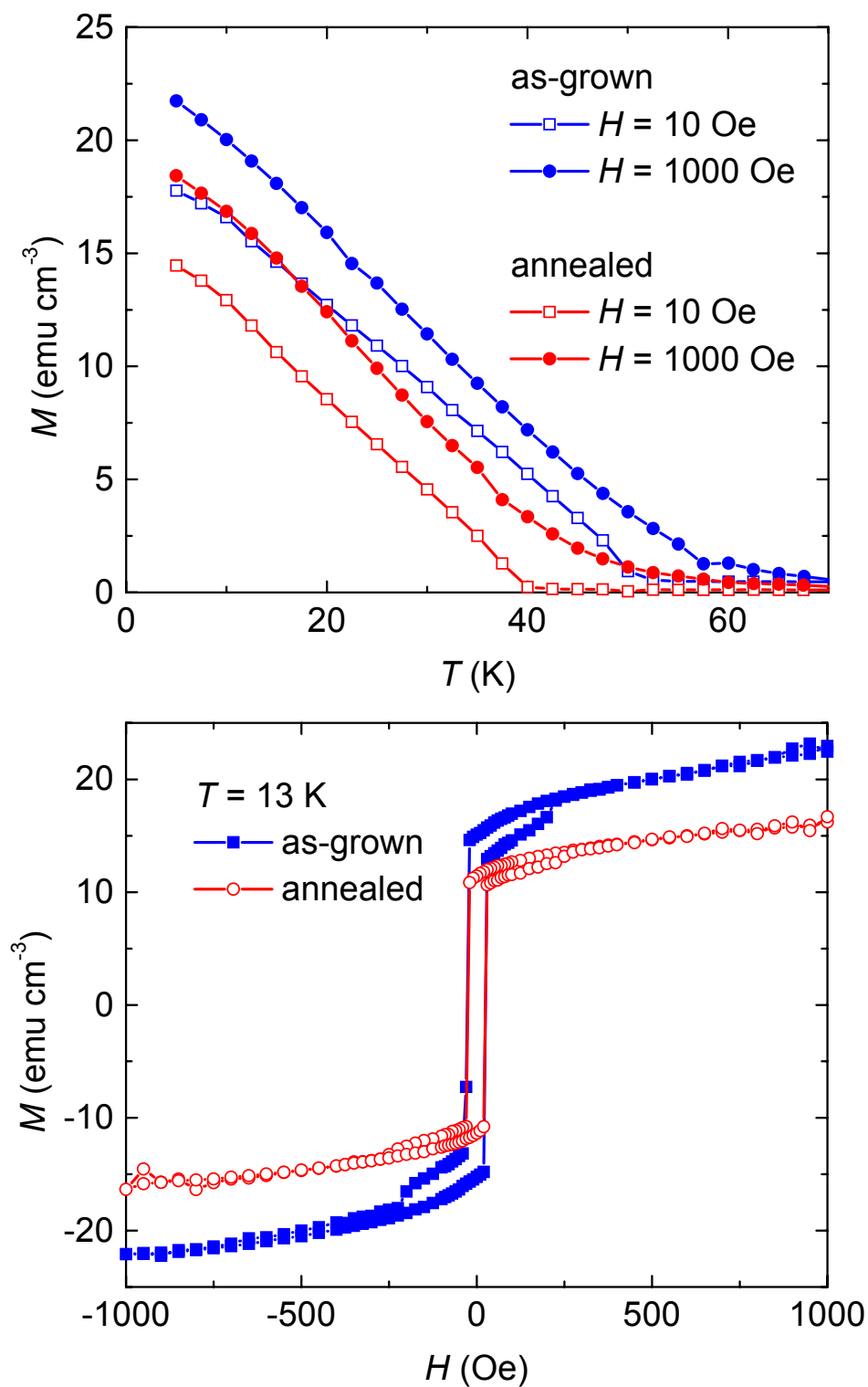


Figure 4.1: SQUID results showing the net magnetization of the as-grown and annealed films as functions of temperature (top), and applied magnetic field (bottom).

temperatures, 13 K, and 18 K. Background scattering was largely instrumental, as background for both samples matched each other, and several other different measurements taken under similar conditions, justifying addition of several background scans to improve statistics. Non spin-flip (NSF) and spin-flip (SF) reflectivities were measured, but the SF scattering was found to be minimal, and was used only to make polarization corrections to the data.

The data happened to be of slightly higher quality for the $T = 18$ K scans than for those at $T = 13$ K, so we will begin by considering the higher- T data. Figure 4.2 compares the as-grown and annealed films for each of the fitted NSF reflectivities, which can be qualitatively evaluated in a manner similar to that described in Chapter 3. The reflectivities are very similar, as there are no large-scale differences in peak periodicity (which would suggest thickness differences), peak amplitude (which would suggest large differences in SLD), or slope of the high- Q intensity (which would suggest differing surface compositions). The as-grown and annealed data are slightly shifted in relative intensity, which cause the as-grown data to *appear* more intense, but this is merely an effect of slight differences in instrumental alignment. A more meaningful difference between the two films is that the high- Q oscillations of the annealed film are slightly more damped than their as-grown counterparts. This feature suggests an increase in interfacial roughness upon annealing.

Figure 4.3 compares the fitted NSF reflectivities for the as-grown and annealed films. Plotted in this way, the as-grown and annealed films again look strikingly similar. A benefit of a 9 nm GaAs capping layer is improved contrast with the $\text{Ga}_{1-x}\text{Mn}_x\text{As}$ layer (as compared with air or a 5 nm MnN layer, as was the case with the Chapter 3 samples).

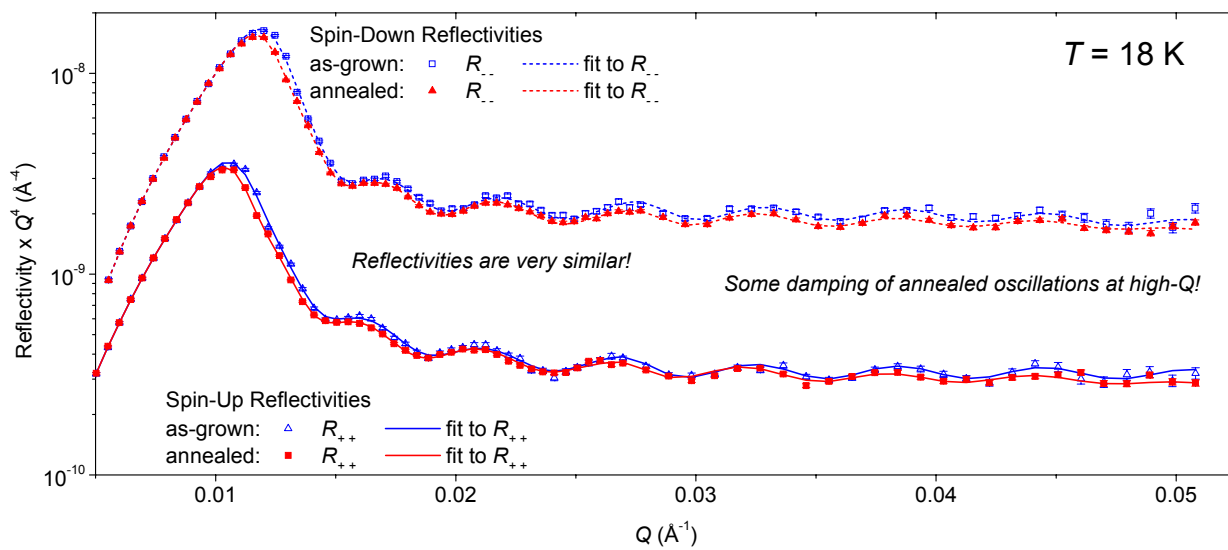


Figure 4.2: Comparison of as-grown and annealed NSF fitted reflectivities at 18 K.

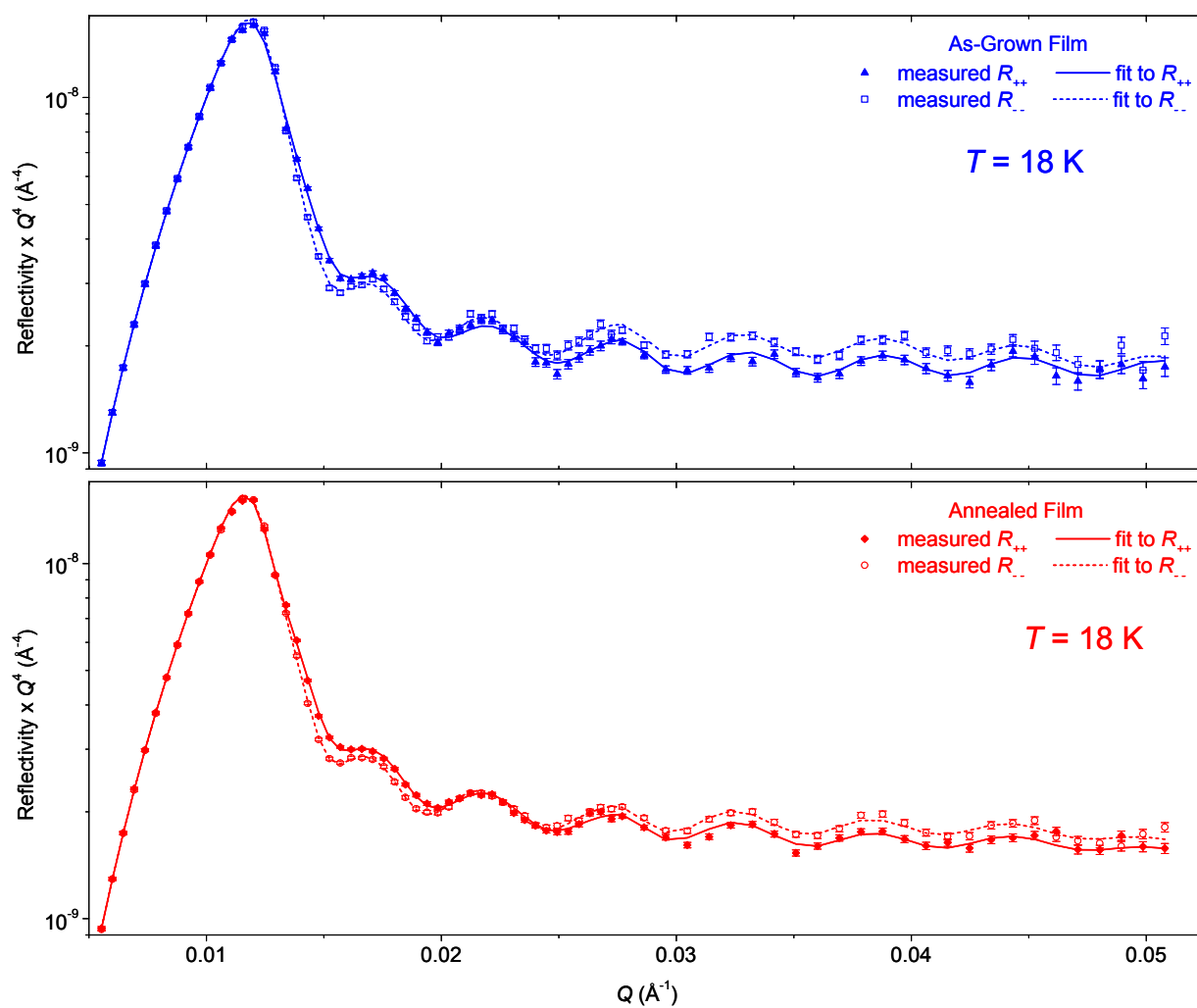


Figure 4.3: Comparison of fitted NSF reflectivities for the as-grown and annealed films at 18 K.

This results in “landmark” features in the data that help to reduce ambiguity of the fits. For example, the NSF reflectivities for both films form a ribbon at around $Q = 0.017 \text{ \AA}^{-1}$ (a feature that is shown in Chapter 3 to imply a magnetization gradient), and then undergo a “dead zone” where the spin-up/spin-down splitting begins to collapse at around $Q = 0.020 \text{ \AA}^{-1}$, before the splitting begins to become very large at about $Q = 0.027 \text{ \AA}^{-1}$.

The magnetic features of the PNR data are more apparent when recast as spin asymmetry (as defined in section 3.5), which is shown with fits in Figure 4.4. These plots clearly show the similarities in the films even at this high level of detail, and also reveal the high quality of the fits. Both films show low- Q smearing of the peaks (again - the telltale sign of a magnetization gradient), a crossing of zero at similar Q values, and large negative spin asymmetries at high- Q . The level of detail provided through spin asymmetry also shows a subtle difference in the films, as the lowest- Q peak of the as-grown film is slightly larger than its annealed counterpart. Since the low- Q spin asymmetry corresponds to the magnetization at large length scales, this difference is consistent with a slightly greater net magnetization for the as-grown film.

The fits to the PNR data in Figures 4.2 - 4.4 were generated from the SLD models shown in Figure 4.5. Bracketed by GaAs on either side, the $\text{Ga}_{1-x}\text{Mn}_x\text{As}$ film shows up clearly in each model, denoted by a region of decreased chemical SLD, and non-zero magnetic SLD. The models show the integrated magnetization for the as-grown film to be $26 \text{ emu}\cdot\text{cm}^{-3}$, and $20 \text{ emu}\cdot\text{cm}^{-3}$ for the annealed film. Since the GaAs caps constituted known, well-defined non-magnetic surface layers for these samples, *only* the thickness of the $\text{Ga}_{1-x}\text{Mn}_x\text{As}$ layer was used to calculate the integrated magnetizations. Uncertainty in the models’ *integrated* magnetizations (but not their depth-dependent magnetizations),

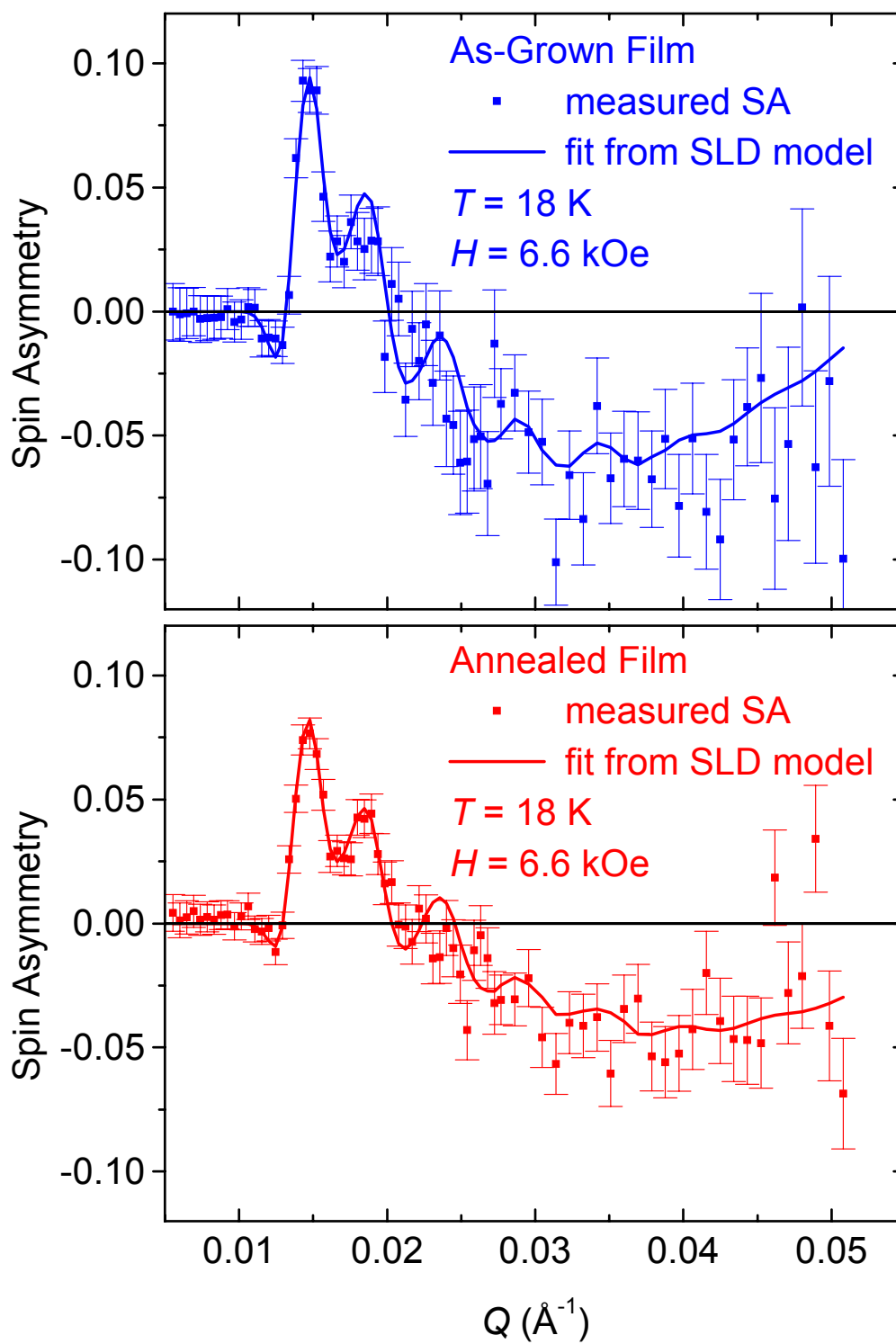


Figure 4.4: Spin asymmetries and fits at 18 K.

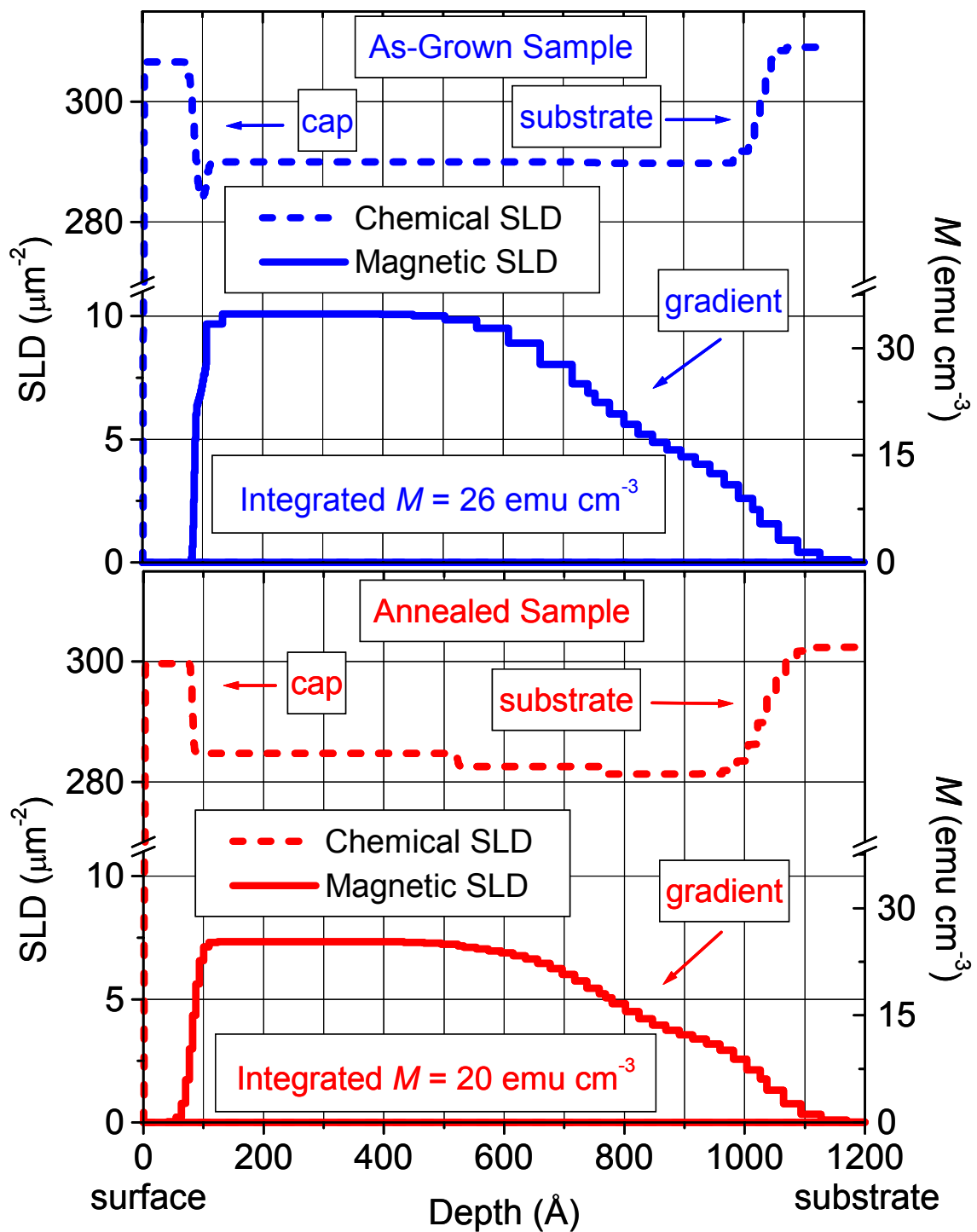


Figure 4.5: Scattering length density models used to fit the 18 K data.

was reconciled by choosing models in which the integrated magnetization is consistent with that obtained from the SQUID measurements.

These results are corroborated by PNR measurements taken at $T = 13$ K, which agree well with the $T = 18$ K data. The 13 K fitted reflectivities are shown in Figure 4.6, and are recast as fitted spin asymmetries in Figure 4.7. The fits to the 13 K data were produced with the SLD models shown in Figure 4.8, which are very similar to the 18 K data. The uncertainties associated with these models are also similar to those of the 18 K models.

4.5 Interpretation of PNR Data

An interesting difference between the two films is a small increase in chemical roughness at the substrate/film interface for the annealed film - a phenomenon also observed in the uncapped films of Chapter 3. Otherwise, we see that annealing changes the depth profiles very little. Both films feature a pronounced gradient in M that extends over a thickness of approximately $500 \text{ \AA} \pm 100 \text{ \AA}$. (Note that -- although the fit is not highly sensitive to the *exact* extent of this gradient -- the data unambiguously require that the models' magnetizations near the substrate be greatly depleted.) We therefore conclude that the reduction in net magnetization upon annealing occurs uniformly, and that annealing does not appreciably "smooth out" the magnetization as we commonly observe it to do for uncapped samples.

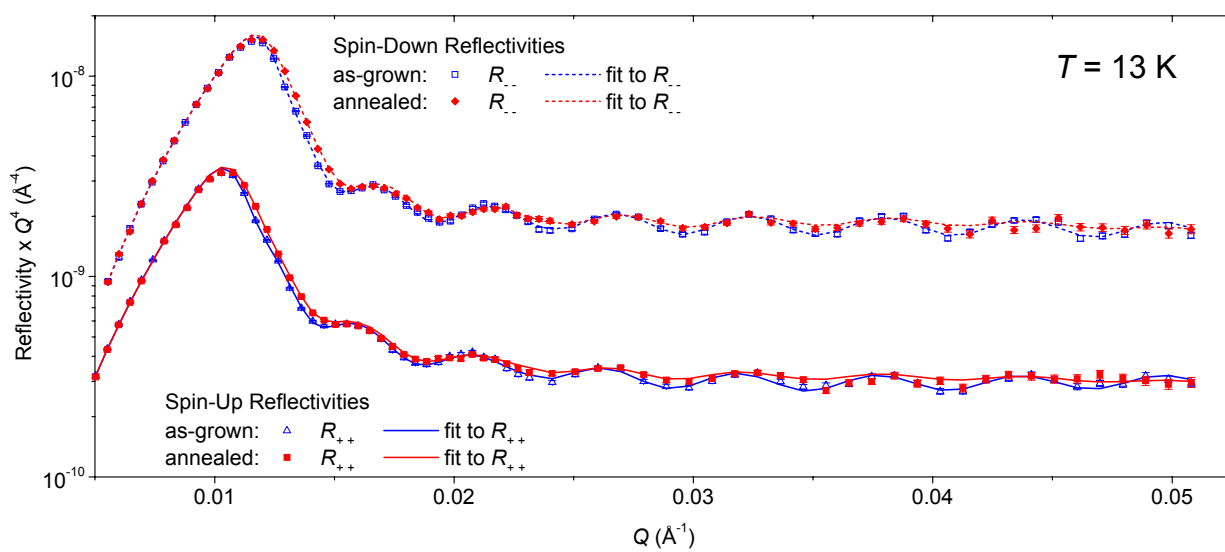


Figure 4.6: Comparison of the as-grown and annealed fitted NSF reflectivities at 13 K. The data are very similar to that at 18 K.

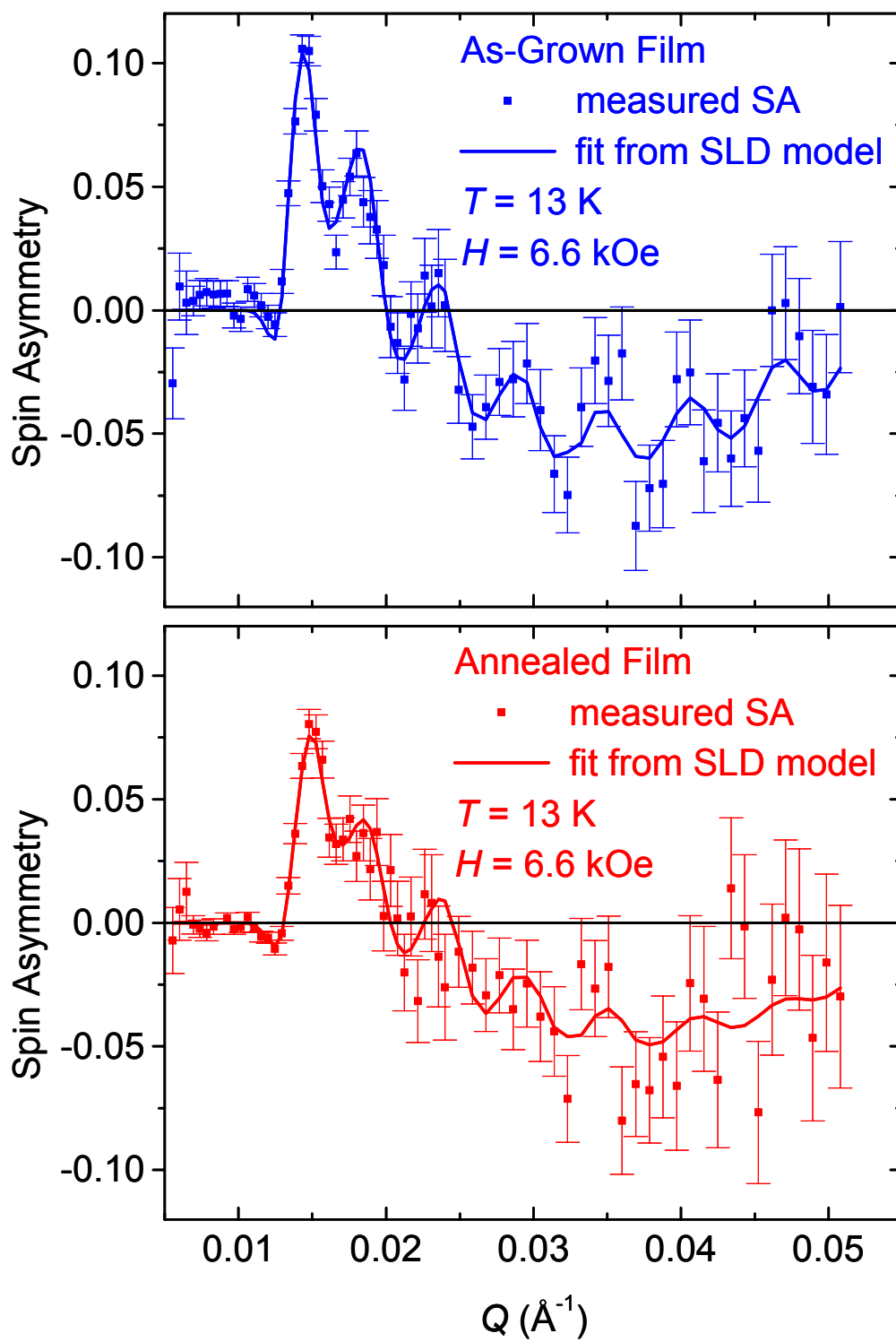


Figure 4.7: Spin asymmetries and fits at 13 K.

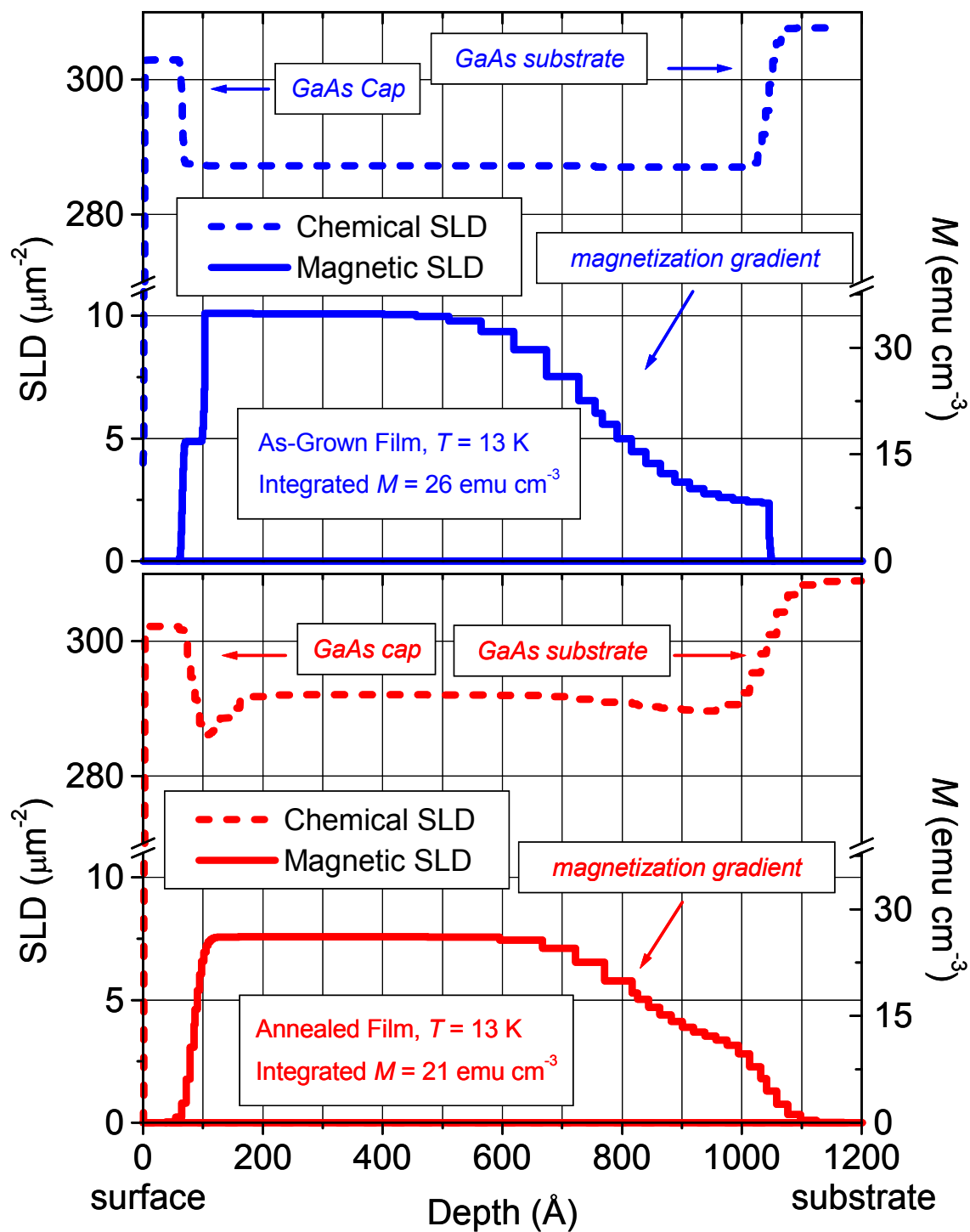


Figure 4.8 Scattering length density models used to fit the 13 K data.

These two films are further examples of the presence of magnetization gradients in films with low T_C and low net M . This further suggests that these gradients are correlated with increased Mn_I concentration. However, as was the case for uncapped films, the chemical SLD changes little over the region of graded magnetization - implying that the *total* Mn concentration is relatively constant. This reinforces the idea that the magnetization gradients are indicative of a non-uniform, depth-dependent ratio of Mn_{Ga} to Mn_I , due to small, depth-dependent differences in growth temperature. If this is the case, a magnetization gradient is a unique “signature” of the Mn_{Ga}/Mn_I ratio. If the energy added to the capped system through annealing was appreciably redistributing Mn_I , and the GaAs cap was merely a barrier to the liberated Mn_I as they “bounced around” during annealing, one would expect a significant change in this signature. That the signature instead remains virtually intact is significant, as it suggests that the GaAs cap somehow prevents *any* large-scale Mn_I redistribution. This result not only corroborates the formation of a p-n junction at the GaAs/ $Ga_{1-x}Mn_xAs$ interfaces during annealing [15, 33], it additionally suggests that the presence of two such interfaces somehow inhibits migration of Mn ions from the outset. However, while it does not appear that large amounts of Mn_I are vertically migrating during annealing, it is possible that the added energy causes a *small* number of Mn to break free of the lattice, and form Mn clusters or MnAs inclusions. These Mn may well be freed from Ga sites, in addition to interstitial ones - resulting in a net loss in ferromagnetically active Mn_{Ga} , which could explain the observed drop in T_C and net M upon annealing.

4.6 Conclusion

In summary, we have observed that a GaAs capping layer not only eliminates the beneficial effects of annealing, but it also appears to prevent annealing from altering the depth-dependence of the magnetization in $\text{Ga}_{1-x}\text{Mn}_x\text{As}$. This suggests that the cap somehow inhibits large scale vertical migration of Mn_I . Additionally, these results lend further support to a model of annealing for uncapped $\text{Ga}_{1-x}\text{Mn}_x\text{As}$ in which the added energy pries Mn_I ions from the lattice, allowing them to eventually diffuse to the free surface - freeing additional Mn_Ga to participate in the ferromagnetic exchange. Finally, we see more evidence that a non-uniform magnetization is a common pitfall of $\text{Ga}_{1-x}\text{Mn}_x\text{As}$ growth - a factor that may warrant consideration for potential device applications.

Chapter 5

Search for Magnons in $\text{Ga}_{1-x}\text{Mn}_x\text{As}$

5.1 Introduction

For the final chapter of this dissertation, we will switch gears, and discuss the results of *inelastic* neutron scattering measurements performed on $\text{Ga}_{1-x}\text{Mn}_x\text{As}$ samples. These experiments constituted an ambitious effort to be the first to detect magnons (spin-waves) [59] in this very dilute ferromagnetic system. While some very weak evidence of magnons was found, the evidence was inconclusive and not wholly reproducible. So, the following discussion describes a study that is incomplete, and has primary utility as a starting point for future attempts to detect magnetic excitations in this challenging material.

5.2 Theoretical Magnon Dispersion

In order to determine limits on T_C for $\text{Ga}_{1-x}\text{Mn}_x\text{As}$, it is important to understand the fundamental exchange interactions between magnetic ions. This understanding

would benefit from a measurement of the energy required to excite (or annihilate) a propagating precession of the ferromagnetically aligned Mn_{Ga} ions about their z -axes. Such collective excitations are known as magnons, or spin-waves, and the energy associated with them is typically dependent on the excitation wavevector q . The q -dependence of the magnon energy is known as the magnon dispersion.

In the Heisenberg model of the ferromagnet [60], the system Hamiltonian is described in terms of an *exchange energy* J that results from electrostatic interactions among atoms, and the Fermionic asymmetry of those atoms' electrons. In the approximation that only interactions among nearest neighbor Mn_{Ga} ions are considered, the Heisenberg magnon dispersion is expressed as

$$E_m = 2rJS \left\{ 1 - \frac{1}{r} \sum_{\rho} \exp(i\mathbf{q} \cdot \boldsymbol{\rho}) \right\}, \quad (36)$$

where r is the number of nearest neighbors, S is the Mn_{Ga} spin ($5/2$), and $\boldsymbol{\rho}$ is the position vector between interacting ions. For $\mathbf{q} \cdot \boldsymbol{\rho} \ll 1$ (i.e. low q), Eq. 36 can be approximated to a parabolic form

$$E_m \approx Dq^2, \quad (37)$$

where D is the spin stiffness – very apt nomenclature, as D is a measure of how “securely” magnetic moments are held in ferromagnetic alignment. Eq. 37 describes a

“pure” Heisenberg system with isotropic magnons, but real systems commonly feature a constant energy gap Δ in addition to the quadratic term,

$$E_m \approx \Delta + Dq^2. \quad (38)$$

The energy gap usually arises from a magnetic anisotropy, and is a measure of the energy required to excite a magnon of infinite wavelength. In the nearest-neighbor Heisenberg model, the spin stiffness is predicted to be dependent on the number of nearest neighbors, and the distance between them

$$D = \frac{rJS\rho^2}{3}. \quad (39)$$

But, with $\text{Ga}_{1-x}\text{Mn}_x\text{As}$, we are dealing with a very dilute, random distribution of ions that do not have well defined nearest neighbors, and are thought to communicate via a long-range interaction mediated by itinerant carriers. Therefore, a more complex model is likely required to describe the spin stiffness in $\text{Ga}_{1-x}\text{Mn}_x\text{As}$.

König *et al.* have used a Kohn-Luttinger Hamiltonian [61] to produce a theory of the long wavelength magnetic properties of $\text{Ga}_{1-x}\text{Mn}_x\text{As}$ that attempts to account for details of the GaAs semiconductor band structure [62]. In König’s model, the magnon dispersion is

$$E_m = \frac{2\lambda_1\lambda_2}{NS} + \frac{2A}{NS}q^2 + \mathcal{O}(q^4), \quad (40)$$

where N is the Mn_{Ga} number density, A is an exchange constant, and λ 's 1 and 2 are anisotropy parameters. To order q^2 , Eq. 39 is of the same form as Eq. 38, therefore, in Heisenberg terms, the energy gap is

$$\Delta = (2\lambda_1\lambda_2) / (NS), \quad (41)$$

and the spin stiffness is

$$D = (2A/NS). \quad (42)$$

Numerical calculations in Ref. 62 suggest that the energy gap is small compared to the energy bandwidth, and that the spin stiffness is nearly isotropic. Furthermore, the authors numerically calculate the zero-temperature spin stiffness as a function of itinerant-carrier concentration p for two experimentally plausible values of the exchange energy density J_{pd} [63, 64, 65]. While not terribly precise, these calculations of D provide a starting point for trying to experimentally map the magnon dispersion.

5.3 Inelastic Neutron Scattering

Thermal neutrons are the ideal probe for probing magnetic excitations in solids, as the neutron magnetic moment can interact with moments in the sample, and the neutron

energy is comparable to the typical energy range of the excitations. This is the realm of *inelastic neutron scattering*, in which neutrons of a known energy E_i are incident on a sample, and scattered neutrons are looked for at a specific final energy E_f . Thus, by either fixing E_i and scanning E_f (or vice-versa), one can measure the scattered intensity as a function of energy transfer,

$$\Delta E = E_i - E_f. \quad (43)$$

This change of energy can then be attributed to the creation or annihilation of an excitation in the sample. Commonly, inelastic measurements made on a triple-axis spectrometer (see below) also allow for selection of a particular wavevector transfer that corresponds to the selected energy transfer. The wavevector transfer is defined in terms of the incident and final neutron wavevectors, \mathbf{k}_i and \mathbf{k}_f

$$\mathbf{Q} = \mathbf{k}_i - \mathbf{k}_f = 2\pi\boldsymbol{\tau} + \mathbf{q}, \quad (44)$$

where $\boldsymbol{\tau}$ is a reciprocal lattice vector corresponding to the crystal structure of the sample, and \mathbf{q} is the wavevector associated with the excitation.

The standard instrument for measuring the scattered intensity as a function of energy transfer and wavevector transfer $S(\Delta E, \mathbf{Q})$ is the triple-axis neutron spectrometer [66]. Triple -axis refers to the three primary scattering events that occur as a neutron travels from the source to the detector

- Off a monochromator crystal, which scatters only [67] neutrons of energy E_i towards the sample
- Off the sample, resulting in scattered neutrons with a spectrum of E_f and Q values
- Off an analyzer crystal, which scatters only neutrons of a desired energy E_f towards the detector.

5.4 World Record Samples

In order to attempt inelastic measurements, $\text{Ga}_{1-x}\text{Mn}_x\text{As}$ films thicker than any ever produced were required. With this in mind, Tomek Wojtowicz of Prof. Furdyna's group at Notre Dame endured a tour de force of MBE films growth, and produced a series of $\text{Ga}_{1-x}\text{Mn}_x\text{As}$ films each with a thickness on the order of 10 μm - world record samples, to the best of our knowledge. However, the increased thickness did limit the Mn_{Ga} concentration x to approximately 0.04 for each of the samples, and T_C was only 47 K. Hall effect measurements revealed a carrier concentration of $p \approx 0.065 \text{ nm}^{-3}$. Attempts to enhance these samples through annealing were unsuccessful - likely because interstitial Mn could not reach the surface in such a thick (two orders of magnitude larger than those discussed in Chapter 3) sample.

5.5 SPINS Measurements

Assisted by Sungil Park, inelastic neutron scattering measurements were made using the SPINS triple-axis spectrometer at the NCNR. To maximize magnetic signal, six of the thick $\text{Ga}_{1-x}\text{Mn}_x\text{As}$ samples were stacked together for measurement, providing a collective $\text{Ga}_{1-x}\text{Mn}_x\text{As}$ layer thickness of 46.1 μm . The instrument was aligned on the

[200] Bragg peak in reflection geometry, and constant- Q scans were taken in the $[q00]$ direction. The final energy was fixed at 5 meV, and the energy resolution was approximately 0.2 meV. 80° collimation was used between the monochromator and the sample, and between the sample and the analyzer. Counting times ranged from 20-30 minutes per q value, and the intensity was approximately 500,000 counts per minute. Fig. 5.1 shows scans at four different q values that (with a little imagination) show some evidence of excitations. The red solid lines are Gaussian fits to the data. Using those fits to determine energy positions, the magnon energy dispersion is shown in Fig. 5.2. The spin stiffness and energy gap were then determined by fitting the data to a parabola (in accordance with the Heisenberg or König models). The fit is shown in red, and indicates that $D = 53 \text{ meV}\cdot\text{\AA}^2$, and $\Delta = 0.3 \text{ meV}$.

These results can be compared with the theoretical results of König's six-band Luttinger model. By plugging the numerically calculated value of the exchange constant A from Ref. 62, and the experimentally determined value of the Mn_{Ga} number density N into Eq. 42, a König model estimate of D can be determined. The calculations for A as a function of p were carried out for two values of J_{pd} that correspond to low and high-end estimates for $\text{Ga}_{1-x}\text{Mn}_x\text{As}$ with optimal x , and $T_C = 110 \text{ K}$. Since our samples have lower x and T_C , the most reasonable comparison is with the calculation utilizing low-end $J_{pd} = 68 \text{ meV}\cdot\text{nm}^{-3}$. Furthermore, the minimum p at which A was calculated was 0.1 nm^{-3} , which is still about double the value found for our samples. That, coupled with the fact that the calculations were done for zero temperature, while the measurements were done at $T = 20 \text{ K}$ (which could noticeably soften the dispersion), imply that the calculated D should be taken as an *upper limit* on the spin stiffness. With all of this in mind, the

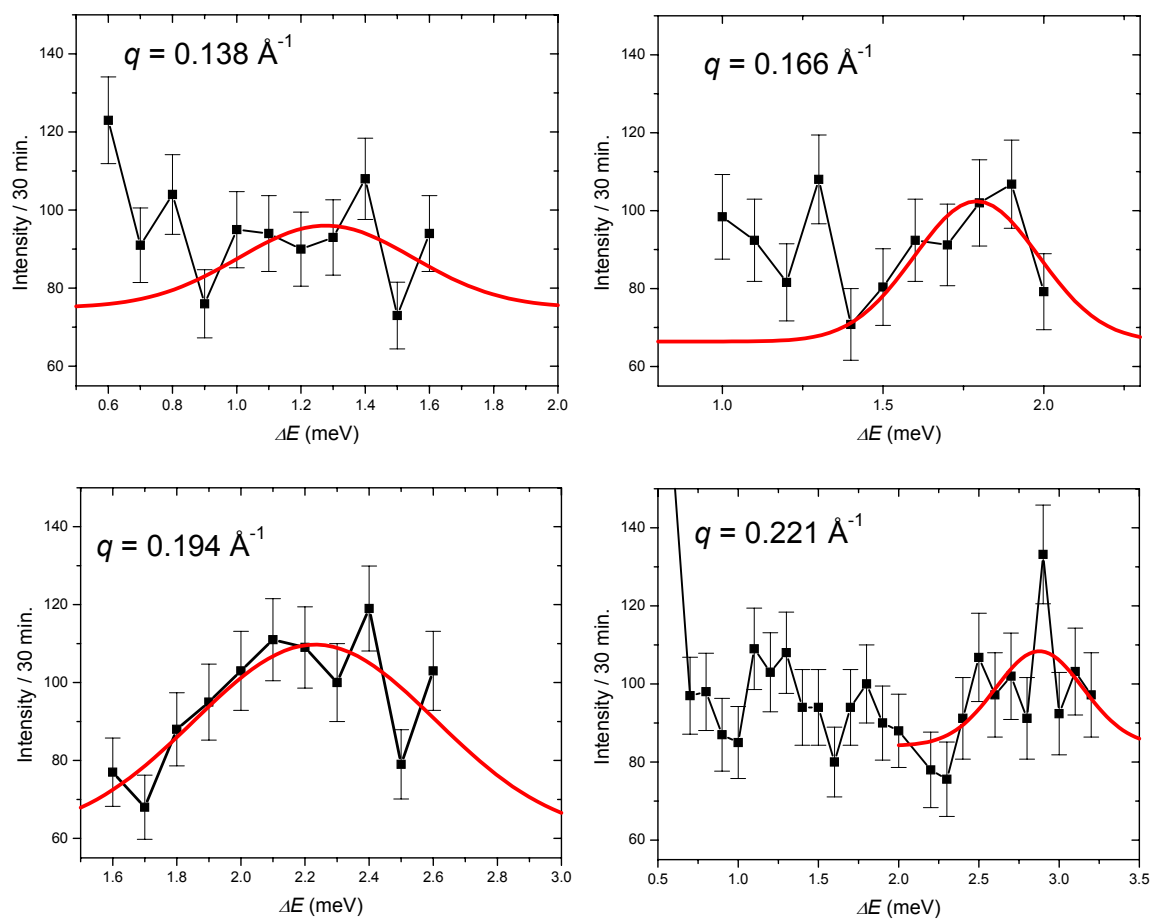


Figure 5.1: Scattered neutron intensity as a function of energy transfer for selected wavevectors. Solid red lines are gaussian fits to the data.

König value of the spin stiffness is estimated to be $D = 182 \text{ meV}\cdot\text{\AA}^2$. This value is used in Eq. 37 to produce a theoretical dispersion, which is shown as the blue dashed line in Fig. 5.2. Since König's calculations suggest that Δ is small compared with the energy bandwidth, it is taken to be zero for our purposes. Comparison of the measured and calculated dispersion insinuates that the measured dispersion is at least plausible.

However, the evidence we find for these excitations is quite weak, as the data shown in Fig 5.2 are far from being conclusive. Furthermore, a later set of SPINS measurements did not reproduce the peak found at $q = 0.194 \text{ \AA}^{-1}$, and found no evidence of low energy (scanning 0-1 meV) excitations at $q = 0.111 \text{ \AA}^{-1}$ (which should have been present if the original dispersion was correct). While it is conceivable that instrumental differences between the two experiments accounts for this lack of reproducibility (increased background for instance), it is also entirely possible that the original data does not constitute actual excitations. Therefore, this study is definitively non-definitive.

If this study is to be continued, and the magnon dispersion in these samples is to be further pursued, the experiments should:

1. employ energy scans that encompass the full-range of reasonable magnon energies, at least to the upper-end dispersion suggested by the König model.
2. use increased statistics - with such low magnetic ion concentration, increased neutron count and reduced background will likely be required to produce believable evidence of magnetic excitations.

It may indeed be possible to map out the magnon dispersion in these samples, but it will require a much more involved effort (i.e. a lot more beamtime than we've received so far!).

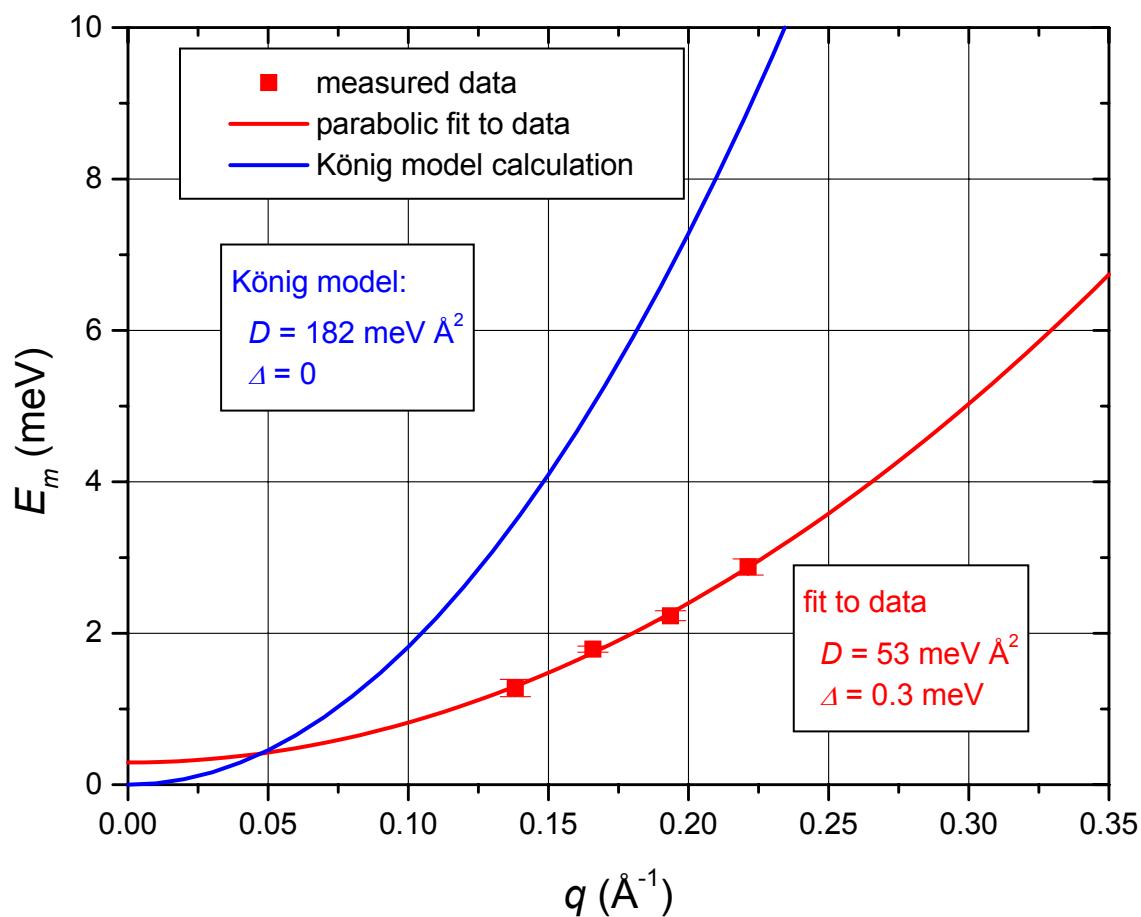


Figure 5.2: Measured and calculated dispersions. The König model should be taken as an upper limit for plausible spin stiffness D , in these samples. The measured dispersion is based on inconclusive data, and should not be considered reliable.

Appendix A

Reflpol Models

The following tables summarize the Reflpol parameters used to create the scattering length density models shown in Chapters 3 and 4 (see Section 2.7, and Ref. 43 for information about fitting PNR data with Reflpol). For all of the models, the magnetic layer thickness DM is restrained to be equal to the chemical layer thickness D, the absorption $MU = 2 \times 10^{-20}$ for each layer (except for the vacuum layer, where $MU = 1 \times 10^{-20}$), and the magnetic moment angle $TH = 270^\circ$ (unless otherwise noted). As for the beam parameters, for all models, intensity = 1.0, background = 1×10^{-10} , wavelength = 4.75 Å, and wavelength divergence = 0.021 Å.

Table A.1: Sample A, As-Grown, High-Field Scan

Layer	QC (10^{-4} \AA^{-2})	D (\AA)	RO (\AA)	QM (10^{-6} \AA^{-2})	RM (\AA)
1	1.39081	41.1642	5.0	1.69434	5.0
2	1.40242	90.9586	40.0	4.71854	40.0
3	1.39971	251.063	25.0	3.85932	90.0
4	1.40445	161.48	25.0	2.17344	160.0
5	1.54623	100.0	5	0.0	5.0

angular divergence = 0.0008 radians

Table A.2: Sample A, Annealed, High-Field Scan

Layer	QC (10^{-4} \AA^{-2})	D (\AA)	RO (\AA)	QM (10^{-6} \AA^{-2})	RM (\AA)
1	1.52533	49.2333	8.81511	1.84073	8.81511
2	1.38233	517.976	48.0	7.6985	10.0
3	1.50998	100.0	56.062	0	11.2303

angular divergence = 0.0008 radians

Table A.3: Sample A, As-Grown, High-Field Scan, 3 layers

Layer	QC (10^{-4} \AA^{-2})	D (\AA)	RO (\AA)	QM (10^{-6} \AA^{-2})	RM (\AA)
1	1.38555	41.0	5.0	1.6	5.0
2	1.40502	500.594	5.0	3.54008	5.0
3	1.54481	100	7.63182	0.0	25.0

angular divergence = 0.0008 radians

Table A.4: Sample A, Annealed, High-Field Scan, 5 layers

Layer	QC (10^{-4} \AA^{-2})	D (\AA)	RO (\AA)	QM (10^{-6} \AA^{-2})	RM (\AA)
1	1.54213	41.3736	8.03377	0.286874	8.03377
2	1.38841	110.676	20.0	8.19373	5.0
3	1.36528	299.893	100.0	8.86257	100.0
4	1.37150	113.894	25.0	8.09464	100.0
5	1.49722	100.00	50.0	0.0	25.0

angular divergence = 0.0008 radians

Table A.5: Sample A, Annealed, Spinflip, 3 layers

Layer	QC (10^{-4} \AA^{-2})	D (\AA)	RO (\AA)	QM (10^{-6} \AA^{-2})	RM (\AA)
1	1.53353	46.2766	8.68635	1.25677	8.68635
2	1.38544	520.512	45.0	8.00087	5.0
3	1.51303	100.0	56.3144	0.0	11.2303

angular divergence = 0.0008 radians

TH = 250.643 for layers 1-3 (canting angle)

Table A.6: Sample A, As-Grown, Low-Field Scan, 6 layers

Layer	QC (10^{-4} \AA^{-2})	D (\AA)	RO (\AA)	QM (10^{-6} \AA^{-2})	RM (\AA)
1	1.42572	53.4529	1.0	2.97669	1.0
2	1.44503	99.6431	50.0	4.45752	20.0
3	1.47284	137.643	50.0	2.80193	75.0
4	1.48773	141.841	125.0	2.48271	55.0
5	1.44937	110.484	100.0	2.2319	100.0
6	1.54858	100.0	10.0	0.0	5.0

angular divergence = 0.0009 radians

Table A.7: Sample A, Annealed, Low-Field Scan, 5 layers

Layer	QC (10^{-4} \AA^{-2})	D (\AA)	RO (\AA)	QM (10^{-6} \AA^{-2})	RM (\AA)
1	1.56737	44.9209	1.7774	0.467444	1.7774
2	1.42311	214.955	38.9254	8.55355	25.0
3	1.44579	203.322	92.1386	8.37688	25.0
4	1.44664	106.802	50.0	7.37532	50.0
5	1.60818	100.0	80.1652	0.0	5.0

angular divergence = 0.0009 radians

Table A.8: Sample B, As-Grown, 6 layers

Layer	QC (10^{-4} \AA^{-2})	D (\AA)	RO (\AA)	QM (10^{-6} \AA^{-2})	RM (\AA)
1	1.44708	32.3978	1.0	0.0	1.0
2	1.4757	178.559	5.0	4.0265	5.0
3	1.4743	403.392	125.0	2.7307	125.0
4	1.47137	301.636	250.0	1.83426	250.0
5	1.46013	154.935	30.0	1.82934	30.0
6	1.55396	100.0	5.0	0.0	5.0

angular divergence = 0.0005 radians

Table A.9: Sample B, Annealed, 6 layers

Layer	QC (10^{-4} \AA^{-2})	D (\AA)	RO (\AA)	QM (10^{-6} \AA^{-2})	RM (\AA)
1	1.58588	46.1736	1.0	0.0	1.0
2	1.49062	255.072	5.0	7.37021	45.0
3	1.49394	486.96	5.0	8.3118	20.0
4	1.49038	203.43	5.0	7.37397	25.0
5	1.50181	86.9446	5.0	4.97338	85.0
6	1.59125	100.0	30.0	0.0	35.0

angular divergence = 0.0006 radians

Table A.10: Sample B, As-Grown, 4 layers
Figs

Layer	QC (10^{-4} \AA^{-2})	D (\AA)	RO (\AA)	QM (10^{-6} \AA^{-2})	RM (\AA)
1	1.50786	59.1778	18.0421	2.71466	18.0421
2	1.47026	765.981	25.0	4.53827	25.0
3	1.46014	245.045	240.0	2.13161	240.0
4	1.55335	100.0	4.78176	0.0	5.0

angular divergence = 0.0005 radians

Table A.11: Sample B, Annealed, 3 layers

Layer	QC (10^{-4} \AA^{-2})	D (\AA)	RO (\AA)	QM (10^{-6} \AA^{-2})	RM (\AA)
1	1.5844	46.2038	1.0	0.0	1.0
2	1.49552	1028.82	1.0	7.25773	45.0
3	1.5897	100.0	51.4085	0.0	83.4488

angular divergence = 0.0006 radians

Table A.12: Sample C, As-Grown, 4 layers

Layer	QC (10^{-4} \AA^{-2})	D (\AA)	RO (\AA)	QM (10^{-6} \AA^{-2})	RM (\AA)
1	1.34757	39.2768	5.0	0.0	5.0
2	1.41492	350.722	15.0	4.06843	10.0
3	1.37744	114.638	98.487	4.06843	10.0
4	1.47579	100.00	5.0	0.0	25.0

angular divergence = 0.00055 radians

Table A.13: Sample C, Annealed, 3 layers

Layer	QC (10^{-4} \AA^{-2})	D (\AA)	RO (\AA)	QM (10^{-6} \AA^{-2})	RM (\AA)
1	1.42789	28.7854	4.9701	0.0	4.9701
2	1.43113	528.342	28.0	5.94935	1.0
3	1.53983	100.0	80.0	0.0	10.0

angular divergence = 0.00085 radians

Table A.14: Capped, As-Grown, 18 K Scan, 5 layers

Layer	QC (10^{-4} \AA^{-2})	D (\AA)	RO (\AA)	QM (10^{-6} \AA^{-2})	RM (\AA)
1	1.54123	83.9254	1.0	0.0	1.0
2	1.42349	20.3251	15.0	3.08855	5.0
3	1.45753	634.423	10.0	5.07656	25.0
4	1.45645	286.068	55.0	1.94938	285.0
5	1.55354	100.0	45.0727	0.0	150.0

angular divergence = 0.0006 radians

Table A.15: Capped, Annealed, 18 K Scan, 5 layers

Layer	QC (10^{-4} \AA^{-2})	D (\AA)	RO (\AA)	QM (10^{-6} \AA^{-2})	RM (\AA)
1	1.50632	79.6136	1.0	0.0	1.0
2	1.43133	440.987	5.0	3.68904	27.6156
3	1.42013	245.55	5.0	3.56019	134.743
4	1.41383	268.619	5.0	1.61322	245.0
5	1.51993	100.0	74.7787	0.0	135.0

angular divergence = 0.0006 radians

Table A.16: Capped, As-Grown, 13 K Scan, 5 layers

Layer	QC (10^{-4} \AA^{-2})	D (\AA)	RO (\AA)	QM (10^{-6} \AA^{-2})	RM (\AA)
1	1.50243	63.0506	1.0	0.0	1.0
2	1.42511	37.5841	5.0	2.44842	5.0
3	1.42358	652.018	5.0	5.07068	5.0
4	1.4226	290.774	5.0	1.15385	290.0
5	1.52632	100.00	28.9807	0.0	5.0

angular divergence = 0.00055 radians

Table A.17: Capped, Annealed, 13 K Scan, 5 layers

Layer	QC (10^{-4} \AA^{-2})	D (\AA)	RO (\AA)	QM (10^{-6} \AA^{-2})	RM (\AA)
1	1.51896	82.7079	1.0	0.0	1.0
2	1.42552	44.0366	25.0	3.80208	30.8159
3	1.46796	687.371	78.238	3.80603	75.0
4	1.45434	224.686	224.0	1.59548	224.0
5	1.55284	100.0	85.0	0.0	85.0

angular divergence = 0.00060 radians

Bibliography

- ¹ S. A. Wolf, D. D. Awschalom, R. A. Buhrman, J. M. Daughton, S. von Molnár, M. L. Roukes, A. Y. Chtchelkanova, D. M. Treger, *Science*, **294**, 1488 (2001).
- ² S. Datta and B. Das, *Appl. Phys. Lett.* **56**, 65 (1990).
- ³ D. D. Awschalom, M. E. Flatté, and N. Samarth, *Scientific American* **286**, 66 (2002).
- ⁴ H. J. Zhu, M. Ramsteiner, H. Kostial, M. Wassermeier, H. -P. Schönherr, and K. H. Ploog, *Phys. Rev. Lett.* **87**, 16601 (2001).
- ⁵ Y. Ohno, D. K. Young, B. Beschoten, F. Matsukura, H. Ohno, and D. D. Awschalom, *Nature* **402**, 790 (1999).
- ⁶ P. Van Dorpe, Z. Liu, W. Van Roy, V. F. Motsnyi, M. Sawicki, G. Borghs, and J. De Boeck, *Appl. Phys. Lett.* **84**, 3495 (2004).
- ⁷ T. Kasuya and A. Yanase, *Rev. Mod. Phys.* **40**, 684 (1968).
- ⁸ A. Mauger and C. Godart, *Phys. Rep.* **141**, 51 (1986).
- ⁹ H. Ohno, *Science* **281**, 951 (1998).
- ¹⁰ J. K. Furdyna, *J. Appl. Phys.* **64**, R29 (1988).
- ¹¹ H. Munekata, H. Ohno, S. von Molnar, Armin Segmüller, L. L. Chang, and L. Esaki, *Phys. Rev. Lett.* **63**, 1849 (1989).
- ¹² H. Ohno, H. Munekata, T. Penny, S. von Molnár, and L. L. Chang, *Phys. Rev. Lett.* **68**, 2664 (1992).
- ¹³ H. Ohno, A. Shen, F. Matsukura, A. Oiwa, A. Endo, S. Katsumoto, and Y. Iye, *Appl. Phys. Lett.* **69**, 363 (1996).
- ¹⁴ K. C. Ku, S. J. Potashnik, R. F. Wang, S. H. Chun, P. Schiffer, N. Samarth, M. J. Seong, A. Mascarenhas, E. Johnston-Halperin, R. C. Myers, A. C. Gossard, and D. D. Awschalom, *Appl. Phys. Lett.* **82**, 2302 (2003).
- ¹⁵ K. W. Edmonds, P. Bogusławski, K. Y. Wang, R. P. Campion, S. N. Novikov, N. R. S. Farley, B. L. Gallagher, C. T. Foxon, M. Sawicki, T. Dietl, M. Buongiorno Nardelli, and J. Bernholc, *Phys. Rev. Lett.* **92**, 37201 (2004).
- ¹⁶ T. Dietl, H. Ohno, F. Matsukura, J. Cibert, D. Ferrand, *Science* **287**, 1019 (2000).

- ¹⁷ K. Yosida, *Theory of Magnetism*, (Springer, Berlin, 1996).
- ¹⁸ B. Beschoten, P. A. Crowell, I. Malajovich, D. D. Awschalom, F. Matsukura, A. Shen, and H. Ohno, *Phys. Rev. Lett.* **83**, 3073 (1999).
- ¹⁹ C. Zener, *Phys. Rev.* **81**, 440 (1951).
- ²⁰ C. Zener, *Phys. Rev.* **83**, 299 (1951).
- ²¹ T. Hayashi, Y. Hashimoto, S. Katsumoto, and Y. Iye, *Appl. Phys. Lett.* **78**, 1691 (2001).
- ²² S. J. Potashnik, K. C. Ku, S. H. Chun, J. J. Berry, N. Samarth, and P. Schiffer, *Appl. Phys. Lett.* **79**, 1495 (2001).
- ²³ K. W. Edmonds, K. Y. Wang, R. P. Campion, A. C. Neumann, N. R. S. Farley, B. L. Gallagher, and C. T. Foxon, *Appl. Phys. Lett.* **81**, 4991 (2002).
- ²⁴ S. J. Potashnik, K. C. Ku, R. Mahendiran, S. H. Chun, R. F. Wang, N. Samarth, and P. Schiffer, *Phys. Rev. B* **66**, 12408 (2002).
- ²⁵ J. Blinowski and P. Kacman, *Phys. Rev. B* **67**, 121204 (2003).
- ²⁶ K. M. Yu, W. Walukiewicz, T. Wojtowicz, I. Kuryliszyn, X. Liu, Y. Sasaki, and J. K. Furdyna, *Phys. Rev. B* **65**, 201303 (2002).
- ²⁷ W. Walukiewicz, *Appl. Phys. Lett.* **54**, 2094 (1989).
- ²⁸ S. Lee, S. J. Chung, I. S. Choi, Sh. U. Yuldeshev, H. Im, T. W. Kang, W. -L. Lim, Y. Sasaki, X. Liu, T. Wojtowicz, and J. K. Furdyna, *J. Appl. Phys.* **93**, 8307 (2003).
- ²⁹ S. Sanvito and N. A. Hill, *Appl. Phys. Lett.* **78**, 3493 (2001).
- ³⁰ P. A. Korzhavyi, I. A. Abrikosov, E. A. Smirnova, L. Bergqvist, P. Mohn, R. Mathieu, P. Svedlindh, J. Sadowski, E. I. Isaev, Yu. Kh. Vekilov, and O. Eriksson, *Phys. Rev. Lett.* **88**, 187202 (2002).
- ³¹ D. E. Bliss, D. D. Nolte, W. Walukiewicz, J. W. Ager III, E. E. Haller, K. T. Chan, and S. Tanigawa, *J. Appl. Phys.* **71**, 1699 (2002).
- ³² D. Chiba, K. Takamura, F. Matsukura, and H. Ohno, *Appl. Phys. Lett.* **82**, 3020 (2003).
- ³³ M. B. Stone, K. C. Ku, S. J. Potashnik, B. L. Sheu, N. Samarth, and P. Schiffer, *Appl. Phys. Lett.* **83**, 4568 (2003).

- ³⁴ B. J. Kirby, J. A. Borchers, J. J. Rhyne, S. G. E. te Velthuis, A. Hoffmann, K. V. O'Donovan, T. Wojtowicz, X. Liu, W. L. Lim, and J. K. Furdyna, *Phys. Rev. B* **69**, 81307 (2004).
- ³⁵ C. F. Majkrzak, K. V. O'Donovan, N. F. Berk, to be published (2004).
- ³⁶ M. R. Fitzsimmons and C. F. Majkrzak, to be published (2003).
- ³⁷ G. P. Felcher, *Phys. Rev. B* **24**, 1595 (1981).
- ³⁸ Nuclear SLD and chemical SLD is the same thing. I employ the dubious tactic of alternating these names depending on the situation. For instance, using “nuclear” is more intuitive when discussing the mechanisms through which neutrons scatter from a collection of nuclei, but “chemical” is more intuitive when using SLD to discuss changes in chemical composition. If this is frustrating instead of helpful, the reader reserves the right to make malicious comments about the author.
- ³⁹ J. J. Sakurai, *Modern Quantum Mechanics*, Chapter 7, (Addison-Wesley, New York, 1994).
- ⁴⁰ <http://www.ncnr.nist.gov/icp>.
- ⁴¹ <http://www.pns.anl.gov/instruments/posyii/>.
- ⁴² G. P. Felcher, R. O. Hileke, R. K. Crawford, J. Haumann, R. Kleb, and G. Ostrowski, *Rev. Sci. Instr.* **58**, 609 (1987).
- ⁴³ http://www.ncnr.nist.gov/programs/reflect/data_reduction/software/index.html.
- ⁴⁴ J. F. Ankner and C. F. Majkrzak, *Neutron Optical Devices and Applications, SPIE Conference Proceedings*, Vol. 1738, edited by C. F. Majkrzak, and J. W. Wood (SPIE, Bellingham, WA, 1992), pp. 260-269.
- ⁴⁵ C. F. Majkrzak, N. F. Berk, and U. A. Perez-Salas, *Langmuir* **19**, 7796 (2003).
- ⁴⁶ G. M. Schott, W. Fashinger, and L. W. Molenkamp, *Appl. Phys. Lett.* **79**, 1807 (2001).
- ⁴⁷ I. Kuryliszyn-Kudelska, J. Z. Domagała, T. Wojtowicz, X. Liu, E. Łusakowska, W. Dobrowolski, and J. K. Furdyna, *J. Appl. Phys.* **95**, 603 (2004).
- ⁴⁸ X. Liu, private communication.
- ⁴⁹ Note the use of the word “consistent” when discussing interpretation of the resistivity. Differences in maximum resistivity could conceivably be due to factors other than carrier concentration (e.g. defects, contact quality, etc.).

- ⁵⁰ Spin asymmetry is also commonly referred to as “polarization”
- ⁵¹ D. J. Keavney, D. Wu, J. W. Freeland, E. Johnston-Halperin, D. D. Awschalom, and J. Shi, *Phys. Rev. Lett.* **91**, 187203 (2003).
- ⁵² Yu-Jun Zhao, W. T. Geng, K. T. Park, and A. J. Freeman, *Phys. Rev. B* **64**, 035207 (2001).
- ⁵³ E. Kulatov, H. Nakayama, H. Mariette, H. Ohta, and Yu. A. Uspenskii, *Phys. Rev. B* **66**, 045203 (2002).
- ⁵⁴ A. Leineweber, R. Niewa, H. Jacobs, and W. Kockelmann, *J. Mater. Chem.* **10**, 2827 (2000).
- ⁵⁵ Since the annealed sample has a non-magnetic surface layer, one might question the use of the *entire* non-substrate thickness for calculating the integrated magnetization. This was the convention adopted for Ref. 34, so I’ve stuck with it for this chapter. In practice, this typically only makes a difference of only 1-2 emu-cm⁻³, so it’s probably not worth losing sleep over.
- ⁵⁶ This witty terminology is the unofficial brainchild of J. A. Borchers.
- ⁵⁷ While exhaustive measures have been taken to try to examine all likely models, remember from Chapter 2, no *guarantee* can be made that there isn’t some wild model lurking out in the ether that fits the data, but that we haven’t conceived of!
- ⁵⁸ X. Liu, private communication.
- ⁵⁹ Ashcroft and Mermin, *Solid State Physics*, chapter 33 (Saunders, 1976).
- ⁶⁰ G. L. Squires, *Introduction to the Theory of Thermal Neutron Scattering*, Chapter 8 (Dover, 1978).
- ⁶¹ J. M. Luttinger and W. Kohn, *Phys. Rev.* **97**, 869 (1954).
- ⁶² Jürgen König, T. Jungwirth, and A. H. MacDonald, *Phys. Rev. B* **64**, 184423 (2001).
- ⁶³ H. Ohno, N. Akiba, F. Matsukura, A. Shen, K. Ohtani, and Y. Ohno, *Phys. Rev. B* **57**, R2037 (1998).
- ⁶⁴ J. Okabayashi, A. Kimura, O. Rader, T. Mizokawa, A. Fujimori, T. Hayashi, and M. Tanaka, *Phys. Rev. B* **58**, R4211 (1998).
- ⁶⁵ T. Omiya, F. Matsukura, T. Dietl, Y. Ohno, T. Sakon, M. Motokawa, and H. Ohno, *Physica E* **7**, 976 (2000).

⁶⁶ Gen Shirane, Stephen M. Shapiro, and John M. Tranquada, *Neutron Scattering With a Triple-Axis Spectrometer*, (Cambridge University Press, 2002).

⁶⁷ For the sake of conceptual simplicity I'm ignoring the presence of wavelength $n\lambda$ neutrons that might be scattered by a monochromator or analyzer crystal in addition to neutrons of the desired λ . In reality, this is an important effect that we accounted for with a higher-order Be filter.

Publications

Spin Excitations in $La_{1-x}Ca_xMnO_3$

L. Stumpe, B. Kirby, H. Kaiser, J. J. Rhyne, and J. Mitchell, *Journal of Applied Physics* **91**, 7511 (2002).

Annealing Dependent Magnetic Depth Profile in $Ga_{1-x}Mn_xAs$

B. J. Kirby, J. J. Rhyne, J. A. Borchers, K. V. O'Donovan, S. G. E. te Velthuis, A. Hoffmann, T. Wojtowicz, X. Liu, W. L. Lim, and J. K. Furdyna, *Physical Review B* **69** 81307(R) (2004).

Effects of Capping on the $Ga_{1-x}Mn_xAs$ Magnetic Depth Profile

B. J. Kirby, J. J. Rhyne, J. A. Borchers, K. V. O'Donovan, T. Wojtowicz, X. Liu, Z. Ge, S. Shen, and J. K. Furdyna, submitted to *Applied Physics Letters*, September 2004.

Spin Dynamics and Magnon-Phonon Interactions in $Nd_{0.6}Sr_{0.4}MnO_3$

B. J. Kirby, J. J. Rhyne, H. Kaiser, Y. Tokura, and H. Kuwahara, submitted to *Physical Review B*, December 2004.

Invited Talks

Princeton Plasma Physics Laboratory FQ Equilibrium Code UNIX Workstation Port

B. J. Kirby and M. D. Mulligan, FA-SURE Conference, Argonne National Laboratory, Argonne, IL, June 1999.

Neutron Scattering Studies of Ferromagnetic Semiconductors

B. J. Kirby, Missouri University Research Reactor Fellowship Award Seminar, Columbia, MO, May 2003.

Annealing-Dependent Phenomena in Ferromagnetic Semiconductors: a neutron scattering study of $Ga_{1-x}Mn_xAs$

B. J. Kirby, University of Missouri-Columbia Department of Physics Condensed Matter Seminar, Columbia, MO, September 2003.

Annealing-Dependent Phenomena in $Ga_{1-x}Mn_xAs$

B. J. Kirby, International Workshop on Polarized Neutrons in Condensed Matter Investigations, Washington D. C., June 2004.

Annealing-Dependent Phenomena in $Ga_{1-x}Mn_xAs$

B. J. Kirby, Invited Lecturer, NIST Summer School on Neutron Small Angle Scattering and Reflectometry from Submicron Structures, Gaithersburg, MD, June 2004.

Mechanisms of Annealing-Induced Ferromagnetic Enhancement in $Ga_{1-x}Mn_xAs$

B. J. Kirby, University of Missouri-Columbia O. M. Stewart Colloquium, Columbia, MO, October 2004.

Contributed Conference Presentations

Magnetization Profile in GaMnAs

J. J. Rhyne, B. J. Kirby [presenter], S. G. E. te Velthuis, A. Hoffmann, T. Wojtowicz, X. Liu, and J. K. Furdyna, Bulletin of the American Physical Society **48**, # 1 (March 2003).

Depth Profile & Annealing Dependence in Ga_{1-x}Mn_xAs

J. J. Rhyne, B. J. Kirby, S. G. E. te Velthuis [presenter], A. Hoffmann, J. A. Borchers, K. V. O'Donovan, J. K. Furdyna, T. Wojtowicz, and X. Liu, poster presentation at the International Conference on Magnetism, Rome, Italy, August 2003 [poster by B. J. Kirby].

Magnetic Depth Profile and Annealing Dependence in Ga_{1-x}Mn_xAs

B. J. Kirby [presenter], J. J. Rhyne, J. A. Borchers, K. V. O'Donovan, S. G. E. te Velthuis, A. Hoffmann, J. K. Furdyna, T. Wojtowicz, and X. Liu, 9th Joint MMM/Intermag Conference, Anaheim, California, January 2004. *Finalist, Best Student Presentation Award.*

Annealing-Dependent Phenomena in Ga_{1-x}Mn_xAs

B. J. Kirby [presenter], J. J. Rhyne, J. A. Borchers, K. V. O'Donovan, S. G. E. te Velthuis, A. Hoffmann, T. Wojtowicz, X. Liu, W. L. Lim, and J. K. Furdyna, poster presentation at the American Conference on Neutron Scattering, College Park, Maryland, June 2004 [poster by B. J. Kirby].

Effects of Capping on the Ga_{1-x}Mn_xAs Magnetic Depth Profile

B. J. Kirby [presenter], J. J. Rhyne, J. A. Borchers, K. V. O'Donovan, T. Wojtowicz, X. Liu, Z. Ge, S. Shen, and J. K. Furdyna. 49th Congerence on Magnetism and Magnetic Materials, Jacksonville, Florida, November 2004. *Finalist, Best Student Presentation Award.*

Vita

Brian James Kirby was born December 20, 1977 in Pittsburg, Kansas. He is the son of farmer and flight instructor Jim Kirby, and elementary school teacher Pat Kirby. Brian grew up with his younger brother Kevin on a grain farm near Nashville, Missouri and attended high school in Liberal, Missouri. During high school, Brian studied flying, and he obtained his private pilot's license in 1995. In 1996, Brian began college at Pittsburg State University, and despite a wide variety of enjoyable distractions, he graduated magna cum laude with a B. S. in Physics in 2000. Following graduation, Brian began graduate study in physics at the University of Missouri, where he worked with Prof. Jim Rhyne on neutron scattering studies of magnetic materials. In 2002, Brian married the lovely and talented Elizabeth Buckalew of Anchorage, Alaska. After receiving his Ph. D. in Physics from Mizzou in December, 2004, Brian and Elizabeth moved to Los Alamos, New Mexico, where Brian took a postdoctoral position at Los Alamos National Laboratory.